UNIVERSIDAD DE CHILE
FACULTAD DE CIENCIAS FÍSICAS Y MATEMÁTICAS
ESCUELA DE POSTGRADO Y EDUCACIÓN CONTINUA

TRANSPORT OF POLLUTING PARTICLES IN ALLUVIAL CURRENTS DUE TO MINING ACCIDENTS. CASE STUDY: SPILL OF FINE MINERAL PARTICLES IN RIVERS WITH GRAVEL BEDS

TESIS PARA OPTAR AL GRADO DE
DOCTORA EN CIENCIAS DE LA INGENIERÍA, MENCIÓN FLUIDODINÁMICA

NATALIA BUSTAMANTE PENAGOS

PROFESOR GUÍA:
YARKO IVÁN NIÑO CAMPOS

MIEMBROS DE LA COMISIÓN:
DR. ALDO TAMBURRINO TAVANTZIS
DR. CHRISTIAN IHLE BASCUÑÁN
DR. CARLOS MARCELO GARCÍA RODRÍGUEZ
DR. OSCAR LINK LAZO

SANTIAGO DE CHILE
2022

RESUMEN DE TESIS PARA OPTAR AL GRADO DE DOCTORA EN CIENCIAS DE LA INGENIERÍA, MENCIÓN FLUIDODINÁMICA
POR: NATALIA BUSTAMANTE PENAGOS
FECHA: 2022
PROF. GUÍA: YARKO IVÁN NIÑO CAMPOS

TRANSPORTE DE PARTÍCULAS CONTAMINANTES EN CORRIENTES ALUVIALES DEBIDO A ACCIDENTES MINEROS. CASO DE ESTUDIO: DERRAME DE PARTÍCULAS FINAS EN RÍOS CON LECHOS DE GRAVA

Esta tesis es una recopilación de artículos científicos originales autocontenidos. Se investigó la infiltración de partículas finas, como concentrado de cobre, relave y pumicita, en lechos de grava. Este estudio explica la dinámica de la contaminación de lechos con partículas finas luego de un accidente minero en lechos de grava. Esta contaminación ocurre por la depositación de partículas finas en sustratos en los cuales el tamaño del poro es mayor que el tamaño de la partícula fina. Investigaciones previas han caracterizado la profundidad de infiltración en función del diámetro del sustrato y de las partículas finas. Sin embargo, estas caracterizaciones no representan de buena forma la profundidad de infiltración de partículas finas como el concentrado de cobre y el relave. Adicionalmente, la densidad de las partículas no ha sido un factor considerado en el análisis, ya que los estudios han considerado partículas con densidades cercanas a las densidades de sedimentos naturales. Este trabajo consideró dos montajes experimentales y tres tipos de partículas finas, con densidades diferentes. Mediante técnicas de velocimetría se caracterizó el flujo superficial, se analizó la distribución de intensidades turbulentas antes y después de la contaminación del lecho con las partículas finas. Se reportaron eyecciones de partículas finas del tipo pumicita que pueden modificar la distribución de intensidades turbulentas en canales abiertos. También se analizan brigding y unimpeded static percolation como tipos de infiltración de partículas finas en lechos de grava, para diferentes espesores de sustratos. Se implementó el análisis espectral de Fourier y Wavelet, para caracterizar las estructuras turbulentas medidas experimentalmente. Se discute sobre los resultados obtenidos, el efecto de la densidad y los parámetros hidráulicos superficiales y subsuperficiales en la profundidad de infiltración.

RESUMEN DE TESIS PARA OPTAR AL GRADO DE DOCTORA EN CIENCIAS DE LA INGENIERÍA, MENCIÓN FLUIDODINÁMICA
POR: NATALIA BUSTAMANTE PENAGOS
FECHA: 2022
PROF. GUÍA: YARKO IVÁN NIÑO CAMPOS

TRANSPORT OF POLLUTING PARTICLES IN ALLUVIAL CURRENTS DUE TO MINING ACCIDENTS. CASE STUDY: SPILL OF FINE MINERAL PARTICLES IN RIVERS WITH GRAVEL BEDS

This thesis is a compilation of original independent scientific articles investigating infiltration of fine mineral particles such as copper concentrate, tailings, and pumicite into gravel beds. This study explains the dynamics of bed contamination with fine mineral particles after a mining accident in gravel beds. This contamination occurs by the deposition of fine mineral particles on substrates in which the pore size is greater than the fine particle size. Previous research has characterized infiltration depth as a function of substrate diameter and fine particle size. However, these characterizations do not represent the infiltration depth of fine particles such as copper concentrate and tailings. In addition, since studies have considered particles with densities close to natural sediment, it has not been a factor considered in the analysis. This work considered two experimental setups and three types of fine mineral particles with different densities. Surface flow was characterized by velocimetry techniques, and the distribution of turbulent intensities was analyzed before and after contamination of the bed with fine particles. Fine particle ejections that can modify the distribution of turbulent intensities in open flumes were reported. Bridging and unimpeded static percolation were also analyzed as types of fine particle infiltration in gravel beds for different substrate thicknesses. Fourier and Wavelet spectral analysis was implemented to characterize the experimentally measured turbulent structures. The results obtained and the effect of density and surface and subsurface hydraulic parameters on the infiltration depth are discussed.

A mis padres, Eugenia y Guillermo, hermanos y tíos por su apoyo incondicional y enseñarme siempre el valor de la perseverancia.

A mis sobrinos Sara, Manuela y Miguel por llenar de alegria la vida.

Agradecimientos

Quiero agradecer a la Universidad de Chile, en particular al departamento de Ingeniería Civil de la Facultad de Ciencias Físicas y Matematicas, por todo el apoyo brindado y por haberme acogido durante este tiempo.

Quiero agradecer también, al profesor Gabriel Easton Vargas quien me permitió hacer las curvas granulométricas de sedimentos finos, en el laboratorio de Sedimentología del departamento de Geología.

Quiero agradecer a ANID quienes por medio de la beca de doctorado Nacional N° 21181620 y el proyecto Fondecyt N° 1140767 financiaron esta investigación. Además agradecer al Advanced Mining Technologic Center (AMTC) por el financiamento de congresos.

Quiero agradecer además a Camilo Tapia Carrasco, Gustavo Aracena, Felipe Galaz por la colaboración durante la ejecución de los experimentos. A don Juan, don Manuel y Geovanni por toda la ayuda técnica en el laboratorio. A Jacqueline Suarez, Joseph Rozas, Edwin Paccha, William Licanqueo, Diego Villegas, Paula Calderon, Susi Cadavid, Javiera Abarca, Aldo Muñoz, Ariel Crespo, Eduardo Muñoz, Nicolás Vasquez y Pablo Mardones por todo el apoyo brindado durante este tiempo. A Lorena Fuentes por toda su ayuda en el área administrativa de la Universidad.

Finalmente quiero agradecer muy profundamente a los profesores Yarko Niño y Aldo Tamburrino por su paciencia, su disposición para guiarme en este proceso de mi vida académica y por ser excelentes ejemplos a seguir en la vida.

Table of Content

List of Tables

List of Figures

Chapter 1

Introduction

1.1 Motivation

In mining industry, the extraction of minerals can generate concentrates and tailings that can be toxic because these materials have a high content of heavy metals, sulfides and sulphur. The extracted material and tailings can be transported from the mine to the port or dam by pipelines, channels, trains, and others. The extracted ore is transported as a hyperconcentrate mixture of particles, between 60-65%, and water, between 35-40%, through pipes or channels and the routes for transporting the extracted material may cross rivers or lakes, thus generating a high risk of pollution associated with a potential accident in the area near the bodies of water. Amankwah, Pickles (2009) reported that the sulphide minerals in gold concentrate can be arsenopyrite, pyrite, pyrrohtite, moscovite, and chlinochlore. Fuentes et al. (2009) stated that the ore identified in copper concentrate was digenie, chalcopyrite, bornite, covellite, pyrite and sphalerite. In the case of copper concentrate, gold and iron the heavy metals reported are iron, copper, gold, arsenic, chromium, cadmium, nickel, molybdenum, and others. On the other hand, the coal extraction can generate heavy metal pollution of soils such as reported in China by Liu et al. (2019). In this research Liu et al. (2019) reported high concentration of cadmium, lead and nickel, however, components as arsenic, chromium, copper, zinc and nickel showed a low potential ecological risk.
Pollution of water bodies due to mining accidents has occurred worldwide. Copper concentrate in Uganda's Lake George, which is 11 km downstream from a copper mine, was reported by Edroma (1974). The tailings dam break at the Harmony Golden mining spilled 2.5 Mton near Merriespruit, South Africa in 1994 (Van Niekerk, Viljoen, 2005); in 2009, a valve break of a pipe generated a spill of 45 m^3 of copper concentrate into Choapa river in the Coquimbo region, Chile; in 2011, a broken seal on a tank of mining products spilled 5 m^3 in Los Andes, Chile and, in 2016, a rupture of a pipeline in the Blanco River, Saladillo, Chile, dumped 50 m^3 of copper concentrate. Mount Polley mine tailings dam break in British Columbia spilled 25 Mm^3 of tailings into the Quesnel river basin (Byrne et al., 2015). Fundão tailings dam failure in Brasil spilled 43 Mm^3, and that material reached the Atlantic Ocean (Carmo do et al., 2017).
The spilled material from mining accidents is a biphasic mixture, i.e., water and particles. These mixtures cause turbidity and generate a decrease in light reaching the bottom of

rivers, affecting the zooplankton, fishes and macro-invertebrates (Lloyd et al., 1987; Wood, Armitage, 1997). Furthermore, in highly permeable beds, for instance gravel beds, interstitial flow velocities can transport fine particles into the hyporheic zone by filling interstitial spaces (Mcdowell-Boyer et al., 1986; Findlay, 1995). Fine particles in gravel bed streams generate large changes in hyporheic exchange, macroinvertebrate survival, nutrient cycling, low oxygenation of fish eggs, anaerobic changes, thus having a high environmental impact (Beschta, Jackson, 1979; Diplas, Parker, 1985; Lisle, 1989; Findlay, 1995; Tonina, Buffington, 2009; Shrivastava, 2020).
However, the environmental impact due to spillage of mining materials into water bodies is greater than for instance a landslide, because mining materials contain heavy metals and these materials can reside for thousands of years as a secondary source of contamination (Byrne et al., 2015). Additionally, the gravel bed substrates can become a storage area for toxic materials (Thoms, 1987). Byrne et al. (2015) stated that the environmental risk increases when the spilled tailings occurs in the upper part of the basin, as high river flows are associated with snowmelt and have a high potential to remobilize fine material for transport in suspension.

1.2 Background

The sediment transport in alluvial streams is through suspension and bedload. Saltation, rolling, sliding, are modes of bedload, Figure 1.1, and the fine particle infiltration phenomenon occurs when the fine particle is much finer than the sediment bed. The movement of a particle is generated when the hydrodynamic forces are higher than a critical value (Dey, Papanicolaou, 2008). This is called *incipient motion* of non-cohesive sediment in bed. Shields (1936) proposed to analyze the tractive-forces coefficient, $\tau_* = \tau_0/((\rho_s - \rho)\, g\, \mathrm{d}_s)$, as a function of Reynolds number of the grain, $Re_* = u_*\, \mathrm{d}_s/\nu$, where τ_0 is shear stress in the bed, ρ_s and ρ are the sediment density and fluid density, respectively, d_s is the particle diameter, u_* is shear velocity and ν is the kinematic viscosity. On the other hand, Geremew, Yanful (2011) analyzed incipient motion considering cohesive particles in tailings. They adopted the Shields' critical mobility parameter:

$$\tau_{*-EX} = \frac{\tau_{cr}}{(\rho_s - \rho)\, g\, \mathrm{d}_{50}} \tag{1.1}$$

where τ_{*-EX} depends on fines content.

On the other hand, fine particles can infiltrate into the substrate. In this context, several researchers have studied the infiltration phenomenon. Einstein (1968) in Diplas, Parker (1985), Beschta, Jackson (1979), Carling (1984), Cui et al. (2008), Diplas, Parker (1985), Iseya, Ikeda (1987) experimentally researched the infiltration dynamics of fine sand into gravel beds. They reported that the infiltration phenomenon depends on the size of the coarse material. They did not find evidence that link the effect of the hydraulic flow parameters in the infiltration depth, such as Fr, τ_*. On the other hand, the mechanisms of infiltration reported by Diplas, Parker (1985), Gibson et al. (2009), Huston, Fox (2015), Dudill et al. (2016) are the so called unimpeded static percolation and bridging. Unimpeded static percolation is when fine sediments can move freely in the bed depth towards some

physical barrier, while bridging is when the fine sediment cannot move freely in the bed depth. Researchers such as Beschta, Jackson (1979), Gibson et al. (2009), Huston, Fox (2015) and Dudill et al. (2016) has analyzed the thresholds for characterizing infiltration type as function of fine sediment size. Table 1.1 presents a summary of thresholds reported by Beschta, Jackson (1979), Gibson et al. (2009), Huston, Fox (2015) and Dudill et al. (2016). D_{ss}, D_{fs} are diameters of substrate sediment and fine sediment, respectively, and σ_{ss} is the standard deviation ($\sqrt{D_{84ss}/D_{16ss}}$), D_g is the diameter of substrate. Nevertheless, classic literature does not report investigations about mining particles, copper concentrate and tailings, in the river beds.

In highly permeable beds, such as gravel beds, interstitial flow velocities can transport fine particulates into the hyporheic zone filling the interstitial spaces (Mcdowell-Boyer et al., 1986; Findlay, 1995). Cui, Parker (1998) reported that the gravel porosity is a reservoir for the interstitial deposition of fine sediment. Iseya, Ikeda (1987) observed that the fine material fills the interstitial spaces formed, and can reduce the roughness of the grains. Lisle (1989) analyzed the phenomenon of infiltration of natural rivers and was able to report that fine sand can form a seal. Cui et al. (2008) through a theoretical model, showed that fine sediment accumulation decreases with depth into the substrate.

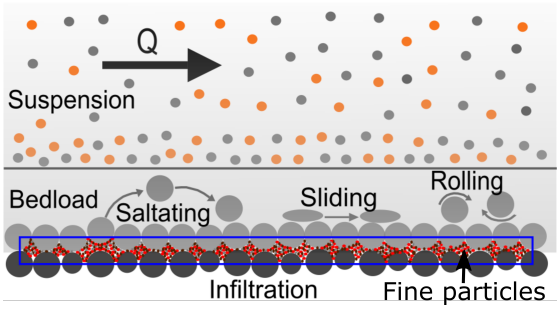

Figure 1.1: Mechanics of sediment transport

Table 1.1: Summary of thresholds to characterize the vertical gradation of fine sediments in gravel beds.

Researcher	Material	Types of movement	Criterion
Beschta, Jackson (1979)	Natural sediment	Bridging	$2D_{90g}$ to $5D_{90g}$
Gibson et al. (2009)	Natural sediment	Unimpeded static percolation	$D_{15ss}/D_{85fs} \geq 15.4$
		Transition	$12 < D_{15ss}/D_{85fs} < 14$
		Bridging	$D_{15ss}/D_{85fs} \leq 10.6$
Huston, Fox (2015)	Natural sediment	Unimpeded static percolation	$D_{ss}(D_{fs}\sigma_{ss})^{-1} > 27$
		Bridging	$D_{ss}(D_{fs}\sigma_{ss})^{-1} < 27$
Dudill et al. (2016)	one particle size	Bridging	$2.5 \leq D_{ss}/D_{fs} \leq 3.3$
		Partially unimpeded static percolation	$5.56 \leq D_{ss}/D_{fs}$

As mentioned above, fine sediments can move in suspension if the turbulent eddies of the flow have upward velocity components exceeding the fall velocity of the particles (Bagnold, 1966). Besides, the grain roughness could generate an increment in the vertical intensity of turbulence (Jackson, 1976). The strong upward turbulent ejections could generate the vertical

anisotropy for suspension transport and the entrainment of the fine sediment (Jackson, 1976; Niño, García, 1996; Niño et al., 2003). Furthermore, several researches, such as Adrian (1991), Tamburrino, Gulliver (1999), Zhong et al. (2015), Zhong et al. (2016) studied the turbulent structures in smooth flumes. They showed and characterized hairpin vortices according to scale of motion, such as small scale motion $l \sim h$, hairpin vortices that have a large scale motion $l \sim 3h$, and super streamwise vortices, which have a super scale motion $l > 10h$, where l is the streamwise scale of the vortices and h is the water depth. Conversely, Nikora (2005); Roussinova (2009); Shamloo, Pirzadeh (2015) analyzed rough beds. Roussinova (2009) showed that at shallow depths roughness increases turbulence intensities compared to turbulent intensities in a smooth bed, however in the outer layer these turbulence intensities have smaller differences between smooth bed and rough bed.

In addition, turbulence can be analyzed by considering turbulent fluctuations using quadrant analysis, where $Q1$ ($u' > 0$ and $w' > 0$) represent inward interactions, $Q2$ ($u' < 0$ and $w' > 0$) are ejections, $Q3$ ($u' < 0$ and $w' < 0$) are outward interactions, and $Q4$ ($u' > 0$ and $w' < 0$) are sweeps. According to Adrian (1991); Niño, Musalem (2000); Sambrook Smith, Nicholas (2005); Cooper et al. (2018); Wallace (2016) the sweeps and ejections are more more frequent interactions than outward and inward interactions. Experimental researches have showed that the ejections and sweeps are the most frequent turbulence interactions and the sweeps interaction, are more efficient for the entrainment of sediment particles into suspension than ejections (Niño, Musalem, 2000). In these researches it was considered a mobile bed. Sambrook Smith, Nicholas (2005) studied the deposition of sand on gravel beds, they could report that fine sediment deposited in a gravel bed can reduce the vertical velocities' gradients and shear stresses near the bed.

Roussinova (2009) compared results for rough and smooth walls and found that the magnitude of the turbulence quantities are higher in the case of the rough wall, so the roughness and the flow depth are key to modify the turbulent structures at shallow flow conditions, and also reported that ejection events are prevalent over sweeps. On the other hand, Manes et al. (2009) compared the turbulence structure for permeable and impermeable beds in open channels, finding that large scale eddies generated within the surface flow have influence in the subsurface flow.

In this thesis, both the infiltration of fine particles into gravel beds and the turbulence interaction in the neighbourhood of the gravel bed associated with sediment ejection were analyzed. The result of this thesis enabled the publication of three papers, and the Chapters 2, 3, 4 are based on published works considering the observation of the reviewers of the thesis. Chapter 2 shows the paper on the experimental results on copper concentrate spilling in immobile gravel bed. An experimental analysis of the suspension and infiltration of copper concentrate in gravel beds after a mining accident is presented. Chapter 3 shows the experimental results on the expulsion of fine sediments and the analysis of turbulent interactions associated with the presence of sediment ejection in the neighborhood of the bed. Chapter 4 analyzed the infiltration of copper concentrate, pumicite and tailings in open channels. The analysis considers the effect of surface and subsurface flows, density and size of fine particles. Chapter 5 presents the general conclusions of the research and future work. Finally, two papers congress are presented as appendixes, Appendix A was the paper presented in the 38th IAHR World Congress and Appendix B was the paper presented in XXV Chilean congress of hydraulic engineering.

1.3 Hypothesis

In this thesis, the infiltration of fine mineral particles into a gravel bed was analyzed. According to the background presented in section 1.2, the dynamics of infiltration of fine mineral particles into a gravel bed has not been discussed in the literature. For this reason, the hypothesis of this thesis assumes that there is a similar transport dynamic between the infiltration of sands into gravel beds and the infiltration of fine mineral particles into the gravel bed. However, in the case of fine mineral particles the subsurface flow is more important than that of the infiltration of sands. Additionally, the transport mechanisms of fine mineral particles could change according to the size, density of the material. In fact, there would be no bed load because a fine particle tends to move in suspension or to infiltrate. Furthermore, the fine mineral, in some cases, material has a high density and this physical property could facilitate the deposition of fine particles and these could modify the turbulent interactions in the neighbourhood of the bed.

1.4 Objectives

Main objective

To characterize and describe, through laboratory experiments, the dynamics of infiltration of fine mineral particles in alluvial streams and the interaction zone between surface and subsurface flow.

Specific objectives

1 Experimentally characterize the infiltration of fine mineral particles in flumes with sediment beds, considering both physical and kinematic parameters.

2 To analyze the infiltration of fine mineral particles in a gravel bed and the changes in the distribution of turbulent interactions in the neighborhood of gravel beds.

3 To characterize the infiltration depth of minerals particles considering dimensional analysis and using image processing.

4 To analyze turbulent intensities and shear stress variations near the bed before and after the infiltration of mineral particles, and the effect of fine mineral particles deposited in the bed on the distribution of turbulent intensities and turbulent structures.

1.5 Methodology

The experimental approach considered in this thesis were two experimental setups to analyze the dynamics of gravel bed contamination. The experiments in Chapter 2 and Chapter 4 were conducted in the experimental setup used by Bustamante-Penagos, Niño (2020b). This setup consisted of an open channel 0.11 m wide, 3.0 m long, 0.15 m deep, and bed slope that varied between 0.007 and 0.047. The fine material was fed as punctual discharge through an acrylic cone, 2.83 cm in diameter (Figure 1.2a).
The experiments in Chapter 3 and Chapter 4 were conducted in the experimental setup used

by Bustamante-Penagos, Niño (2020a). This setup consisted of an open channel, 0.03 m wide, 0.58 m long, and 0.63 m deep. The structure is divided into three sections. Upstream are the surface and subsurface input flows. At the center of the facility are the open channel, the bed, and the point where the fine material mixture is spilled. In the downstream area are the surface and subsurface output discharges. The fine material was fed through an acrylic cone in the free surface, of 1.0 cm of diameter (Figure 1.2b). The arrangement used in this thesis considered a bed with two layers of sediments and an immobile bed. The surface layer is composed of gravel and subsurface layer is sand.
The instrumentation used were a Venturi pipe for flow measurement, a Nikon D3200 camera for image analysis of fine sediment transport, and a Photron FASTCAM Mini UX50 camera that takes up of 2500 fps, for Particle Image Velocimetry (PIV) analysis. The grain size distribution analysis of the fine particles is carried out in the Sedimentology Laboratory of the Universidad de Chile with Malvern Mastersizer 2000 equipment. On the other hand, in Chapters 2 - Chapter 4 are presented the methodology implemented in each experiment.

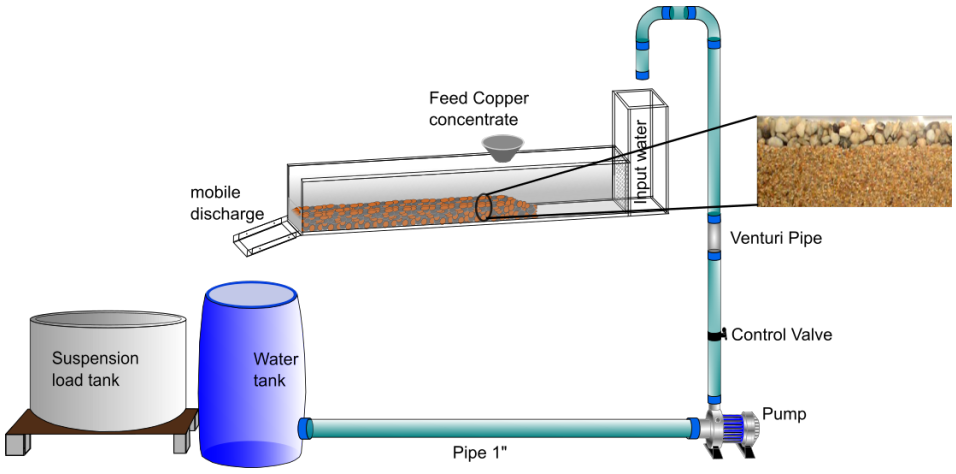

(a) The experimental setup used in (Bustamante-Penagos, Niño, 2020b)

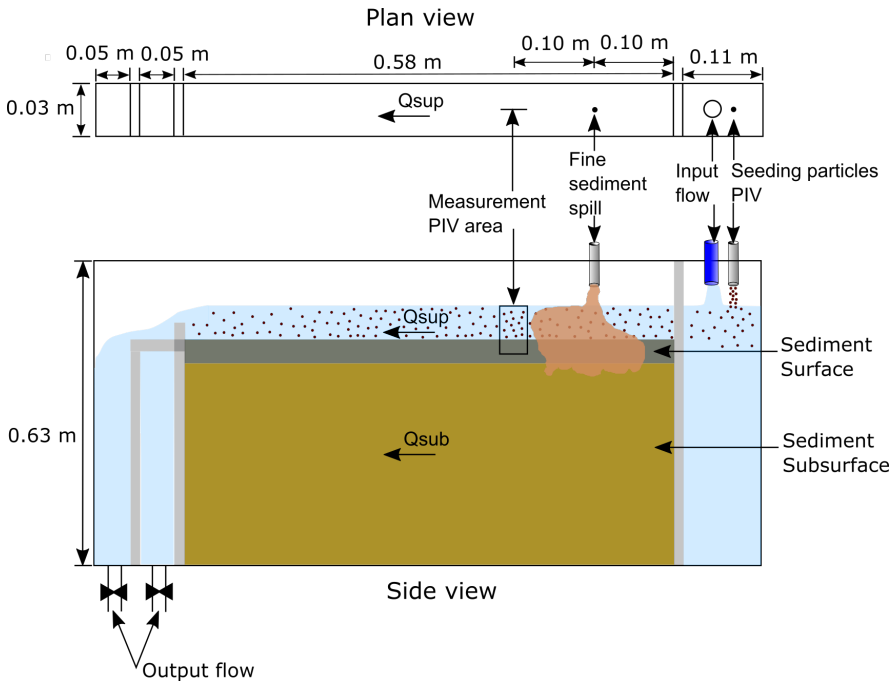

(b) The experimental setup used in (Bustamante-Penagos, Niño, 2020a).

Figure 1.2: **(a)** Flume with water recirculation and with the possibility of diverting the flow with a chute to a tank (Bustamante-Penagos, Niño, 2020b); **(b)** Experimental scheme used in the study of (Bustamante-Penagos, Niño, 2020a). The flume with 0.39 m of sediment thickness is used to measure high infiltrations of fine sediment and subsurface flow. The surface flow rate is Q_{sur} and subsurface flow rate is Q_{sub}.

Chapter 2

Suspension and infiltration of copper concentrate in a gravel bed: a flume study to evaluate the fate of a potential spill in a Chilean river.

This chapter is based in the paper published in Environmental Earth Science journal (2020). Bustamante-Penagos N. y Niño Yarko. doi:s12665-020-09274-y

Abstract

This paper shows the advances of an experimental study of the spill of copper concentrate into immobile gravel beds. The purposes of this research are to identify the dynamics of the copper concentrate as it spills in gravel bed rivers due to mining pipeline accidents, and to quantify loads of transport in suspension and bed infiltration experimentally. The sedimentation process is generated downstream of the spill, inducing the infiltration into the bed. We have found two types of infiltration: unimpeded static percolation, when the pore size is larger than the size of copper concentrate into the substrate, or bridging layer, when the size of copper concentrate is larger than the pores in the substrate. For large fluvial sediments, $d_{90s}/d_{50c} > 47$, the infiltration of the copper concentrate reaches a state of unimpeded static percolation. Moreover, when the size of the granular material is small, $d_{90s}/d_{50c} < 28$, the bridge layer avoid free infiltration of the copper concentrate. The maximum length of the bed on which we could make measurements is limited by the dimensions of the flume. About 50% by weight of the copper concentrate infiltrates in to the bed within a distance equal to 100 flow depths, downstream from the point where the spill was generated. Due to its high density, ultimately, the copper concentrate must completely infiltrate into the bed.

2.1 Introduction

Large amounts of fine sediment may be introduced into gravel bed rivers by erosion and anthropogenic changes, such as changes in land use in the watershed, mining accidents (ore concentrate or tailings), dredged material disposal from mining activities, or natural changes as erosion in the basin (Lisle, 1989; Parker et al., 1996; Macklin et al., 2006).
Pollution in gravel-bed rivers with fine materials has environmental effects; it may reduce hyporheic exchange, affecting oxygenation of fish eggs, macro-invertebrate survivorship, nutrient cycling, and pollutant retention (Beschta, Jackson, 1979; Diplas, Parker, 1985; Iseya, Ikeda, 1987; Lisle, 1989; Nuñez-González, 2016, and others). When fine material comes from mining, the problem is exacerbated because those materials have heavy metals that may reside in the substrate for a long time (Byrne et al., 2015).
Additionally, fine sediment in the gravel-bed substrate can change in the river processes, hydraulic parameters and vertical structure of gradation into the bed. Einstein (1968), in Diplas, Parker (1985), experimentally investigated the deposition of sand in stable gravel beds and observed that fine material fills the pores of the gravels from the bottom up. Beschta, Jackson (1979), Iseya, Ikeda (1987), Kuhnle et al. (2013), Niño et al. (2018), and others, also considered immobile beds in their researches on contamination of gravel beds with fine sediment. Beschta, Jackson (1979), Iseya, Ikeda (1987) and Niño et al. (2018) used a continuous sediment feeder localized at the flume inlet. They observed that the fine sediment interacts with the gravel bed and infiltrates. This method of introducing fine sediment is the same as in this article's experiments. The copper concentrate that is not transported into suspension interacts with the gravel bed and infiltrates.
Beschta, Jackson (1979) reported the formation of bridge or seal layers in the coarse material; their depth is on the order of 2 to 5 times the d_{90} of the coarse material, and the structures have only slight dependence between the seal depth and the Froude number. Diplas, Parker (1985) noticed that fine sediment could seal the gaps in the gravel (bridges), thus controlling the depth of infiltration. Bridge layers, or seal, are generated when the size of the fine sediment is larger than the pores in the substrate, i.e., the fine sediments cannot move freely through the interstitials spaces. Iseya, Ikeda (1987) observed that the fine material fills the interstitial spaces formed by the coarse material and can reduce the roughness of the grain. Lisle (1989) investigated the infiltration of fine sediment in natural channels and found that the fine sediment could form a seal (bridge), and the fine infiltration decreased as the bedload transport increased. Cui, Parker (1998) proposed that gravel porosity is a reservoir for the interstitial deposition of fine sediment. Cui et al. (2008), through a theoretical model, showed that fine sediment accumulation decreases with depth into the substrate.
On the other hand, Gibson et al. (2009), Huston, Fox (2015), and Dudill et al. (2016), using natural sediment and one particle size, characterized vertical movements of fine sediment into the substrate as: i) unimpeded static percolation, when fine sediments can move freely in the bed depth towards some physical barrier, and ii) bridging, when the fine sediment cannot move freely in the bed depth. Table 2.1 presents the characterization performed by Gibson et al. (2009), Huston, Fox (2015) and Dudill et al. (2016), where D_{ss} is the diameter of the substrate sediment, D_{fs} is the diameter of the fine sediment, and σ_{ss} is the standard deviation of the substrate ($\sqrt{D_{84ss}/D_{16ss}}$).
Previous research, have been done with gravel and sand as coarse and fine materials, but what happens when the fine sediment has great differences with respect to natural sediment? e.g., mining materials, such as ore concentrates or tailings, which, due to accidents, may end

Table 2.1: Summary of the vertical gradation characterization of fine sediments in gravel beds.

Researcher	Material	Types of movement	Criterion
Gibson et al. (2009)	Natural sediment	Unimpeded static percolation	$D_{15ss}/D_{85fs} \geq 15.4$
		Transition	$12 < D_{15ss}/D_{85fs} < 14$
		Bridging	$D_{15ss}/D_{85fs} \leq 10.6$
Huston, Fox (2015)	Natural sediment	Unimpeded static percolation	$D_{ss}(D_{fs}\sigma_{ss})^{-1} > 27$
		Bridging	$D_{ss}(D_{fs}\sigma_{ss})^{-1} < 27$
Dudill et al. (2016)	one particle size	Bridging	$2.5 \leq D_{ss}/D_{fs} \leq 3.3$
		Partially unimpeded static percolation	$5.56 \leq D_{ss}/D_{fs}$

up in rivers, lakes, or oceans. Several accidents in the world have contributed to significant environmental damage associated with mining accidents, either by dumping tailings or copper concentrate, both in water bodies. For example, Edroma (1974) reported copper concentrate in Lake George, which is 11 km downstream from a copper mine. The presence of copper is associated with leaks of copper concentrate due to pipeline failures and was transported by the Kamulikwezi River to the Rwenzori National Park and Lake George. Edroma (1974) found that the maximum concentration of copper concentrate was in the first few centimeters of the flood zone sediment column. Furthermore, spills reaching rivers, lakes, and oceans, and contaminated of the bed and hyporheic zone were reported by Van Niekerk, Viljoen (2005), Byrne et al. (2015), Yolcubal et al. (2016), and Carmo do et al. (2017).

In 2016 a rupture of a pipeline in the Blanco River, Saladillo-Chile, dumped 50 m^3 of copper concentrate. That day, the Blanco river stream-gaging station registered a flow of 10.0 m^3/s, so the maximum weight concentration of copper concentrate could be between 0.1 - 0.16%, affecting the El Sauce drinking water plant, located in the Los Andes city. This is one of the many spills that have affected the Blanco River over the years.

Nowadays, after a mining accident in Chile, companies only collect the mining materials deposited on the river banks and leave the infiltrated material in the riverbed. Environmental authorities, such as the Chilean Ministry of Environment, take samples of the water quality once the spill has occurred, and do so until the levels return to normal, but nobody takes samples of the sediments in the bed (Ambiente, 2016).

Los Andes Mountain range is a geomorphologic control of Chilean rivers in the north and central regions of the country, generating rivers with steep slopes and coarse and extended grain size distributions. According to Davis' (1899) classification, the Chilean rivers are young, whereas according to Rosgen's (1994) classification, the cross-sections are type A+ and A, i.e., the floodplains are small, and the scour-pool feature may be common. Niño (2002) reported slopes between 0.04 - 8.61 %, and median sediment size between 0.3-250 mm, and the material is well-sorted, i.e., the bed material consisted of gravel and sand.

Table 2.2 presents information on the characteristics of the sediments of Blanco and Aconcagua rivers in Chile (Niño, 2002; CENMA, 2008), that have been affected by copper concentrate spills. Gravel-bed rivers in Chile of the type that receives copper concentrate spills are macro-roughness flows, and this is observed taking into account the dimensionless parameter h/D_{90}. When this parameter is less than 10, the flow is considered macro-rough, and the flow resistance changes regarding the simple rough flow (Limerinos, 1970; Niño, 2002; García, 2008; Niño et al., 2018). The copper concentrate spill enters the flow through the surface of the alluvial flow and similarly infiltrates the bed, which is reproduced by the experimental

flume in this article.
For this reason, the purpose of this research is to experimentally characterize the suspension transport dynamics and the infiltration of the copper concentrate after its spills point in an open channel. There are no reports of this type in the literature, with sediments and copper concentrate, so this research proves to be novel.

2.2 Dimensional analysis

The diameter, density and cohesion of copper concentrate, as well as the diameter of the bed material and the flow parameters, should determine the depth of infiltration. Dimensional analysis was carried out through the Buckingham Theorem. Equation 2.1 shows that the dimensionless infiltration depth depends first on a relation between the diameter of copper concentrate and bed grains, D_{ic} and D_{js}, where i (or j) denote the grain size at which i (or j) percent is finer and c and s denote copper concentrate or sand, respectively, and the geometric standard deviations of the sediment, ($\sigma_{gs} = \sqrt{D_{84s}/D_{16s}}$), and copper concentrate, ($\sigma_{gc} = \sqrt{D_{84c}/D_{16c}}$). Second, there are hydraulic parameters such as particle Reynolds number, $Re_{p*} = (u_* D_{50s})/\nu$, where u_* is the shear velocity and ν is the kinematic viscosity, the dimensionless submerged weight of sediment and copper concentrate, $R = (\rho_s - \rho)/\rho$, and $R_c = (\rho_c - \rho)/\rho$, where ρ, ρ_s, and ρ_c are the densities of water, sediments, and copper concentrate, respectively, and dimensionless shear stress, $\tau_* = (u_*^2)/(gD_{50s}R)$. Third, there are the aspect ratios between width, B, and depth, H, of the flow with the diameter of sediment, and porosity of the bed, ϕ.
Note that $\frac{\rho_s - \rho}{\rho}$ and $\frac{\rho_c - \rho}{\rho}$ are constant because the densities of sediment, copper concentrate, and fluid are the same as in a natural river contaminated with copper concentrate in this research. In addition, the cohesion of the copper concentrate is constant in this research due to the fact that the copper concentrate does not change, so cohesion is not considered in the equation 2.1. On the other hand, $\frac{B}{D_{50s}}$, $\frac{H}{D_{50s}}$, and ϕ could change, but for the experimental conditions in this research, it is not possible to have great changes.

$$\frac{H_{perc}}{D_{\mathrm{ic}}} = f(\underbrace{\frac{D_{js}}{D_{\mathrm{ic}}}, \sigma_{gs}, \sigma_{gc},}_{1} \underbrace{\frac{u_* D_{50s}}{\nu}, \frac{\rho_s - \rho}{\rho}, \frac{\rho_c - \rho}{\rho}, \frac{u_*^2}{gD_{50s}R},}_{2} \underbrace{\frac{B}{D_{50s}}, \frac{H}{D_{50s}}, \phi)}_{3} \tag{2.1}$$

The dimensionless infiltration depth is, in principle, a function of 10 dimensionless numbers. Huston, Fox (2015) made a dimensional analysis of the infiltration of sand into gravel and could not find an influence of hydraulic parameters on the dimensionless infiltration depth. The infiltration of sand into gravel depends solely on the relation between the diameters of the sand and gravel. We explore the dimensionless parameters of equation 2.1 for copper concentrate in natural sediment, varying the values of the parameters i and j, respectively. The aim is to analyze the dynamics of a spill of copper concentrate in an alluvial flume and find dimensionless relationships that can be applied in the field.

Table 2.2: Sediment characteristics on mountain rivers in Chile and experimental research.

River	S(%)	D_{50} (mm)	D_{90} (mm)	h/D_{90}
Blanco Chile[a] [b]	4.03	58.0	244.0	1.4 - 7.2
Aconcagua in Blanco River Chile[a] [b]	7.8	88.3	299.8	3.7 - 7.0
Present experiments	0.007 – 4.7	0.94-2.12	10.0	2.0 - 4.1

[a] CENMA (2008)
[b] Niño (2002)

2.3 Materials and Methods

The experiments were conducted in an open channel 0.11 m wide, 3.0 m long, 0.15 m deep, and bed slope that varied between 0.007 and 0.047 (Figure 2.1). The copper concentrate was fed through an acrylic cone, 2.83 cm of diameter, with which we can simulate a pipeline failure. This system can pour a flow rate of 0.23 l/s of, copper concentrate for 7 s, and the net weight of copper concentrate was $W_{tot} = 2.8$ kg.
In this research, an immobile bed was considered, i.e., there is no bedload transport. The bed has two layers of sediment: gravel and sand (Figure 2.1). Gravel has always unimpeded static percolation because the copper concentrate is so small in size that only the sand can from bridges depending on the sand sizes. It was an analogy to represent the active layer and substrate of sediment in a natural alluvial flow (Parker, Klingeman, 1982). The sediment substrate has good gradation, and the size of sediment is smaller than the active layer of the sediment, but we subtract the gravel part. The surface layer is gravel, 20 mm thick, and has mean diameter of D_g= 10 mm. The subsurface layer is sand, of 30 mm thick, and has mean diameter, D_s, variable between 0.2 and 3.35 mm in different experiments. The density of both materials, gravel and sand, is 2.65 g/cm^3. Furthermore, we use copper concentrate of the Codelco-Andina mining company, Chile. Andina processes the material as a sulfide mineral. It has a characteristic diameter (D_{50}) $D_c = 40$ μm, a density of 4.2 g/cm^3 and approximately between 30 – 40 % is copper and the rest are 24 - 26 % iron, 24 - 27 % sulfur, 2.5 – 3.0 % aluminum, 0.3 % arsenic, and others components.
The relative depth, h/D_{90g}, is lower than 10, as observed in Table 2.2 and Table 2.3, i.e., they are macro-roughness flows, such as mountain rivers. For Aconcagua and Blanco rivers, h/D_{90g}, is 1.4 - 7.2. For the present experiments, h/D_{90g}, is 1.7- 4.1 (Table 2.2).

The copper concentrate is similar in size to silt, but its density is 1.6 times greater or more. Due to its physical properties, the copper concentrate is transported in suspension and deposited in the bed. Furthermore, the copper concentrate is poured with a concentration of 70% by weight, to avoid encapsulation. Since the copper concentrate is transported in suspension, the experimental arrangement has a mobile chute that conducts the suspended copper concentrate into a tank for collection, preventing recirculation of the concentrate in the system (Figure 2.1). There is a water reserve system, which becomes operational once the copper concentrate is poured into the channel, and stops operating when the suspended material passed downstream of the flume to the tank, and the mobile discharge returns to its initial state.

The instrumentation used were a Venturi pipe for flow measurement, a Nikon D3200 camera for image analysis of copper concentrate transport, and a Photron FASTCAM Mini UX50 camera that takes up of 2500 fps, for Particle Image Velocimetry (PIV) analysis. The grain

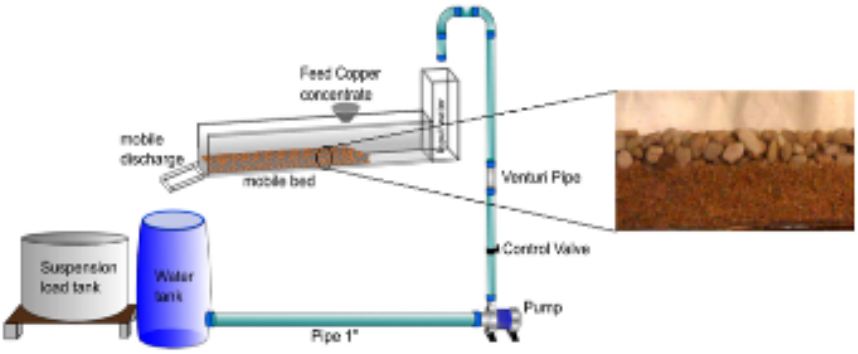

Figure 2.1: The experimental arrangement used in the study. The flume is an open channel that is recirculating or passes through a chute to a tank. The arrangement of the bed is with two layers of sediments. The surface layer is composed of gravel and the substrate layer of sand.

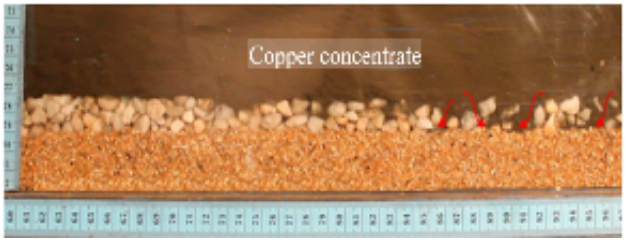

Figure 2.2: Transport of copper concentrate in open channels, the image was taken from the sidewall. The arrows in red show that the copper concentrate begins to percolate.

size distribution analysis of the copper concentrate was carried out in the Sedimentology Laboratory of the Universidad de Chile with a Malvern Mastersizer 2000 equipment.
The experimental setting was small, to control the discharge of copper concentrate in the experiments to a minimum so that there is no danger of spillage into the sewer system.

In this investigation, ten experiments were carried out. For each experiment, it took a week or two to measure the weight of copper concentrate in the bed, the one in the tank for the suspension, and the preparation for a new experiment. Table 2.3 summarizes the hydraulics flow parameters such as Q, discharge; h, depth; A, wetted area; V, section mean flow velocity; R_h, hydraulic radius; S, slope of the channel; $u_{*th} = \sqrt{gSR_h}$, theoretical bulk shear velocity; $Fr = V/\sqrt{gh}$, Froude number; g, gravitational acceleration; h/D_g, with D_g the gravel diameter and $\mathrm{Re} = Vh/\nu$, Reynolds number with ν the kinematic viscosity, and besides, the D_{50s} and D_{90s} of the sediment substrate. Figure 2.3 reports the grain size distribution curves of gravel, sand 5, 6, or 7 and copper concentrate. The gravel goes in the surface layer of the sediment bed, the sand goes into the substrate, and the copper concentrate is deposited in the bed. Experiment 9 had two types of sand, sand 7 in the first 1.75 m of length and sand 6 in the rest of the channel.

The copper concentrate suspension transport begins as soon as it was poured into the channel. After saturating the water column with the spill, infiltration of the copper concentrate begins moving towards the gravel layer, as shown in Figure 2.2. This figure is from the flume sidewall. However, the infiltration dynamics are representative of the flume cross-section. At the flume center, of course, the flow velocity is higher than in the sidewall. But in a series of experiments, we excavated the entire cross-section, and the infiltration depth was of the

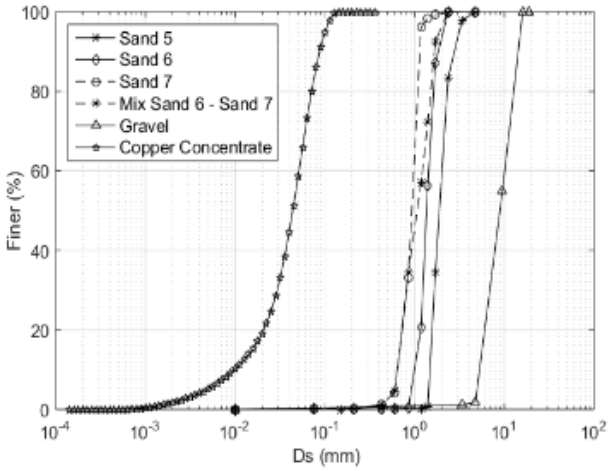

Figure 2.3: Grain size distributions of gravel, sands and copper concentrate.

Table 2.3: Hydraulic parameters and substrate sand characteristic for each experiment.

Exp	D_{50sand}	D_{84sand}	D_{90sand}	σ_{gsand}	Q	h	A	V	R_h	S	u_{*th}	Re	Fr	h/D_g
#	mm	mm	mm	-	l/s	m	m^2	m/s	m	-	m/s	-	-	-
1	-	-	-	-	0.61	0.03	0.0033	0.185	0.017	0.047	0.089	5507	0.34	2.0
2	-	-	-	-	0.61	0.03	0.0034	0.180	0.018	0.047	0.090	5507	0.33	1.7
3	-	-	-	-	0.61	0.03	0.0033	0.185	0.017	0.047	0.089	5507	0.34	1.7
4	1.36	1.67	1.85	1.23	1.95	0.03	0.0033	0.591	0.017	0.047	0.089	17604	1.09	1.7
5	2.12	3.03	3.20	1.44	1.95	0.043	0.0050	0.394	0.023	0.047	0.103	17604	0.59	2.7
6	0.94	1.12	1.15	1.26	1.82	0.057	0.0062	0.293	0.027	0.007	0.043	16458	0.39	3.4
7	1.36	1.67	1.85	1.23	1.82	0.057	0.0062	0.293	0.027	0.007	0.043	16458	0.39	3.4
8	0.94	1.12	1.15	1.26	2.45	0.067	0.0074	0.333	0.029	0.007	0.044	22158	0.41	4.1
9	0.94	1.12	1.15	1.26	2.30	0.063	0.0069	0.332	0.028	0.007	0.044	20764	0.42	3.9
	1.36	1.67	1.85	1.23										
10	1.08	1.57	1.66	1.68	2.50	0.053	0.0033	0.185	0.026	0.016	0.064	5507	0.34	3.2

same order of magnitude as in the sidewall.

On the other hand, the movement of the infiltrated material is mostly downstream but upstream, as well. The infiltration of the copper concentrate into the subsurface sands begins after the infiltration of copper concentrate into the surface layer is completed. The movement of copper concentrate into the sands are like fingers, i.e., the vertical motion dominated over the longitudinal motion. We have been able to identify that the infiltration process can be i) the formation of bridges or ii) the unimpeded static percolation, as has been reported in the literature for studies of gravel and sand.

The depths and speeds of infiltration of copper concentrate, and its evolution over time into the substrate sands, were measured by image processing. The measurement zone was located far enough from the pouring point, to ensure that the copper concentrate has infiltrated between the gravel layer and the base flow of the channel. Data acquisition was taken with the Nikon D3200 camera, and the MATLAB Image Processing Toolbox was used to perform the image analysis. images, composed of three channels, Red, Green, Blue (RGB), represent matrices. Each set of matrices is imported into the software and analyzed in grayscale, seeking for a better demarcation of the sand-copper concentration interface. In this way, the temporal and spatial evolution of the copper concentrate interface is quantified in the measurement area.

2.4 Results

2.4.1 Shear stress

Velocimetry was measured with Particle Image Velocimetry (PIV). The copper concentrate generated small changes in the roughness of the sediments. The shear stress, estimated with the fluctuations of velocities with the methodology proposed by Nikora et al. (2004) for a gravel bed, was analyzed defining the shear stress (τ_{tot}) such as: $\tau_{tot} = \mu(\partial\overline{u})/\partial z - \rho\left\langle\overline{u'w'}\right\rangle - \rho\langle\tilde{u}\tilde{w}\rangle$, i.e., the shear stress has three components that are: viscous ($\mu(\partial\overline{u})/\partial z$), turbulent ($-\rho\left\langle\overline{u'w'}\right\rangle$) and form-induced ($-\rho\langle\tilde{u}\tilde{w}\rangle$), where μ is the kinematic viscosity, $\overline{u}$ is the mean velocity, $u^{'}$ and $w^{'}$ are the velocity fluctuations in x and z components, respectively, $\tilde{u}$ and $\tilde{w}$ are the form-induced disturbance in the flow variables (where $\tilde{u} = \overline{u} - \langle\overline{u}\rangle$ and $\tilde{w} = \overline{w} - \langle\overline{w}\rangle$) and z is the vertical coordinate. Three planes were considered in the cross-section, at y/B =1/2, y/B =1/4 and y/B =1/8, P1, P2 and P3, respectively, where y is the transverse coordinate and B the channel width, to estimate average shear stress before and after the spill of copper concentrate. So the changes associated with the copper concentrate deposited into the bed were quantified. For experiment 9, the shear stresses measured in three planes are presented in Figure 2.4. Considering one symmetrical section, planes measured at y/B =1/4 and y/B =1/8 reflect the planes at y/B =3/4 and y/B =7/8. For each plane, there is one shear stress, and these values are associated with an effective area of the cross-section and, based on these, one weighted average. These considerations allowed estimating the average shear stress associated with the bed (not the walls) for each experiment, before and after the spill of copper concentrate. It was found that the average shear stress had decreased after the spill. The maximum decrease was 9%, and this effect may be related to the copper concentrate forming a cap between gravel and sand. Turbulence near the bed induces the resuspension process of the copper concentrate for a short time, and it reaches a steady-state where there was no resuspension, so the changes in the roughness are small.

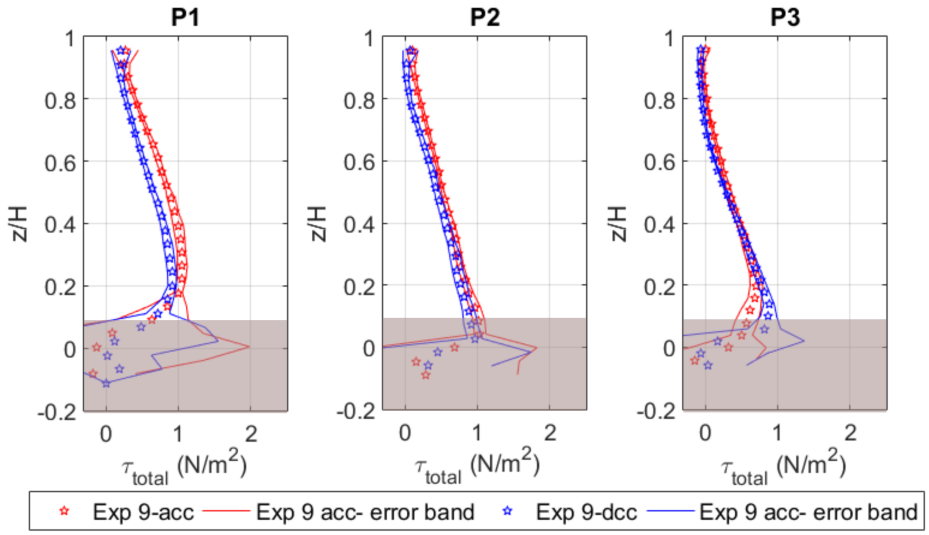

Figure 2.4: Total shear stress, before and after the spill of copper concentrate in Experiment 9. The colored area at the bottom is the gravel layer on the bed; bcc is before the spill and acc is after the spill.

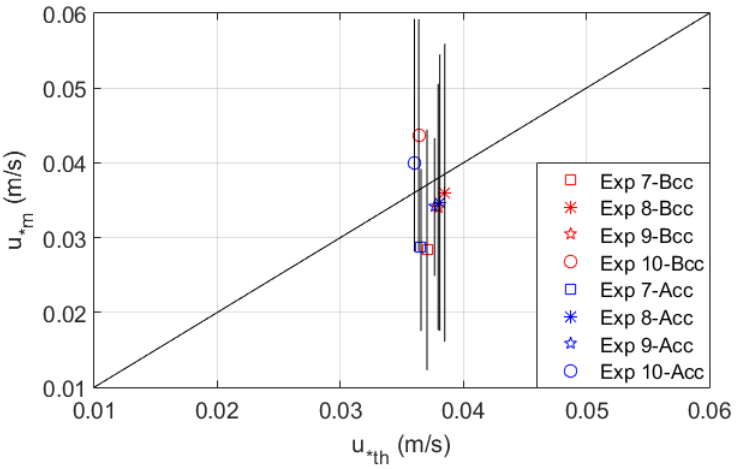

Figure 2.5: Relationship between u_{*m} and u_{*th} in the experimental flume.

The average shear velocities measured in the cross-section, u_{*m}, show a small underestimation concerning the theoretical bulk shear velocity, u_{*th}, before (bcc) and after (acc) the spill of copper concentrate (Figure 2.5). The black line is the ideal relationship between theoretical and measured results for shear velocity. Table 2.4 shows the shear velocity, u_{*m}, the particle Reynolds number measured, $Re_{p*m} = (u_{*m}D_s)/\nu$, and the dimensionless shear stress measured, $\tau_{*m} = u_{*m}^2/(gD_sR)$, before and after the spill of copper concentrate into the gravel bed.

Table 2.4: Experimental shear velocity and dimensionless experimental parameters.

Exp	u_{*m} (m/s)		Re_{p*m}		τ_{*m}	
#	bcc	acc	bcc	acc	bcc	acc
7	0.028	0.029	1.287	1.302	0.564	0.577
8	0.036	0.035	2.243	2.157	0.663	0.613
9	0.034	0.034	2.100	2.111	0.601	0.607
	0.034	0.034	1.882	1.892	0.671	0.678
10	0.044	0.040	3.076	2.816	0.864	0.724
	0.044	0.040	2.499	2.288	1.063	0.891

2.4.2 Spill of copper concentrate

In each experiment the suspension load leaving the system, the infiltration in the bed and the grain size distribution of copper concentrate, suspended and infiltrated, were measured. The copper concentrate bed deposit was measured in seven sections: one section upstream of the spill, in section at the spill, and the rest covering the channel downstream of the spill. Figure 2.6 shows the weight per unit bed area of copper concentrate deposited in each section, Q_{Bed}, made dimensionless with the weight of the total input of copper concentrate per unit bed area of the flume, Q_{Tot}, as a function of the longitudinal coordinate made dimensionless with the diameter of the copper concentrate that feeds the acrylic cone, X_*. Upstream of the spill area of copper concentrate, at a dimensionless distance of 17.7, the copper concentrate was found to infiltrate into the substrate. The blue box in Figure 2.6 shows the spill area. Also, near the spill zone, the deposit is between 30 - 60% of the total weight input of the

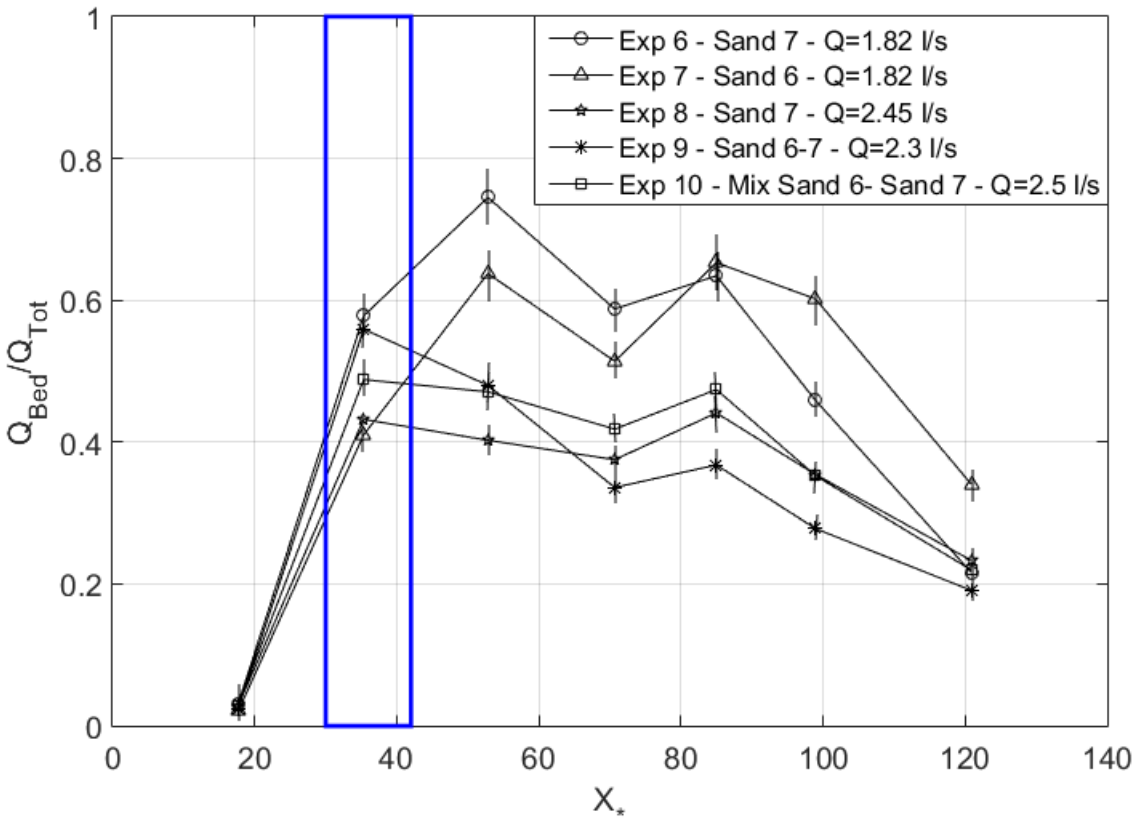

Figure 2.6: Distribution of dimensionless weight per unit area of copper concentrate along the channel after the spill. The blue box shows the spill area.

copper concentrate, i.e., on average, the 50% of the weight of the copper concentrate is transported in suspension downstream from X_* >120, or 100 flow depths downstream from the point where the spill was generated. This research has not found a direct relationship between that percentage and sand diameter or discharge.

Table 2.5 summarizes the weight of the copper concentrate in suspension that leaves the channel, W_{susp}, maximum, mean and minimum depths of infiltration, $H_{perc-max}$, $H_{perc-mean}$, $H_{perc-min}$, standard deviations of depth of infiltration, $\sigma_{H_{perc}}$, with their respective grain size distribution, where D_{50c} is the mean diameter of copper concentrate, and the total weight of infiltration, W_{perc}, respectively. Experiments 1, 2 and 3 were only taken into account to understand the dynamics of the phenomenon, make modifications in the system and improve the quality of the measured data. In these preliminary experiments, we found that the concentration of copper concentrate in the water column is variable in space and time, i.e., the suspended copper concentration was getting higher in the lower part of the flow from its pouring point until the beginning of the infiltration. Then, the suspended load decreases, since the re-entrainment of the copper concentrate were low or negligible.

Note that experiments 6 and 8 have the same type of sand (sand 7), different discharge flow, and similar infiltration depths (Table 2.3 and Table 2.5). Likewise, it is worth noting that although both types of sand (sand 6 and 7) were poorly graded, sand 7 having a smaller grain size, in turn, produces smaller pore sizes, which prevent the phenomenon of unimpeded static percolation. The increases in flow rate imply an increase in the ratio W_{Sus}/W_{Tot},

Table 2.5: Results on weight in suspension and bed infiltration of copper concentration, its mean diameters and infiltration depth after the spill.

Exp	Sand	Suspension		Bed		$H_{perc-max}$	$H_{perc-mean}$	$H_{perc-min}$	σ_{Hperc}
#	Type	D_{50c} (μm)	W_{susp} (gr)	D_{50c} (μm)	W_{perc} (gr)	(mm)	(mm)	(mm)	(-)
4	6	22.3	1898.8	42.6	739.1	14.6	-	-	-
5	5	17.5	1866.5	43.8	810.91	30.0*	-	-	-
6	7	14.5	1053.6	61.8	1748.1	5.7	1.1	0	1.1
7	6	12.9	1213.1	45.4	1611.0	30.0*	9.2	0	8.1
8	7	16.0	1556.6	62.3	1174.7	5.7	1.2	0	1.4
9+	7	20.6	1615.1	61.6	667.1	16.1	3.3	0	3.7
	6			55.2	501.6	30.0*	11.0	0	8.3
10+	Mix sand 6 and sand 7	16.4	1433.2	70.4	999.0	8.1	1.74	0	1.5
				57.2	163.7	30.0*	-	-	-

* These infiltrations are limited to the channel bottom which is 30 mm.
+ We could see both types of movement, bridging and unimpeded static percolation.

and a decrease in the ratio W_{Bed}/W_{Tot}, where W_{Sus}, W_{Bed} and W_{Tot} are the weight of copper concentrate in suspension, in the bed and total, respectively. However, no dependence was found between discharge or flow parameters and the distribution of copper concentrate deposited in the bed (Figure 2.7). Beschta, Jackson (1979), Carling (1984) and Huston, Fox (2015) found the same effect with sand and gravel. Figure 2.7 does not show dependence between H_{perc}/D_{50c} with Re_{p*m} and τ_{*m}. For this reason, the analysis of infiltration depth is based on the geometric relationships between sizes of sediment and copper concentrate.

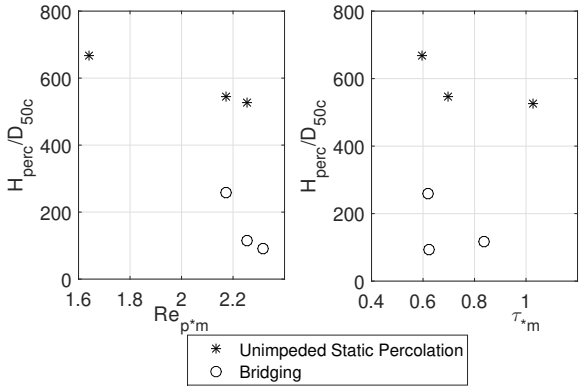

Figure 2.7: Dimensionless infiltration depth versus hydraulic dimensionless parameters: Re_{p*m} and τ_{*m}.

2.4.3 Percolation depth of copper concentrate

Geometric relations such as: H_{perc}/D_{16c} vs D_{84s}/D_{16c}, H_{perc}/D_{50c} vs D_{90s}/D_{50c} and H_{perc}/D_{50c} vs $d_{50c}/(D_{50s}\sigma_{gc})$, have allowed finding different thresholds to characterize unimpeded static percolation and bridge formation in the copper concentrate and sands (Figure 2.8 and Table 2.6). The dimensionless mean geometric relationships such as: $H_{percmean}/D_{16c}$, $(H_{percmean}+\sigma)/D_{16c}$, $(H_{percmean}-\sigma)/D_{16c}$, $H_{percmean}/D_{50c}$, $(H_{percmean}+\sigma)/D_{50c}$ and $(H_{percmean}-\sigma)/D_{50c}$, are reported in Table 2.7, where $H_{percmean}$ is the mean value of the percolation depth, and

σ is the standard deviation of the percolation depth. Table 2.8 presents the geometric dimensionless relationships for the maximum percolation, such as: H_{perc}/D_{16c}, H_{perc}/D_{50c}, D_{84s}/D_{16c}, $D_{50c}/(D_{50s}\sigma_{gc})$ and D_{90s}/D_{50c}. The thresholds for mean percolation with their respective standard deviations are shown in Figure 2.8a-c. The relations: $D_{84s}/D_{16c} < 71$, $D_{90s}/D_{50c} < 30$ or $D_{50c}/(D_{50s}\sigma_{gc}) > 0.022$, are thresholds for bridging. Figure 2.8d-f shows the intervals that define the thresholds for the maximum value for both types of infiltration. We thought that, for unimpeded static percolation, the copper concentrate was dragged in the bottom of the flume (vertical arrows in Figure 2.8d-f), but we do not know whether the maximum percolation is, perhaps, a certain distance below the bottom of the flume. That is why blue boxes are transition zones, i.e., the infiltration of the copper concentrate may be unimpeded static percolation or bridging.

Table 2.6: Experimental thresholds for maximum infiltration.

Types of movement	Criterion
Unimpeded static percolation	$D_{84s}/D_16c > 115$
	$D_{90s}/D_{50c} < 47$
	$D_{50c}/(D_{50s}\sigma_{gc}) < 0.014$
Bridging	$D_{84s}/D_{16c} < 60$
	$D_{90s}/D_{50c} < 28$
	$D_{50c}/(D_{50s}\sigma_{gc}) > 0.025$

Table 2.7: Summary of dimensionless geometric relationship of mean and standard deviations of the copper concentrate infiltration depth.

Exp	$H_{percmean}/D_{16c}$	$(H_{percmean}+\sigma)/D_{16c}$	$(H_{percmean}-\sigma)/D_{16c}$	$H_{percmean}/D_{50c}$	$(H_{percmean}+\sigma)/D_{50c}$	$(H_{percmean}-\sigma)/D_{50c}$
6	35.48	70.97	0.00	17.74	35.48	0.00
7	657.14	1,235.71	78.57	204.44	384.44	24.44
8	42.86	92.86	-7.14	19.35	41.94	-3.23
9	206.25	437.50	-25.00	53.23	112.90	-6.45
	478.26	839.13	117.39	200.00	350.91	49.09
10	62.14	115.71	8.57	24.86	46.29	3.43
	NaN	NaN	NaN	NaN	NaN	NaN

Table 2.8: Summary of the geometric dimensionless relationship for the maximum infiltration depth.

Exp	H_{perc}/D_{16c}	H_{perc}/D_{50c}	D_{84s}/D_{16c}	$D_{50c}/(D_{50s}\sigma_{gc})$	D_{90s}/D_{50c}
4	973.33	339.53	111.33	0.0140	43.02
5	1764.71	681.82	178.24	0.0098	72.73
6	183.87	91.94	36.13	0.0357	18.55
7	2142.86	666.67	119.29	0.0131	41.11
8	203.57	91.94	40.00	0.0328	18.55
9	1,006.25	259.68	70.00	0.0230	18.55
	1,304.35	545.45	72.61	0.0190	33.64
10	289.29	115.71	57.14	0.0296	24.14
	1,200.00	526.32	65.20	0.0232	29.81

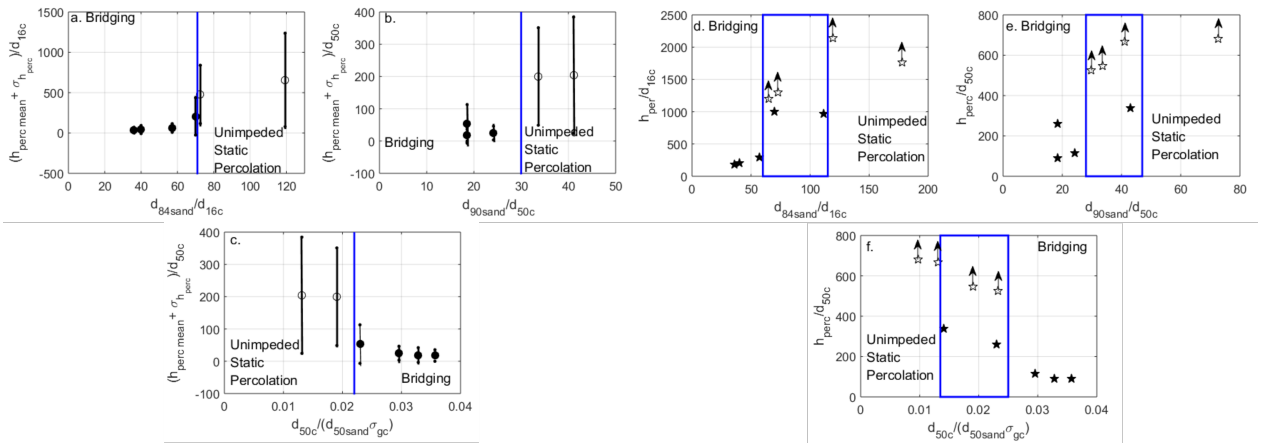

Figure 2.8: Geometric relationships of mean and standard deviations of: a. $H_{percmean}/D_{16c}$ vs D_{84s}/D_{16c}, b. $H_{percmean}/D_{50c}$ vs D_{90s}/D_{50c}, c. $H_{percmean}/D_{50c}$ vs $D_{50c}/(D_{50s}\sigma_{gc})$ of the percolation of copper concentrate into sands
. Vertical lines are plus and minus the standard deviations. d. H_{perc}/D_{16c} vs D_{84s}/D_{16c}, e. H_{perc}/D_{50c} vs D_{90s}/D_{50c}, f. $H_{perc}/D_{50c} vs D_{50c}/(D_{50s}\sigma_{gc})$ of the maximum percolation of copper concentrate into sands.

2.5 Discussion

The point discharge of a hyper-concentrated mixture of fine particles in an alluvial stream generates a gradual dilution of the mixture so that it causes transport in suspension. After reaching a critical concentration, the deposition of the fine material in the bed begins. The material deposited in the bed can be entrained or infiltrated. This dynamic is analyzed by two approaches.

2.5.1 Suspension and entrainment

A particle is transported in suspension if the flow velocity fluctuations in the vertical component are greater than the fall velocity of the particle (Rijn van, 1984; Niño et al., 2003). On the other hand, a particle deposited into the bed can be entrained into suspension transport. Sediment entrainment is associated with coherent flow structures and strong fluid ejections from the bed (Jackson, 1976; García et al., 1995; Niño, García, 1996). However, in this study, the entrainment rate of copper concentrate in suspension transport declines in a short time-span. This behavior is associated with the gravel layer becoming a protective layer for the copper concentrate deposited into them. This dynamic is analogous to the effect of sands hiding between the gravels in a river bed (Parker, Klingeman, 1982). Additionally, the density of the copper concentrate is greater than that of sands, silts and clays, which means that the depositional flux is greater than the flux of the entrainment particles. In fact, lower because of the density of the particles (García, Parker, 1991). Therefore, reincorporating copper concentrate in suspension transport requires shear stresses that can transport the gravel of the active layer as a bedload (Cui, Parker, 1998), and, thus, the copper concentrate particles are exposed to the flow.
The density of the copper concentrate is the main factor in reducing the entrainment in a short time. Assume a case of fine sediment poured as a mixture of water and particles, but the density of the particles is less than that of the copper concentrate. Due to the type of

spill, suspended transport and deposition occurs. On the other hand, considering that the fall velocity of the fine sediment is lower than the copper concentrate, the transport in suspension is greater in the case of fine sediment. Fine sediment deposited on the bed, unimpeded static percolation and bridging layers can occur. However, the infiltration depth might be lower than that of the copper concentrate, according to Beschta, Jackson (1979), Wooster et al. (2008), Gibson et al. (2009), Huston, Fox (2015), Dudill et al. (2016), and others.

2.5.2 Percolation of copper concentrate

Edroma (1974); Govil et al. (2012); Yolcubal et al. (2016) reported heavy metals in the sediments of rivers and lakes, which could be caused by mining accidents or discharges of industrial effluents. For these reasons, it is crucial to estimate the percolation depth, even more so, when the fine sediment is toxic, so in this research, the infiltration of copper concentrate was analyzed similarly to the phenomenon of the infiltration of sand in gravel beds, i.e., considering the relationships proposed by Beschta, Jackson (1979), Diplas, Parker (1985), Iseya, Ikeda (1987), Lisle (1989), Gibson et al. (2009), Huston, Fox (2015), Núñez-González et al. (2016), Dudill et al. (2016). Base on Beschta, Jackson (1979), Diplas, Parker (1985), and Iseya, Ikeda (1987), who gave the maximum percolation of the whole set of dimensionless relationships for sand into gravel, from 2 to 5 times the d_{90} of the coarse sediment. If we applied such relationship to the percolation of copper concentrate into sands, the percolation should be between 2.3 mm and 5.75 mm, much less than the percolation reported here (Tables 2.6 and 2.7). The underestimation is at least a factor three times less than the percolation depth of copper concentrate. On the other hand, the thresholds proposed by Gibson et al. (2010) and Huston, Fox (2015) do not adequately characterize the unimpeded static percolation and bridging layers for the copper concentrate into sands. So, the geometric relationships found in this paper are relevant. For that, Figure 2.8 presents a characterization of the infiltration depth of the copper concentrate, shown for both the average and the maximum infiltration.
On the other hand, we observed that the greatest amount of copper concentrate is found within a distance downwards a few diameters from the sands and decreases with depth. Both behaviors were observed by Wooster et al. (2008) and Cui et al. (2008) in flume experiments with an immobile bed of gravels and sand as fine sediment.
Gravel rivers in nival climates have maximum flows in spring, so they have a stable bed most of the year, and, in this case, the infiltration of a mining accident will be in immobile beds. However, during high flow periods or spring snow-melting flows, bedload transport occurs. On these occasions, there will be entrainment of copper concentrate that infiltrated in the past.

2.5.3 Copper concentrate in natural rivers

In 2016, an observer filmed the rupture of a pipeline in the Blanco River, Saladillo-Chile, ($https://youtu.be/_Ea-FKcUaUU?t = 20$), and the video showed a spill similar to that of our experiments. What is difference is the width of the river compared to the experimental flume. In the video, the spill is from the right bank. Downstream from that point, the concentration of copper concentrate near the wall decreases, and in the center of the river it increases, until the concentration in the cross-section is uniform due to turbulence, according to (Fischer et al., 1979). In the experiment, the spill is in the center of the cross-section, so

downstream, the concentration in the center decreases, and near the wall, it increases until the concentration is uniform in the cross-section. The length of the complete mixing in the cross-section was $l \sim 50$ m for the Blanco River, whereas in the experimental flume, it is approximately 0.7 m. Hence, the ratio l/B for the Blanco river is 5.0 and for the experiment is 6.6, i.e., the ratios have the same order of magnitude, so the experiment manages to represent the natural conditions. Therfore, we can analyze the dynamics of copper concentrate spills in a small flume, without losing the generality of a real spill.
According to Edroma (1974), the maximum distance from the location of a copper concentrate spill in a river would be at least 11 km because that is distance between Lake George and the location of the mining accident on the Kamulinkwezi River.
During high flow periods or snow-melting flows, the entrainment of the copper concentrate as bedload or suspended load will transfer the metals downstream. Of course, the concentration of copper concentrate will decrease as it moves away from the source, and as the tributaries join the main river, they will do so even more.

2.6 Conclusions

We have characterized the dynamics of copper concentrate when there is a spill in an open channel with alluvial sediment in the bed. Furthermore, we can deduce that these dynamics in an alluvial river are similar due to the experimental configuration considered: real copper concentrate, natural sediment, and the infiltration that does not depend on the flow velocity. The bed in our experiment is gravel in the layer in contact with the flow and sand beneath. Initially, the transport of the copper concentrate is in suspension. However, due to its high specific gravity, the sedimentation process is generated, wich induces the transport of the copper concentrate into the gravel and the infiltration into the sands. On the other hand, we did not find a dependence between flow parameters and the distribution of the copper concentrate deposited in the bed and its infiltration depth. For coarse-grained sediments, the infiltration of the copper concentrate would be larger, reaching a state of unimpeded static percolation. Moreover, when the size of the granular material is small, the bridge layer or seal can prevent free movement in sand of the copper concentrate. This research has allowed us to characterize dimensionless infiltration: $D_{84s}/D_{16c} < 60$ or $D_{90s}/D_{50c} < 28$ or $D_{50c}/(D_{50s}\sigma_{gc}) > 0.025$, tend to form bridge layers, and $D_{84s}/D_{16c} > 115$ or $D_{90s}/D_{50c} > 47$ or $D_{50c}/(D_{50s}\sigma_{gc}) < 0.014$, tend to obtain unimpeded static percolation. These relationships are proposed for the maximum infiltration. The relations $D_{84s}/D_{16c} < 71$ or $D_{90s}/D_{50c} < 30$ or $D_{50c}/(D_{50s}\sigma_{gc}) > 0.022$ give a threshold to characterize the transition of the mean infiltration depth.
These analyses are valid in the laboratory and natural rivers. The difference is that in rivers with high flow velocity, the affected length might be greater than in the laboratory, but the infiltration phenomenon is similar. For all experiments we found copper concentrate upstream of the spill zone. Thus, the same effect will exist in natural rivers after a mining accident. In the experiments, for velocities greater than 0.36 m/s dominates the suspension transport, i.e., more than 55% of the copper concentrate travels in suspension for longer distances than the flume, but eventually, in a river, all of the copper concentrates would deposit due to the high density of the copper concentrate. Moreover, in all experiments near the spill zone, we observed that approximately 50% of Q_{Bed}/Q_{Tot} is deposited into the bed.
When a spill of copper concentrate occurs in an alluvial river, the largest deposit of copper concentrate can be found in the first centimeters of the bed, and it can get unimpeded static

percolation of the copper concentrate, where the infiltration can reach much greater depth. There would only be entrainment in suspension of the copper concentrate when there are large flows in the river, capable of transporting the gravel from the active layer, which acts as a protective layer of the fine sediments and copper concentrate. This research shows that management protocols after a mining accident must consider that the interstitial spaces of the gravel have copper concentrate and could be resuspended by floods or spring snowmelt discharges.

It remains to be analyzed, as future work, the infiltration and the vertical gradational variability of copper concentrate in natural rivers, and evaluate the decrease with depth reported by Lisle (1989), Diplas, Parker (1985), Cui et al. (2008) and Wooster et al. (2008). The analysis of contaminants in the hyporheic zone will also be considered.

Chapter 3

Flow–Sediment Turbulent Ejections: Interaction between Surface and Subsurface Flow in Gravel-Bed Contaminated by Fine Sediment

This chapter has been published in Water journal (2020). Bustamante-Penagos N. y Niño Yarko. doi: 10.3390/w12061589

Abstract
Several researchers have studied turbulent structures, such as ejections, sweeps, and outwards and inwards interactions in flumes, where the streamwise velocity dominates over vertical and transversal velocities. However, this research presents an experimental study in which there are ejections associated with the interchange between surface and subsurface water, where the vertical velocity dominates over the streamwise component. The experiment is related to a surface alluvial stream that is polluted with fine sediment, which is percolated into the bed. The subsurface flow is modified by a lower permeability associated with the fine sediment and emerges to the surface current. Quasi-steady ejections are produced that drag fine sediment into the surface flow. Particle image velocimetry (PIV) measured the velocity field before and after the ejection. The velocity data were analyzed by scatter plots, power spectra, and wavelet analysis of turbulent fluctuations, finding changes in the distribution of turbulence interactions with and without the presence of fine deposits. The flow sediment ejection changes the patterns of turbulent structures and the distribution of the turbulence interactions that have been reported in open channels without subsurface flows.

3.1 Introduction

Landslides, volcanos, or anthropogenic changes may modify the availability of fine sediment in rivers, reservoirs, or lakes (Julien, 2010). Fine sediment can cause pollution in gravel beds. This contamination has a high environmental impact because the porosity of the gravel beds

is a reservoir for the deposition of fine sediment (Cui, Parker, 1998). The intrusion of fine sediment into gravel bed streams generates changes in the hyporheic exchange, nutrients cycling, low oxygenation of fish eggs, etc. (Beschta, Jackson, 1979; Diplas, Parker, 1985; Lisle, 1989). Additionally, the hyporreic zone also have an important coupling between the subsurface groundwater system and surface water, such as rivers or lakes and floodplains. This exchange is through the porous sediment, and it is characterized by the circulation of surface water into the alluvium and back to the river bed (Tonina, Buffington, 2009).
Moreover, fine sediments can move in suspension when the turbulent eddies have upward velocity components exceeding the fall velocity of fine sediments (Bagnold, 1966). An increase in grain roughness can generate an increase in the vertical intensity of turbulence (Jackson, 1976). Moreover, strong upward turbulent ejections could provide the vertical anisotropy needed for suspension transport and the entrainment of the fine sediment (Jackson, 1976; Niño, García, 1996; Niño et al., 2003). In addition, the turbulent structures in smooth flumes have been studied by Tamburrino, Gulliver (1999); Adrian (2007); Zhong et al. (2015, 2016) and others, showing coherent structures such as individual hairpin vortices, which have a small scale motion $l \sim h$, hairpin vortices that have a large scale motion $l \sim 3h$, and super streamwise vortices, which have a super scale motion $l > 10h$, where l is the streamwise scale of the vortices and h is the water depth. However, ejections in a rough-bed are smaller near the bed and the secondary currents can change the ejection patterns (Nakagawa et al., 1991). Furthermore, several researchers such as Niño, Musalem (2000); Sambrook Smith, Nicholas (2005); Cooper et al. (2018); Adrian (2007); Wallace (2016) have investigated turbulence characteristics considering a Cartesian plane with streamwise velocity fluctuations, $u^{'}$, and vertical velocity fluctuations, $w^{'}$, where the interaction in the second and fourth quadrant (ejections $u^{'} < 0$ & $w^{'} > 0$ and sweeps $u^{'} > 0$ & $w^{'} < 0$), respectively, are more frequent than the interactions in the first and third quadrants (outward interaction $u^{'} > 0$ & $w^{'} > 0$ and inward interaction $u^{'} < 0$ & $w^{'} < 0$), respectively, because of the mean shear stress is positive (i.e., $\overline{u^{'}w^{'}} < 0$).
Experimentally, researchers have used acoustic Doppler velocimetry (ADV), particle image velocimetry (PIV), laser Doppler velocimetry (LDA), or ultrasonic Doppler velocimeter (UDV) for the acquisition of velocity data. Niño, Musalem (2000) used ADV for characterizing the turbulence interactions in a sand bed, reporting ejections and sweeps as the most frequent turbulence interactions. Niño, Musalem (2000) also reported that the sweeps are more efficient for the entrainment of the particles into suspension than ejections. Sambrook Smith, Nicholas (2005), Cooper et al. (2018), and Chen et al. (2019) implemented PIV to characterize the flow field and the turbulence properties. Sambrook Smith, Nicholas (2005) experimented with the deposition of sand on gravel beds. They reported high velocities and high shear stresses that occur at the level of the crest of the major roughness elements and in their lee side; in addition, interactions such as sweeps and ejections are less frequent when roughness decreases, i.e., the main effect of fine sediment deposited in a gravel bed is to reduce the vertical velocities' gradients and shear stresses near the bed over the sand on the gravel bed. The roughness and the flow depth can modify the turbulent structures at shallow flow conditions Roussinova (2009). Roussinova (2009) compared results for rough and smooth walls and found that the magnitude of the turbulence quantities are higher in the case of the rough wall, ejection events are prevalent over sweeps and in smooth wall cases, and there are ejections and sweeps in the vicinity of the hairpin vortex.
Manes et al. (2009) compared the turbulence structure for permeable and impermeable beds in open channels, finding that large scale eddies generated within the surface flow have

influence in the subsurface flow, and they think that it must be associated with pressure fluctuations. Fourier series are often used to discuss the properties of a turbulent flow field (García, García, 2006; Bailly, Comte-Bellot, 2015). The frequency analysis, for example, is derived from the Fourier spectrum. However, this analysis is for stationary signals and the Fourier transformation has no localization property, i.e., if a signal changes at one position, then the transform changes without the position of the change could be recognized "at a glance" (Bronshtein et al., 2007; Addison et al., 2002). For unsteady signals that have finite duration, such as in geophysical processes and hydrology, the wavelet transform and the cross wavelet transform are excellent tools for analyzing the physical relationships between the time series (Bendat, Piersol, 2010; Grinsted et al., 2004). However, the open channel turbulent velocity fluctuations have been analyzed by Chen et al. (2019) considering the wavelet coherency, i.e., measuring the wavelet correlation between two velocity series at a frequency f on a scale from zero to unity, finding that the wavelet analysis identified the scale of motions and the time of its occurrence.
The present study characterizes the turbulence structures associated with the interchange between subsurface and surface flows due to fine sediment, pumicite, deposited into the interstitial space, the pores of a gravel bed. Particle image velocimetry (PIV) was employed to measure the velocity field before and after the fine sediment was deposited. The velocity data were analyzed by a scatter plot of turbulent fluctuation, Fourier, and wavelet analysis, finding changes in the distribution of turbulence interactions for a flume with and without fine sediment deposits.

3.2 Materials and Methods

Experiments were carried out in an open channel with a sediment bed. With this experiment setup, it was possible to measure independently the surface and subsurface flow. In this research, an immobile bed was considered. The fine material with which the bed is polluted is pumicite, or natural pozzolan, a raw material of minute grains of volcanic glass and ashes with the characteristics of clay.

3.2.1 Experimental Set Up

The experimental facility is an open channel, 0.03 m wide, 0.58 m long, and 0.63 m deep. The facility is divided into three parts. Upstream are the surface and subsurface input flows and the location of the seeding particles for PIV. At the center of the structure are the open channel, the bed, the point where the pumicite mixture is spilled, and the PIV measurement area. Downstream are the surface and subsurface output discharges (Figure 3.1a). The sediment bed has two layers of sediment. The surface layer is of gravel, 20 mm thick and median diameter $D_g = 10$ mm, and the subsurface layer is of fine gravel, 390 mm thick, and mean diameter of $D_s = 2.45$ mm (Figure 3.1b). The grain size distributions of sediment are shown in Figure 3.2. The density of both materials, gravel and fine gravel, is 2.65 g/cm^3, whereas the pumicite has a characteristic diameter (D_{50}) of $D_c = 0.12$ mm (Figure 3.2) and a density of 1.7 g/cm^3. The pumicite was fed through an acrylic cone in the free surface, of 1.0 cm of diameter, during 6 s. The net weight of pumicite was 284.2 g for the experiments. Such feeding can simulate a soil failure that falls into the river. Furthermore, the pumicite

is poured with a concentration of 57% by weight in water.

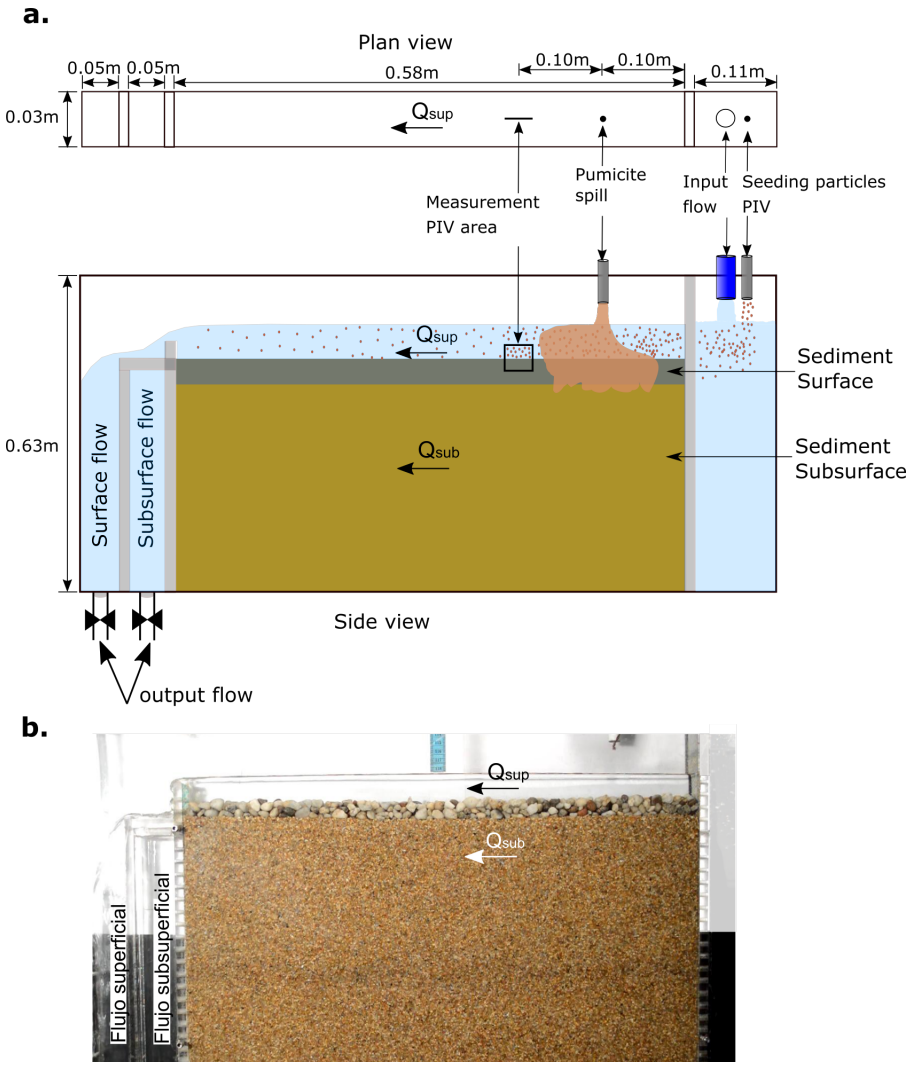

Figure 3.1: (**a**) experimental scheme used in the study; (**b**) experimental flume. The sediment column is used to measure high percorlations of fine sediment (pumicite) and subsurface flow. The surface flow rate is Q_{sur} and subsurface flow is Q_{sub}.

The measurement of flow rates was through volumetric gauges for the surface, Q_{sur}, and subsurface, Q_{sub}, flows in the experiments. A Photron FASTCAM Mini UX50 camera (San Diego, CA, USA) was used for Particle Image Velocimetry. This camera takes up to 2500 fps. A Nikon D3200 camera (Tokyo, Japan) was used for percolation analysis of pumicite. The Malvern Master Sizer 2000 equipment (Malvern, United Kingdom) of the Laboratory of Sedimentology of Universidad de Chile was used for measurement of the grain size distribution of pumicite. Experiments with several flow rates Q_{sur} and Q_{sub} are presented in Bustamante-Penagos, Niño (2018, 2019) for percolation of a variety of fine sediments, among them with pumicite. The experiments in this article are two, for the flow rates $Q_{sur} = 0.088$ l/s and $Q_{sub} = 0.008$ l/s. One with uniform flow with a friction slope $S_f = 0.017$, and water depth $H = 67$ mm, without fine sediment (E0) and the other of the same hydrodynamics conditions but with the spill of the fine sediment (E1). The article focuses, in this way, on the interaction

between subsurface and surface flows due to the deposition of fine sediment in the bed by measuring turbulence in the surface flow.

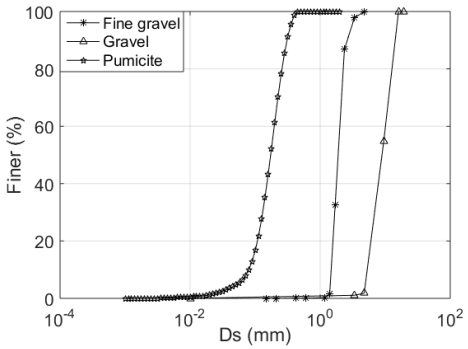

Figure 3.2: The grain size distribution of sediments used in the study.

3.2.2 Velocities

PIV was implemented to measure the flow field. The PIV particle tracers were of diameter 0.12 mm and density 1.7 g/cm^3. The flow was illuminated with a lamp with power of 18 W. The particle tracers are poured dry in low quantity in the stilling tank. Furthermore, for these conditions, the PIV particles are a good tracer because these particles only can move in suspension. Image acquisition was with the Fastcam Mini UX50 camera. It was implemented taking 250 fps during 140 s, before and after the spill of pumicite mixture, in the center of the cross section.

The velocity data were analyzed considering three methodologies. The first methodology is the estimation of the mean shear stress profile with the fluctuations of velocities with the spatially averaged open channel flow methodology proposed by Nikora et al. Nikora et al. (2004). It was analyzed defining the total shear stress such as:

$$\tau_{tot} = \mu(\partial\overline{u})/\partial z - \rho\left\langle\overline{u'w'}\right\rangle - \rho\left\langle\tilde{u}\tilde{w}\right\rangle, \tag{3.1}$$

i.e., the mean shear stress has three components which are: viscous ($\mu(\partial\overline{u})/\partial z$), turbulent ($-\rho\left\langle\overline{u'w'}\right\rangle$), and form-induced ($-\rho\left\langle\tilde{u}\tilde{w}\right\rangle$), where μ is the kinematic viscosity, $\overline{u}$ is the mean velocity, $u^{'}$ and $w^{'}$ are the velocity fluctuations in x (streamwise) and z (vertical) components, respectively. $\tilde{u}$ and $\tilde{w}$ are the form-induced disturbance in the flow variables (where $\tilde{u} = \overline{u} - \langle\overline{u}\rangle$ and $\tilde{w} = \overline{w} - \langle\overline{w}\rangle$), x is the streamwise coordinate and z is the vertical coordinate. In addition, the spatial average mean velocity, $<\overline{u}>(z)$, results from this methodology. In Equation (3.1), the overbar means temporal average and the angular brackets mean spatial averages.

The second methodology considers the scatter plots of velocity fluctuations u' and w', which were analyzed considering that they could be represented by an ellipse, such as Equation (3.2), where α, Ra and Rb are the angle of rotation, major axis and minor axis, respectively Szlapczynski, Szlapczynska (2016). Parameter α is obtained as the slope of a linear fit for the scatter plot between u' and w':

$$\frac{(x \cdot cos(\alpha) + y \cdot sin(\alpha))^2}{Ra^2} + \frac{(x \cdot sin(\alpha) + y \cdot cos(\alpha))^2}{Rb^2} = 1 \tag{3.2}$$

Additionally, Niño and Musalem Niño, Musalem (2000) and Wallace Wallace (2016) measured the intensity of the ejections and sweeps in a measurement at one point by the parameter $K = u'w'/ < u'w' >$. In this research, we have considered the parameter as: $K' = -K = -u'w'/ \mid u'w' \mid$. The percentage of distribution of the K' parameter in an area of 73 mm $\times$ 68 mm at one point x and z of the experiment E0 is presented in Figure 3.3, where K'_{90} and K'_{10} are associated with the 10th and 90th percentiles of K', respectively. After finding the pairs $(u^{'}, w^{'})$ associated with K'_{90} and K'_{10}, the Ra and Rb can be defined. The methodology used for characterizing the ellipses is presented in Figure 3.4.

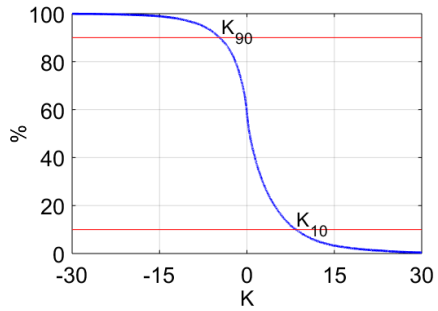

Figure 3.3: Percentage of distribution of parameter K.

The third methodology was Fourier and wavelet analysis. The wavelet analysis has been implemented by Torrence, Compo (1998); Addison et al. (2002); Cohen, Walden (2010); Chen et al. (2019); Grinsted et al. (2004) and others, in order to analyze different physical phenomena. In this research, the Morlet function was used as the mother wavelet. Morlet wavelet mother is a powerful tool for data analysis of low-oscillation functions (Addison et al., 2002).

3.3 Results

Hydraulic parameters for the experiment setup are the Froude number, $Fr = U/\sqrt{gH}$, Reynolds number, $Re = UH/\nu$, B/H is the aspect ratio between wide flume (B) and depth water (H), H/D_g is the ratio of depth water and gravel diameter, S_f is the friction slope (bed slope), and $U = Q_{sur}/(BH)$, as Table 3.1 shows.

Table 3.1: Hydraulic parameters.

Q_{sur}	Q_{sub}	U	Fr	Re	H/B	H/D_g	S_f
l/s	l/s	m/s	–	–	–	–	–
0.088	0.008	0.044	0.054	2933	2.2	6.7	0.017

In experiment E1, the fine sediment in the channel was poured locally, at the beginning of the flume ($x = 0.05$ m), as a hyperconcentrated mixture of fine sediment with water. The dynamics of this mixture considers suspension, deposition, and percolation. After deposition,

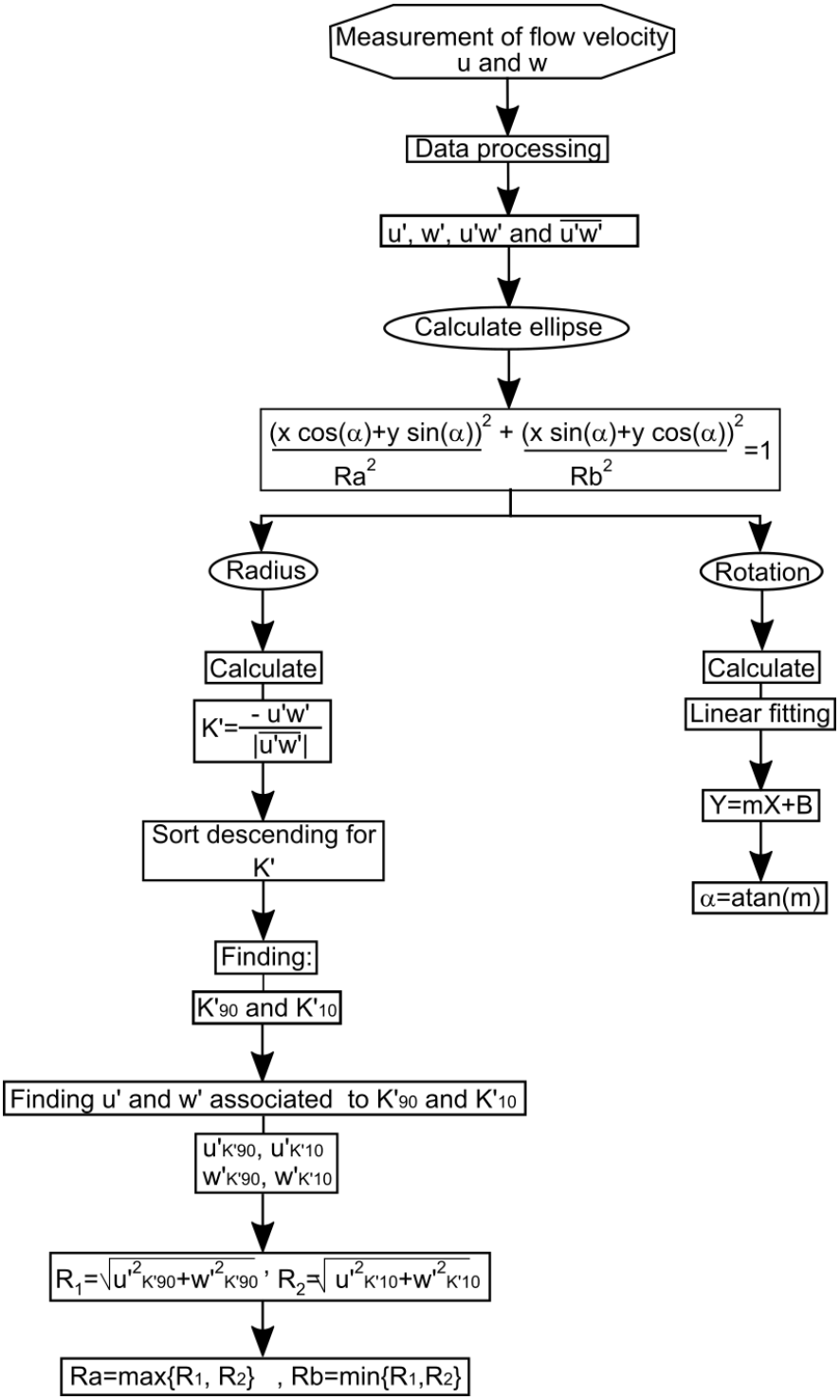

Figure 3.4: Methodology to characterize the scatter plot of velocity fluctuations through the ellipse parameters.

the fine sediment changes the permeability of the gravel bed. Thus, the interaction between surface and subsurface flow generates ejections of water from the bed to the water column. These jets eject subsurface water with fine sediment of low density deposited in the interstices of the gravel bed. The length of the jets has been approximately 15 mm, as shown in Figure 3.5a.

These sediment ejections generate a low entrainment of fine sediment into suspension transport or bedload transport, i.e., the sediment ejected is deposited in the neighborhood of the ejection, forming craters as bedforms (Figure 3.5c). Then, the experiment E1 is to characterize the ejection of the subsurface flow, which is modified by a lower permeability associated with the fine sediment and emerges to the surface current.

Figure 3.5 is localized in the tank at 20 cm downstream of the center part of the facility as shown in Figure 3.1. The velocity data are taken at the center of the cross section and at the point where the sediment ejections appear. Furthermore, the velocity fluctuations and wavelet analysis are analyzed at 1.5 cm up from the of pumicite level. The velocity profiles were analyzed considering spatially averaged open-channel flow proposed by Nikora et al. (2001)

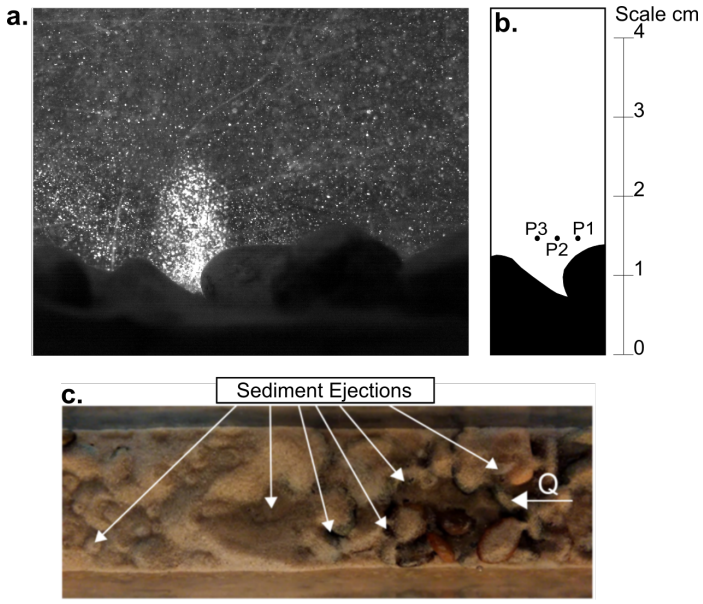

Figure 3.5: (**a**) sediment ejection for Q_{sur} = 0.088 l/s y Q_{sub} = 0.08 l/s; (**b**) measurement points; (**c**) top view of the sediment ejections.

3.3.1 Velocities and Shear Velocities

The velocity data were measured with PIV and processed with PIVLab. The spatial average mean velocity profile and the spatial average mean shear rate were obtained according to the double-averaged methodology proposed by Nikora et al. (2001). The spatial average mean velocity profile made dimensionless with the shear velocity for the experiments E0 and E1 are shown in Figure 3.6. Table 3.2 shows the shear velocities in both experiments, u_{*E0} and u_{*E1}. Shear velocities were calculated as $u_{*Ei} = \sqrt{\tau_{0Ei}/\rho}$, where τ_{0Ei} is the experimental

shear stress in the bed and i = 0, 1, for experiment E0 or E1, respectively. The experimental shear stress E_{0Ei} were estimated applying the methodology proposed Nikora et al. (2001). The dimensionless velocity profile for E1 is much more intense than for E0. This is because the shear velocity u_{*E0} is 39% higher than the shear velocity u_{*E1}. However, the ratio of the depth average mean velocities in E1 and E0, U_{E1}/U_{E0}, is 0.90. Therefore, the surface flow is faster in E0 than in E1 because the sediments ejection has a dominant vertical velocity. However, in an area without sediment ejection, the streamwise velocity in E1 has to be greater than E0 because there is outflow of the subsurface flow to the surface flow.

Table 3.2: Velocities and shear velocities.

U_{E0}	U_{E1}	u_{*E0}	u_{*E1}
m/s	m/s	m/s	m/s
0.058	0.052	0.0032	0.0023

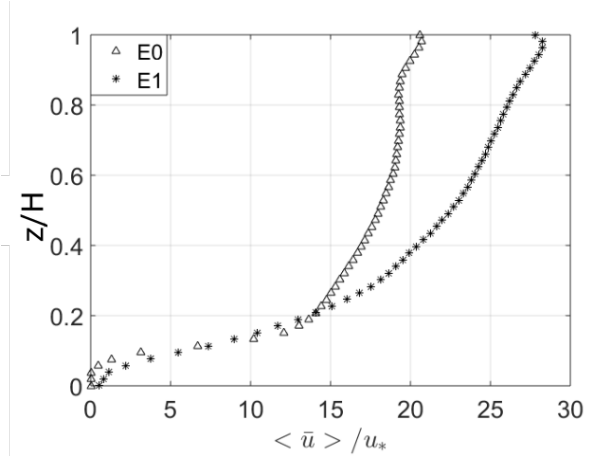

Figure 3.6: Velocity profiles double-averaged, for both experiments E0 and E1, before and after the spill of pumicite mixture, respectively.

In Figure 3.5b are the points that were analyzed for the turbulence interactions in one sediment ejection—that is, upstream of the center of ejection (P1), the center of ejection (P2) and downstream of the center of ejection (P3). Turbulence fluctuations were analyzed under three approaches: scatter plot of u' and w', velocity field, and wavelet analysis.

3.3.2 Velocity Field

Velocity vectors in the streamwise and vertical plane obtained through PVI processing are presented in Figure 3.7, for three different times, 40.00 s, 40.63 s, and 41.26 s. Figure 3.7 also presents the contour plot of the vertical velocity. The red polygon in that figure is limited where the vertical velocities are higher than the streamwise velocities in the ejection. Additionally, in Figure 3.7c, the blue lines show a coherent structure external to the movement we are observing, which is also a coherent structure from upstream. The vertical upward movement from the bed to the water column is associated with turbulent interactions of the

ejection type. However, the sediment ejections reported in this research are associated with jets with sediment, due to the interaction between surface and subsurface flow, and this is different from the turbulent interactions of the ejection type investigated for rigid wall, as reported by Niño, García (1996); Hofland (2005); Adrian (2007); Wren et al. (2011); Cooper et al. (2018) and others, who have analyzed turbulence interactions near the wall and have identified two main interactions as ejections and sweeps.

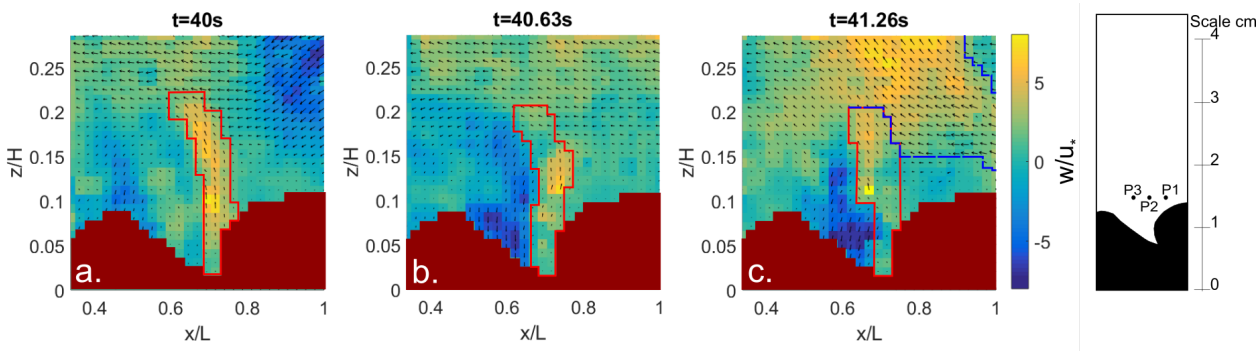

Figure 3.7: Velocity field for dimensionless vertical component (W / u_*) and vectors of streamwise velocity and vertical velocity, measured experimentally for E1, at **a.** $t = 40$ s, **b.** $t = 40.63$ s, **c.** $t = 41.26$ s. Measured field was $\Delta x = L = 2.9$ cm y $\Delta z = 3.5$ cm and flow depth $H = 6.7$ cm. Direction of the flow: from right to left.

In E1, the vertical velocities, w, made dimensionless with mean streamwise velocity, U, were analyzed before and after the spill of pumicite mixture as a function of dimensionless time tU/H. In this case, the vertical velocity time series at the water depth for the three positions into the sediment ejection, i.e., in each position, P1, P2, and P3, shown in Figure 3.5b, the velocities series were taken in the entire water column. However, for the case of E0, with no-spill of pumicite mixture, the vertical velocities are those associated only to P1 and P2. The vertical in P1 is a measure of the vertical velocity at a point on the gravel ridges (Figures 3.7 and 3.8a), while the vertical in P2 is a measure in the gravel pores (Figures 3.7 and 3.8b). The vertical velocities in $E0$, for $z/H > 0.1$ and in positions P1 and P2 follow Taylor's frozen turbulence hypothesis in the streamwise direction quite well (Figure 3.8a,b). Vertical velocities are higher for $z/H > 0.5 - 0.6$ than near the bed at P1 or P2 (Figure 3.8a,b). For position P2 near the bed, for $z/H < 0.1$, there is an area with high vertical velocity for $11 < tU/H < 61$ (Figure 3.8b) that is not detected for position P1. That is, the irregularities presented by the bed of gravel, with the ridges and low points, make Taylor's hypothesis of frozen turbulence invalid near the bottom.

Conversely, in E1, after the spill of pumicite mixture, it is found that the ejections generate streamwise changes in the vertical velocities. At P2, in the gravel pore, an ejection take place, with high positive vertical velocities, for $z/H < 0.2$ and $0 < tU/H < 80$ (Figure 3.9b). At P3, negative vertical velocities are predominant for $z/H < 0.2$. This behavior is associated with a current toward the bed (Figure 3.9c). At P1, vertical velocities are as the experiment E0 (Figure 3.9a). Thus, basically the image in time is as shown in Figure 3.7 in an instant, that is, the ejection is a quasi-steady feature of the flow.

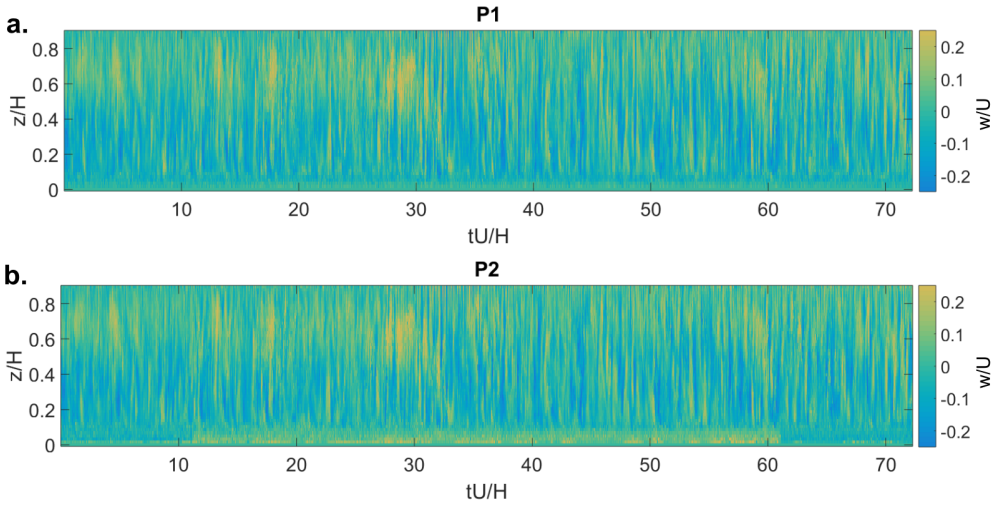

Figure 3.8: Vertical velocity made dimensionless with U, w/U in the experiment E0, with no-spill of pumicite mixture, for: (**a**) upstream of the center of the ejection, P1, (**b**) center of the ejection, P2.

3.3.3 Scatter Plot of Velocity Fluctuations

The turbulence interactions associated with fine sediment ejections (E1) were compared with turbulence interaction without fine sediment (E0). In addition, the experiments measured with PIV in this article (P1, P2 and P3) were compared with Acoustic Doppler Velocimetry (ADV) measurements of turbulent interactions for an open channel with a gravel bed Niño et al. (2018). Experimental setup for the acquisition of ADV data of Niño et al. (2018) was a flow rate of 14 l/s, a gravel bed of 45 mm particle diameter, a flow depth H of 0.1 m and $hm/H = 0.85$, where hm was the location of the ADV with respect to the bed. The distribution of the turbulence fluctuations (u', w') of an open channel in a Cartesian plane can be represented with an ellipse of negative slope and major axis (Ra) in the direction of quadrants 2 and 4 $(Q2 - Q4)$ and minor axis (Rb) in direction of quadrants 1 and 3 $(Q1 - Q3)$, as shown in Figure 3.10a,b, where the quadrants 1 to 4 are against clockwise circuit of the Cartesian plane and $Q1$ was $(u' > 0, w' < 0)$. According to Niño, Musalem (2000); Sambrook Smith, Nicholas (2005); Adrian (2007); Wallace (2016), the main turbulent coherent structures are ejections and sweeps, $Q2$ and $Q4$, respectively. The turbulent interactions in the narrow flume of this article have the same distribution as the widest flume of Niño et al. (2018), i.e., an ellipse with a negative slope and the main turbulent coherent structures are ejections and sweeps; however, the magnitude of fluctuations are greater for Niño et al. (2018), due to the turbulence is also greater, as shown Figure 3.10a,b. However, the pattern of those distributions change with respect to the turbulence in an open channel due to the presence of sediment ejections. These sediment ejections tend to increase the vertical fluctuations and decrease the streamwise fluctuations. These changes generate that outwards and inwards interactions can become events with a greater probability of occurrence than in a regular open channel, i.e., the ellipse has a positive slope and a relationship between Ra and Rb close to 1 (Figure 3.7c–e).

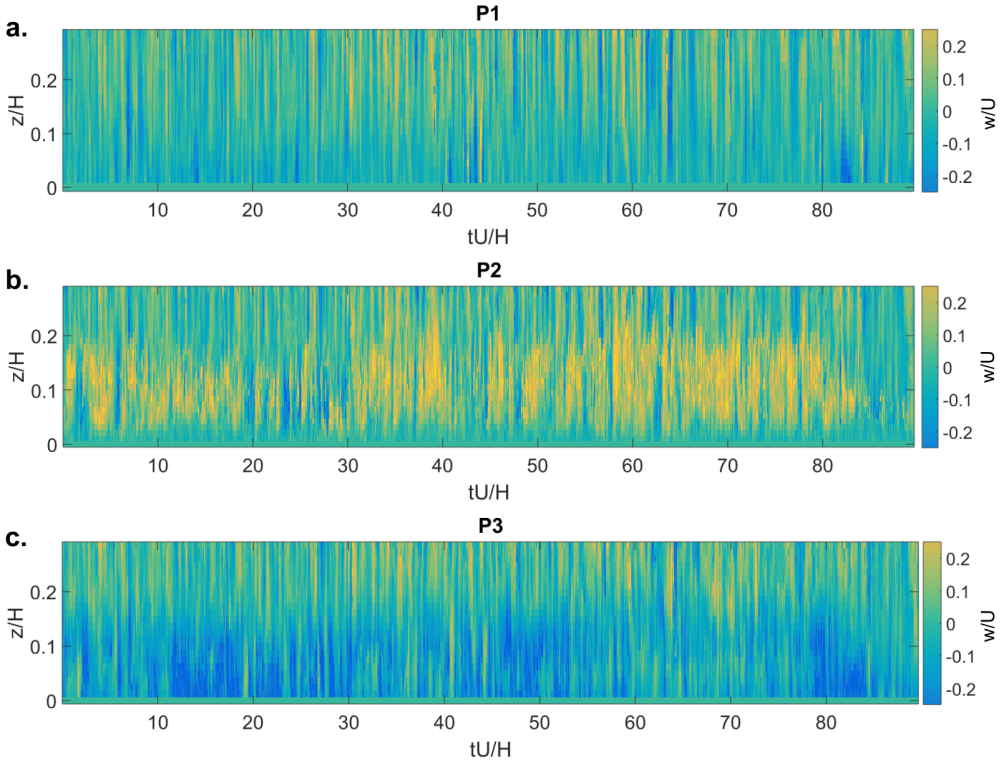

Figure 3.9: Vertical velocity made dimensionless with U, w/U in the experiment E1 after the spill of pumicite mixture for: (**a**) upstream of the center of the ejection, P1; (**b**) center of the ejection, P2 and (**c**) downstream from the center of the ejection, P3.

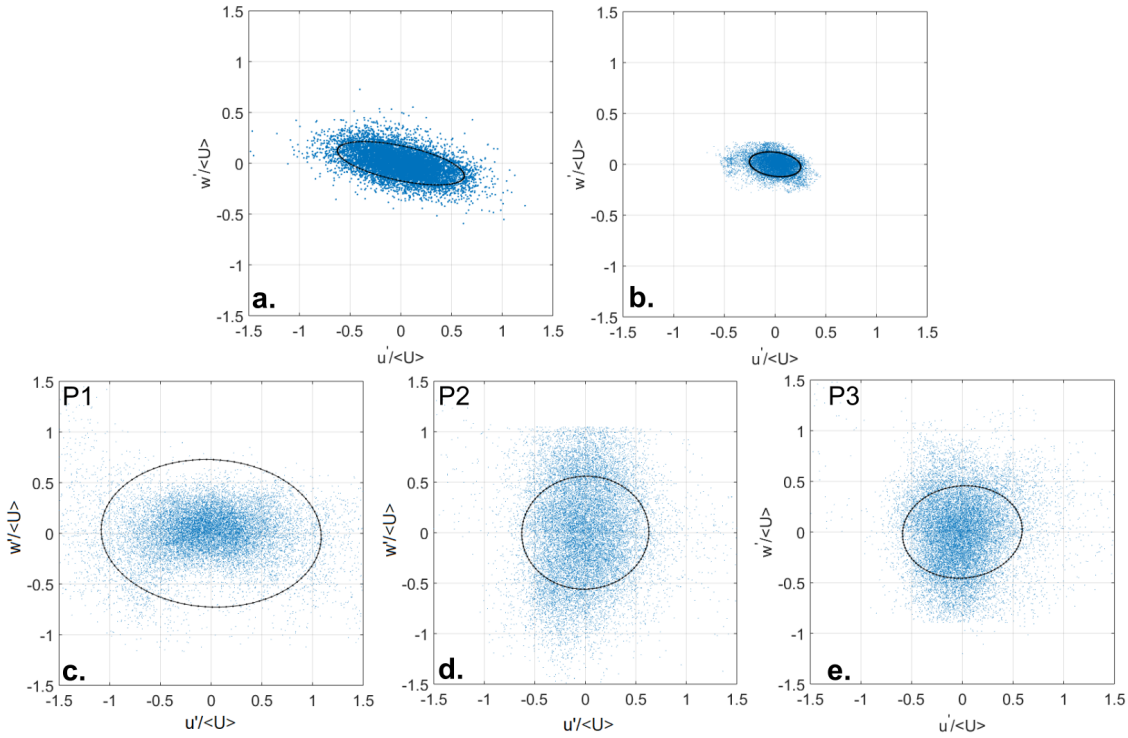

Figure 3.10: Scatter plot for: (**a**) ADV data Niño et al. (2018), (**b**) PIV data in experiment E0, (**c**) PIV data in experiment E1 after the spill of pumicite mixture for P1, (**d**) PIV data in experiment E1 after the spill of pumicite mixture for P2 and (**e**) PIV data in experiment E1 after the spill of pumicite mixture for P3.

3.3.4 Frequency Spectra and Wavelet Analysis

Power spectrum frequency for vertical and streamwise velocities fluctuation are calculated both for E0 and E1 in points P1, P2, and P3 (Figure 3.11). Power spectrum was made dimensionless with $u_*^2 H$. In both cases, it is possible to identify the production zone and the inertial sub-range in the power spectrum for both cases before and after the spill of pumicite mixture. The inertial sub-range was considered between wavenumber 10^2 and 10^3 (or its equivalent in frequencies is between 10^0 and 20–30 Hz), where the slope of $-5/3$ is representative. The frequency of more than 20–30 Hz is noise in the PIV velocities. In the case of E0, in the production zone and in the three points of measurement, the energy is higher for streamwise velocity fluctuations than vertical velocity fluctuations. Conversely, for E1 after the spill of pumicite mixture, the vertical velocity fluctuation has higher energy in the production zone than the streamwise velocity fluctuation because the sediment ejection in P2 has dominant vertical velocities (Figure 3.11e). Then, according to the dynamics of sediment ejection (E1), where the vertical fluctuation is dominant, it can be seen that, at P2, the energy in the production zone for this components is highest, at P1 the energy in the production zone is the same as the experiment E0, and at P3 the energy in the production zone for the vertical component is large with respect to the streamwise component and can be considered as a downwelling point.

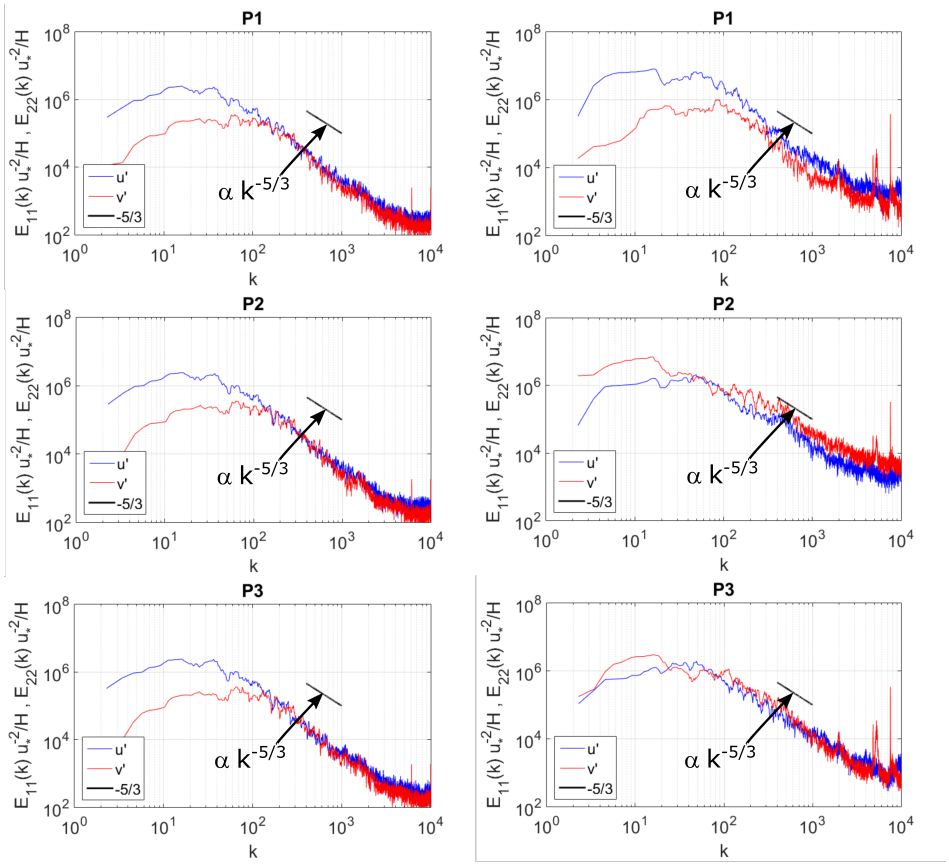

Figure 3.11: Power Spectrum Density for streamwise velocity fluctuation and vertical velocity fluctuations ($z/H = 0.1$), (**a**–**c**) in experiment E0, (**d**–**f**) in experiment E1, after the spill of fine sediment mixture.

Since the sediment ejection is a quasi-steady flow, then the local wavelet spectrum in the experiment E1, after the spill of fine sediment mixture, was implemented to analyze the u' and w' velocity components in the three points of the sediment ejection, P1, P2 and P3 (Figures 3.12 and 3.13). The wavelet spectra $|Wu|^2$ and $|Ww|^2$, corresponding to the wavelet spectra for u' and w' velocity fluctuations, respectively, were made dimensionless with dimensionless with Hu_*, as shown in Figures 3.12 and 3.13. The spectra have λ/H in vertical axes and tU/H in horizontal axes, where λ is the wavelength calculated as $\lambda = U/f$, f is frequency and tU/H is the dimensionless time. Wavelet analysis allows for seeing the variations of the power spectrum over time, i.e., with this analysis, a turbulent structure is determined and the time the structure is present in the measurement time. In the streamwise direction, upstream of sediment ejection, P1, the energy is concentrated for $\lambda = 10H$, for a long period of time, $10 < tU/H < 82$ (Figure 3.12). This wavelength is associated with a frequency of 0.06 Hz. According to the power spectrum shown in Figure 3.11e, it is a structure corresponding to a large-scale motion, i.e., this large-scale is present in almost all the time of the measurement time. In points P2 and P3, there is concentration of energy at this wavelength (frequency), but it is less intense than at P1, whereas, for $\lambda = 5H$ and $\lambda = 4H$, there is a concentration of energy at all the measurement points, P1 to P3. This wavelength is associated with frequencies of 0.13 Hz and 0.16 Hz, corresponding to large-scale motions (Figure 3.11d–f). However, this structure is present only at certain points in time; the period most frequent is $tU/H \sim 50$ (Figure 3.12a–c).

The wavelet spectrum for vertical fluctuation shows energy concentrations in P2 and P3 higher than those of P1; the highest concentration of energy is that of P2. This wavelet spectrum shows that, at point P2, during the entire measurement time, the vertical component of sediment ejection dominates, as shown in the spectrum of Figure 3.9b. According to the wavelet spectrum, Figure 3.13b, $\lambda = 10H$ has a high energy concentration for $10 < tU/H < 82$. That wavelength corresponds to the frequency 0.06 Hz and is associated with a large scale of motion for P2 and P3 (Figure 3.11b,c). In addition, for $\lambda = 5H$, $4H$, and $3H$, there is a concentration of energy at points P2 and P3. This wavelength is associated with frequencies of 0.13 Hz, 0.16 Hz, and 0.21 Hz, respectively, corresponding to large-scale motions (Figure 3.11d–f). However, these structures are present only at certain points in time, the period most frequent is $tU/H \sim 40$ (Figure 3.12a–c).

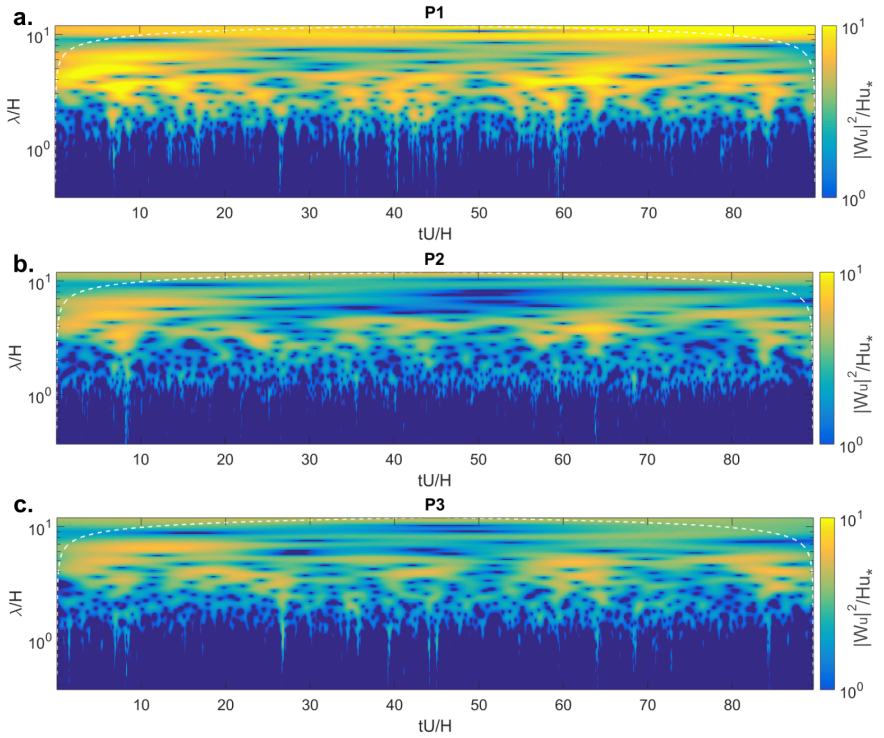

Figure 3.12: Wavelet spectrum for streamwise velocity fluctuations, u', in the experiment E1, after the spill of fine sediment mixture (**a**) P1, (**b**) P2, and (**c**) P3.

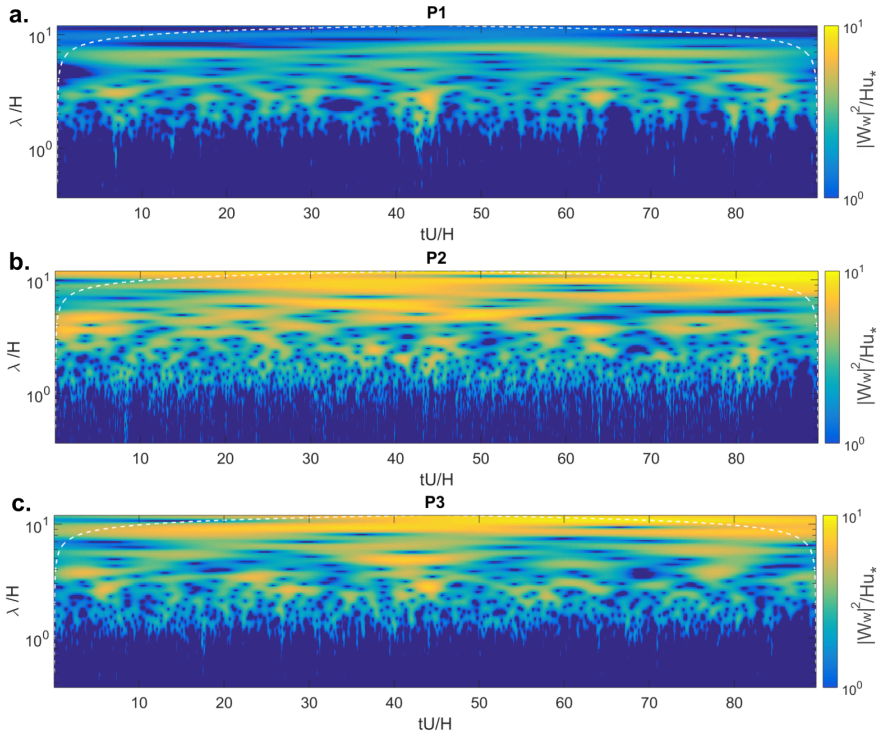

Figure 3.13: Wavelet spectrum for vertical velocity fluctuations, w', in the experiment E1, after the spill of fine sediment mixture, (**a**) P1, (**b**) P2, and (**c**) P3.

3.4 Discussion

The coherent structure in turbulence flows have been researched by Niño, Musalem (2000); Wallace (2016); Cooper et al. (2018); Hofland (2005); Lichtner (2015) in open channels with permeable and impermeable beds, considering a steady flow. One methodology has been to analyze the Reynolds shear stress in quadrants of the Cartesian plane, with u' and w' and their distribution is described as an ellipse of negative slope and a turbulent event has a high probability to be in the quadrant $Q2$ and $Q4$, while $Q1$ and $Q3$ have a low probability of occurrence. In this study, we can see the same distribution of Reynolds shear stress in the case of open channel without fine sediment deposited into the bed (E0). However, the interaction between surface and subsurface flow in E1, after the spill of pumicite mixture, causes the analysis to change. The sediment ejection generates a quasi-steady flow from the bed toward the water column, where the vertical velocity component is higher than the streamwise velocity component, i.e., the turbulent interactions in $Q1$ and $Q3$ for that structure has a higher probability than in other research.

Furthermore, for isotropic turbulence in smooth open channel flow, Taylor's frozen turbulence hypothesis has been validated by Cenedese et al. (1991); Chen et al. (2019); Zhong et al. (2015) and others. Taylor's frozen turbulence hypothesis is also validated in experiment, E0, for $z/H > 0.1$. However, Cameron et al. (2017) recognizes the limitations of applying the Taylor's hypothesis. They considered an uncertainty for $z/H < 0.1$ because, in this region, the mean velocity and local velocity can diverge. Then, in experiment E0, the velocity difference between P1 and P2 for $z/H < 0.1$ is associated with a divergence of gravel pore velocities, so that, near the permeable bed, the Taylor's frozen turbulence hypothesis is invalidated, and these results are according to Cameron et al. (2017).

In experiment E1, fine sediment ejections are quasi-steady flows from the bed. Turbulence patterns change and turbulence becomes anisotropic because sediment ejection has a dominant vertical velocity. In this case, Taylor's frozen turbulence hypothesis is also invalidated.

The power spectrum density in open channels has been reported by García et al. (2005); Chanson et al. (2007); Nikora et al. (2007); Balakumar, Adrian (2007). They have validated the $-5/3$ slope in the measured spectra and show a greater spectral density of the streamwise component than the spanwise and vertical components. However, in this study, for the experiment E0, in the production zone, there is a greater spectral density of the streamwise component than the vertical component, but in the inertial subrange both components have a spectral density of similar magnitude. Conversely, in experiment E1, since the sediment ejection has a dominant upward movement, the spectral density changes. Upstream of the sediment ejection, at P1, in the production zone, the spectral density for streamwise component is greater than the vertical fluctuation component and the spectrum densities in both components are greater than the spectral density in experiment E0, whereas, in the center of the ejection, at P2, in the production zone and in the inertial subrange, the spectral density for vertical fluctuation component is greater than the spectral density for streamwise components. Downstream of the ejection in experiment E1, P3 can be considered as a downwelling point. It is important to note that sediment ejection increases the spectral energy, both in the production zone and in the inertial subrange.

Coherent structures of turbulence in open channels have been characterized by their sizes, such as small-scale motion, large-scale motion, and very-large scale motion by (Zhong et al., 2015; Chen et al., 2019). Streamwise scales of $3H$ and $10H$ allow coherent structures in these experiments to be classified as large-scale, i.e., hairpin vortex, and very large-scale

motion, i.e., super streamwise vortex. Ref. Chen et al. (2019) implemented the wavelet analysis to detect high concentrations of energy over time and their scale of motion, finding high concentrations of energy in $\lambda = 3H$ and $\lambda = 10H$, i.e., they reported hairpin vortices and super stream vortices; however, they did not show the influence cone, so the presence of the super stream vortices is not clear. The large-scale motion and the very large-scale motions find in this research are not the same coherent structures reported by (Zhong et al., 2015; Chen et al., 2019) because the pattern of the sediment ejection has a dominant vertical component. In addition, the energy concentration changes with the measurement position inside the sediment ejection.

The interaction between ejections, sweeps, outward, and inward interactions generates turbulent structures such as horseshoe vortices, hairpin vortices, shedding vortices, etc. Those turbulent structures can move sediment away from where they occurred, i.e., they can generate erosion or scour (Dey, 2014). Interactions such as ejections and sweeps are more common in open channels; however, in the experiments presented in this article, this is not entirely true. Outward and inward interactions are more frequent than in open channels. Furthermore, pumicite is a fine cohesive material, so mechanisms such as particle rolling, sliding, and saltation were not observed in the present experiments. Therefore, no erosion or scour was observed due to the sediment expulsion. However, there is a constant interaction between the surface and subsurface flow. This dynamic is relevant considering that the fine material can be, for example, mining materials and, therefore, a constant exchange of toxic material can be generated from the hyporheic zone to the surface flow.

The experimental scale is small compared with natural environments, but the dimensionless parameters in the experiments presented in this article on the basis of the flow and sediment transport phenomena in mountain streams are believed to be correct. The dimensionless parameter $H/D_g = 6.7$ of the experiments is representative of macroroughness flow and there is no bedload transport, that is, $\tau_* = 0.00006 < \tau_{*c} = 0.035$, where τ_* is the dimensionless shear stress, $\tau_* = u_*^2/(gRD_g)$, and τ_{*c} is the critical shear stress for the incipient motion of the sediment, with $R = (\rho_s - \rho)/\rho$, ρ_s and ρ are the sediment and water density, respectively Niño et al. (2018). However, the dimensionless parameter that is essential for this article is u_e/w_s, where u_e is the entrainment velocity and w_s is the fall velocity of the fine sediment Niño et al. (2003). The dimensionless parameter $u_e/w_s > 1$ would make entrainment possible. The flow average vertical velocity $< w >$ in P2 is 0.007 m/s (Figure 3.9) and w_s of the pumicite is 0.005 m/s, so, if u_e is equal to $< w >$, $< w > /w_s > 1$ and there is entrainment of the pumicite to the surface flow. The value of w/U in P2 observed in Figure 3.9 is in the order of 0.15, which shows that a significant part of the subsurface flow appears in the surface flow.

3.5 Conclusions

Fine sediment, such as pumicite, between the pores of a gravel river bed, can reduce the permeability and the initial porosity of the bed, modifying the roughness and hydraulic parameters of the subsurface flow. Pumicite has a low density, generating changes in the interaction between the subsurface and surface flow. These interactions are mass, momentum, and energy exchange, so the decrease of permeability of the gravel layer can generate an increase of vertical velocity and the turbulence intensities in the surface layer. Additionally, low velocities in the streamwise direction and high vertical velocities can break the streamwise structures associated with secondary currents near the bed and sediment ejections can be

seen.

The sediment ejections change the patterns of turbulent structures and the distribution of the turbulence interactions, which means that the flow does not have a typical rough wall open channel flow turbulence. Additionally, the sediment ejections increase the energy both in the production zone and inertial subrange. Within the ejection, the vertical velocity component has the highest increase of energy in the center of the ejection. The sediment ejections could vary with the granular size of the subsurface layer and the density of the fine material, i.e., the low-density fine material in the subsurface layer encourages the presence of sediment ejections from the bed.

As future work, we will continue to evaluate the turbulent structures associated with sediment ejections in the presence of surface and subsurface flows. Fine sediments, with higher densities will be considered, for example, mining materials, such as tailings or metal concentrates, to evaluate the effect of particle density on the dynamics of the ejection. To characterize both spanwise and the sediment ejection in 3D, we will implement the technique Stereo PIV.

Chapter 4

Infiltration depth of mineral particles in gravel-bed rivers

This chapter is based in the paper published in Minerals journal (2021). Bustamante-Penagos N. y Niño Yarko. Doi: https://doi.org/10.3390/min11111285

abstract
This article discusses the results of an experimental study of a spill of mineral particles in gravel-bed rivers due to mining accidents. The purpose of this research is to characterize the dynamics of the fine mining particles spilled on a bed of immobilized gravel as a hyper-concentrated mixture and to experimentally characterize the infiltration phenomenon. We analyzed the type of infiltration considering the dimensionless coarse to fine particle size relationship, the dimensionless weight of the fine particles, the relative density of the particles, and the relationship between the subsurface and surface velocities, in addition to the densimetric Froude and Reynolds numbers of the fine particles. We found that the dimensionless infiltration depth is not associated with hydraulic parameters or the weight of the fine sediment spilled; however, fine sediment deposition decreases with depth, and infiltration depth may increase if subsurface flow decreases over time. Finally, a relationship of the dimensionless maximum infiltration depth with the relative density of the mining particles, the ratio of the bed sediment and the mining particles sizes, and the ratio between the subsurface and surface velocities is established.

4.1 Introduction

Heavy metals in riverbeds can come from acid rock drainage formation, mining, industry, or mining accidents. As a result of current and historical metal mining, rivers and floodplains in many parts of the world have become contaminated by the metal-rich waste in concentrations that may pose a hazard to human and animal livelihoods (Coulthard, Macklin, 2003; Macklin et al., 2006; Byrne et al., 2015). Human health and environmental impacts commonly arise due to the long residence time of heavy metals in river sediments and alluvial soils and their bioaccumulatory nature in plants and animals (Macklin et al., 2006).

Coulthard, Macklin (2003) modeled heavy metal contamination in river systems in the United Kingdom. Simulations considered sediment transport dynamics to analyze contaminant transport due to sediment movement. An increase in flow rate may reduce contamination because it could generate bedload transport, and further dilution may occur. Jaskuła et al. (2021) analyzed the spatial variability of riverbed pollution by heavy metals, such as Cr, Ni, Cu, Zn, Cd, and Pb, in sediments of the Warta riverbed in Poland. They found that the highest contributors to pollution were urbanized areas and industrial activities. They also reported the temporal variability of heavy metals and that the ecological risk is proportional to the presence of heavy metals in the riverbed.

Several mining accidents have occurred worldwide. Benito et al. (2001) studied the Aznalcollar mine spill in 1998. The accident caused the spilling of some 4.5×10^3 Mm^3 of acid water and pyrite ore, generating a waste sludge with a high concentration of heavy metals in the floodplains of the Agrio and Guadiamar rivers, Spain, affecting the Sierra Morena ecosystem. In 2014 the tailings dam failure at the Mount Polley Mine accidentally spilled 25 Mm^3 into the Quesnel River watershed, and the material was deposited within the riparian zone. However, metal concentrations were lower than in other mining accidents (Byrne et al., 2018). The collapse of the Fundão tailings dam, Brazil, in 2015, spilled more than 43 Mm^3 of iron ore tailings, polluting a length of approximately 668 km from the Doce River to the Atlantic Ocean. Part of the tailings affected the nature reserve in the Doce River (Carmo do et al., 2017). In Chile have occurred several mining accidents of pipe failure that have ended with copper concentrate or tailings into gravel rivers. CENMA (2008) reported sedimentary chemical analysis of the Aconcagua river, finding a negative effect associated with the presence of heavy metals along the river due to mining activity. The most critical situation occur during the fall. Soublette et al. (2011) confirmed sediments with the presence of contaminants, both gold and copper ore tailings on the Illapel river, Chile. These contaminants generated poor quality surface water, but there was no evidence of groundwater contamination.

The hyporheic zone allows exchange between the groundwater system and surface water in rivers and floodplains. This exchange takes place through sediment porosity and is characterized by the circulation of surface water into the alluvium and back to the riverbed (Tonina, Buffington, 2009). In highly permeable gravel beds, interstitial flow velocities can transport fine particles into the hyporheic zone, filling interstitial spaces (Mcdowell-Boyer et al., 1986; Findlay, 1995), so gravel porosity is a reservoir for interstitial deposition of fine sediment (Cui, Parker, 1998). Fine particles in gravel beds generate large changes in hyporheic exchanges. They have a high environmental impact as they have poor macroinvertebrate survival, poor nutrient cycling, low oxygenation of fish eggs, and anaerobic changes (Findlay, 1995; Beschta, Jackson, 1979; Diplas, Parker, 1985; Lisle, 1989; Shrivastava, 2020). Pollution in the hyporheic zone could also be clogged due to natural sediment, fluvial transport of particulate organic carbon (POC), bacterial mass growth (bioclogging), formation of gas bubbles in stream beds, precipitation of heavy metals or metal contaminants (Shrivastava, 2020; Fox, Asce, 2016; Coulthard, Macklin, 2003). However, when the fine particles come from mining, their effect is much worse because of its prolonged residence time, and it has human health and environmental impacts (Coulthard, Macklin, 2003; Macklin et al., 2006).

Sediment particles can be transported in suspension, bedload, or infiltration. Particles, such as gravel, or sand, can be transported as bedload. In contrast, particles such as fine sand, silt, or clay can be transported in suspension. However, when fine particles fall onto the bed, the infiltration phenomenon takes place. The presence of fine sediment infiltrated in gravel beds could change the roughness, velocity field, and shear stress (Sambrook Smith

et al., 1997; Sambrook Smith, Nicholas, 2005; Niño et al., 2018). Fine sand infiltration deposits in gravel beds could change their behavior as a gravel bed to behave as a sand bed (Sambrook Smith et al., 1997). Lisle (1989); Edroma (1974); Cui et al. (2008); Wooster et al. (2008); Bustamante-Penagos, Niño (2020b) reported a decrease in fine material infiltration with depth in the substrate. That behavior considered both natural sediment and copper concentrate in the case of mining accidents.

Several experimental investigations have studied the infiltration of fine materials phenomenon in gravel beds due to the pollution into the hyporheic zone with natural sediment (Cui, Parker, 1998; Beschta, Jackson, 1979; Diplas, Parker, 1985; Cui et al., 2008; Soublette et al., 2011; Iseya, Ikeda, 1987). Additionally, Gibson et al. (2009) considered glass particles, and Bustamante-Penagos, Niño (2020b) used copper concentrate as fine sediment. In those investigations, the unimpeded static percolation and bridging have been reported as infiltration types, so the accumulation of fine sediment does not have to occur by filling the pores of gravel-bed from the bottom up. According to Gibson et al. (2009), unimpeded static percolation is when fine sediment can move freely at depth because it is smaller than the pore of the substrate. Conversely, bridging is when the fine sediment is larger than the pores in the substrate.

Infiltration of fine sediment into the substrate could move as a wavefront when the substrate is gravel, and the fine sediment is fine sand, according to Niño et al. (2018), while Bustamante-Penagos, Niño (2020b) reported that the movement of copper concentrate into the substrate has a dominant vertical movement like fingers. Besides, investigations have shown that there is no evidence of a relationship between the hydraulic flow parameters and the infiltration depth of fine materials, i.e., the infiltration depth is independent of flow parameters of the surface flow. Thresholds to characterize the infiltration type, therefore, are geometric relationships of the particle sizes. The effect of subsurface flow on infiltration of fine materials has been studied by Huston, Fox (2015), but that study did not focus on infiltration depth.

The purpose of this study is to analyze, experimentally, the transport dynamics of fine mineral material in mining accidents in gravel beds. We have analyzed the infiltration of copper concentrate in a gravel bed in a flume study to evaluate the fate of a potential spill in a Chilean river (Bustamante-Penagos, Niño, 2020b). So, among the novel aspects in our present research are the effects of the relative density of the fine particles, the weight of the fine particles spill (copper concentrate and pumicite as a substitute of the clay part of tailings), and the surface and subsurface flow on the infiltration of fine materials phenomenon. Then, this research is the basis for a dimensionless analysis of the infiltration of fine material into substrate of natural gravel-rivers. The experimental study considered two facilities. This article presents a description of the dynamics of hyper-concentrated fine particle-water mixing in alluvial gravel channels. In addition, the infiltration of fine materials phenomenon is characterized by considering the size relationships of the sediments, the relative density of the mineral particles, and the effect of surface and subsurface flow.

4.2 Dimensional analysis

The purpose of this research is to identify the dynamics of mineral particles as they spill in gravel-bed alluvial channels due to mining accidents. The mineral particles are added to the flow through the free surface in the width mid-central point, with a concentration of particles in water. The spill has a given weight of mineral particles.

Bustamante-Penagos, Niño (2020b) presented a dimensional analysis on the infiltration depth of copper concentrate particles into gravel beds through Buckingham Theorem. However, in that article, neither the weight of the mineral particles, W_{spill}, the density of them, ρ_c (as they just considered copper concentrate), nor the subsurface velocity, U_{sub} (because it was not intended to vary it), were not considered because these were constant in all experiments. In this article, W_{spill} was added in the dimensional analysis, as well as ρ_c and U_s. Hence, the infiltration depth of fine sediment into gravel beds depends on the variables presented in equation (4.1). Note that, the equation (4.1) is ordered by geometric, (1), dynamic, (2) and kinematic parameters (3).

First, the geometric variables are presented, D_{ic}, D_{js} are the diameters of fine sediment and coarse grains, respectively, where i (or j) denote the percentage finer, and c and s denote fine particles or sand, respectively. The geometric standard deviations of the mineral particles and sediment are σ_{gs}, $\sigma_{gc} = \sqrt{D_{84c}/D_{16c}}$, the porosity is ϕ, and B and H are the width and depth of the flow, respectively. Second, the dynamic variables are shown, ρ, ρ_c, ρ_s are the densities of water, fine sediment, and coarse particles, respectively, the dynamic viscosity of water is μ, and the net weight of fine sediment that is spilled into the flume is W_{spill}. Third, the kinematic variables are presented, U_{sur} and U_{sub} are the surface and subsurface mean velocities, respectively, and g is the gravitational acceleration.

$$H_{perc} = f\,(\underbrace{D_{\mathrm{ic}}, D_{js}, \sigma_{gs}, \sigma_{gc}, \phi, B, H}_{1}, \underbrace{\rho, \rho_c, \rho_s, \mu, W_{spill}}_{2}, \underbrace{U_{sur}, U_{sub},\ g}_{3}) \tag{4.1}$$

Thus, the dimensionless parameters key in the infiltration depth of fine materials into gravel beds are presented in equation 4.2. First, there is the geometric relationship between diameters of fine particles and coarse sediment and the geometric standard deviation of the mineral particles. Second, there is the relationship between the average velocity of surface and subsurface flow and the dimensionless weight of fine particles feeding the system, $W^*_{spill} = W_{spill}/(\rho_s\, U^2_{sur}\, B\, H)$. Third, there are the hydraulic parameters such as particle Reynolds number, $\mathrm{Re}_s{=}U_{sur}\, D_{\mathrm{is}}\, \rho/\mu$, the dimensionless submerged density of fine mineral particles and sediment, $R_c = (\rho_c - \rho)/\rho$ and $R_s = (\rho_s - \rho)/\rho$, respectively, and densimetric Froude number squared, $Fr^2_{\mathrm{d}} = U^2_{sur}/(R_s\, D_{50s}\, g)$. The densimetric Froude number of sand was considered because fine mineral material begins transport mainly when there is sediment transport or bed scour.

Some parameters were discarded because they were in the same order of magnitude in all experiments. The standard deviation of the sand, σ_{gs}, was between 1.03 and 1.57, i.e., the grain size distribution of sands was similar. The substrate porosity, ϕ, and relationships between B, H, and D_{js} were discarded because the experimental conditions did not allow to have great changes in these parameters. In the same way, the dimensionless submerged weight of the sand, R_s, was discarded because the substrate density was the same in all experiments.

$$\frac{H_{perc}}{D_{ic}} = f\left(\underbrace{\frac{D_{js}}{D_{ic}}, \sigma_{gc},}_{1}, \underbrace{\frac{U_{sub}}{U_{sur}}, W^{*}_{spill},}_{2}, \underbrace{R_c, Re_s, Fr^2_d}_{3}\right) \tag{4.2}$$

However, (Beschta, Jackson, 1979; Gibson et al., 2009; Huston, Fox, 2015; Bustamante-Penagos, Niño, 2020b) reported that the infiltration depth of fine materials does not depend on the hydraulic parameters, so the infiltration depth is analyzed here considering the relationship between diameters of mineral particles, the grain standard deviations of the mineral particles, the subsurface and surface flows, and the dimensionless weight of fine particles feeding the system. We will show the infiltration depth of fine materials does not depend on the hydraulic parameters.

4.3 Materials and Methods

4.3.1 Facilities

In this article, 10 experiments were carried out in a flume with 0.05 m of sediment substrate, named F1, and 24 experiments were carried out in a flume with 0.39 m of sediment substrate, named F2. The experiments in F1 were conducted in the experimental setup used by Bustamante-Penagos, Niño (2020b). This setup consisted of an open channel 0.11 m wide, 3.0 m long, 0.15 m deep, and bed slope that varied between 0.007 and 0.047. The fine material was fed as punctual discharge through an acrylic cone, 2.83 cm in diameter. This system pours a flow rate of 0.23 l/s of copper concentrate for 7 s, and the net weight of fine sediment was $W_{spill} = 2.8$ kg (Figure 4.1a).
The experiments in F2 were conducted in the experimental setup used by Bustamante-Penagos, Niño (2020a). This setup consisted of an open channel, 0.03 m wide, 0.58 m long, and 0.63 m deep. The structure is divided into three sections. Upstream are the surface and subsurface input flows. At the center of the facility are the open channel, the bed, and the point where the fine material mixture is spilled. In the downstream area are the surface and subsurface output discharges. The fine material was fed through an acrylic cone in the free surface, of 1.0 cm of diameter, during 6 s. The net weight of fine material was between 0.070 kg - 0.284 kg for the experiments (Figure 4.1b). The flows in the experiments in both facilities are with fully developed turbulence. They have a relative depth, H/D_g, lower than 10, as observed in Table 4.1, i.e., they are macroroughness flows, such as mountain rivers.

4.3.2 Materials and instrumentation

An immobile bed of two layers of sediments, gravel and sands, was considered here, as did Bustamante-Penagos, Niño (2020a,b). The gravel layer represents the active layer in gravel-bed rivers Cui, Parker (1998) and also prevents the transport of sand. Furthermore, the flow rate is low because the objective of this research is to analyze the phenomenon of static infiltration of fine material. That is, there is no bedload of the bed material. In both experiments, the sediment setup for an immobile bed was considered, with two layers of sediment. Gravel as the first layer, because the mineral particles can move freely through

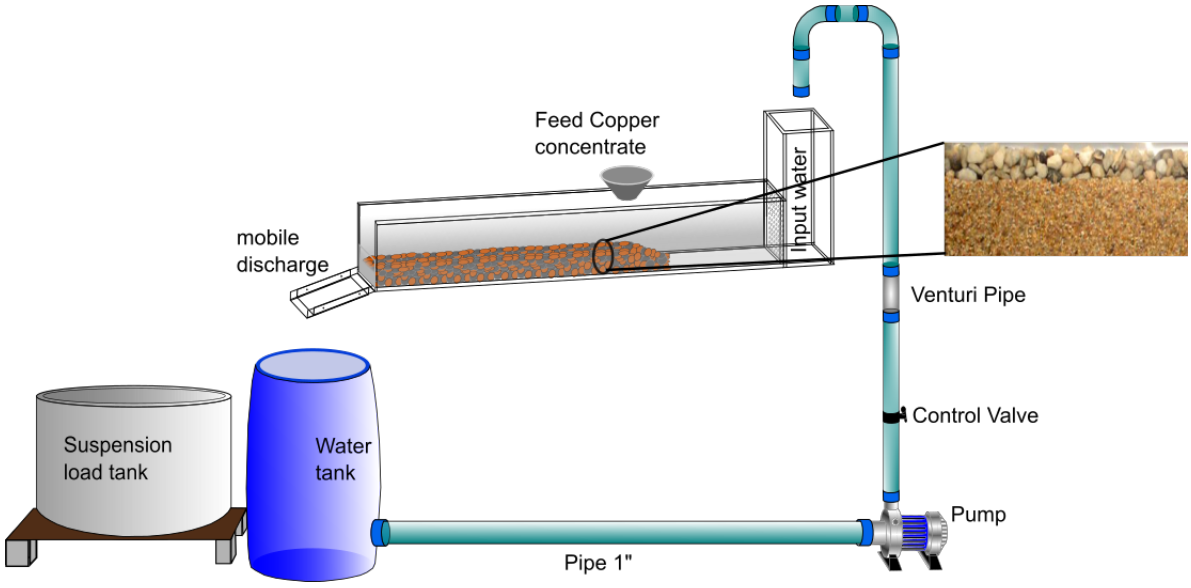

(a) The experimental setup used in Bustamante-Penagos, Niño (2020b)

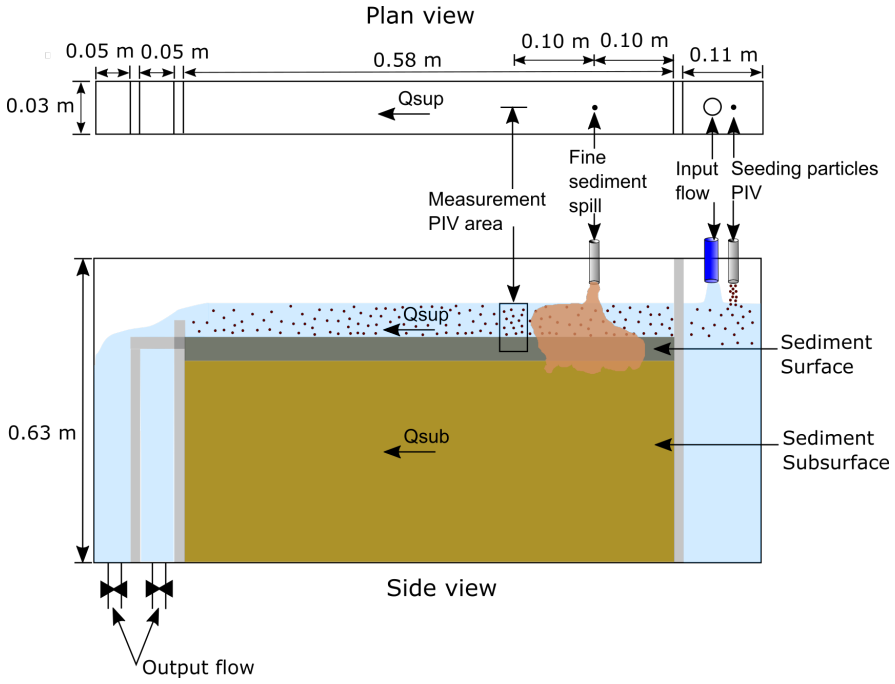

(b) The experimental setup used in Bustamante-Penagos, Niño (2020a).

Figure 4.1: **(a)** Flume with water recirculation and with the possibility of diverting the flow with a chute to a tank Bustamante-Penagos, Niño (2020b). The arrangement of the bed is with two layers of sediments. The surface layer is composed of gravel and the substrate layer of sand; **(b)** Experimental scheme used in the study of Bustamante-Penagos, Niño (2020a). The flume with 0.39 m of sediment thickness is used to measure high infiltrations of fine sediment and subsurface flow. The surface flow rate is Q_{sur} and subsurface flow rate is Q_{sub}.

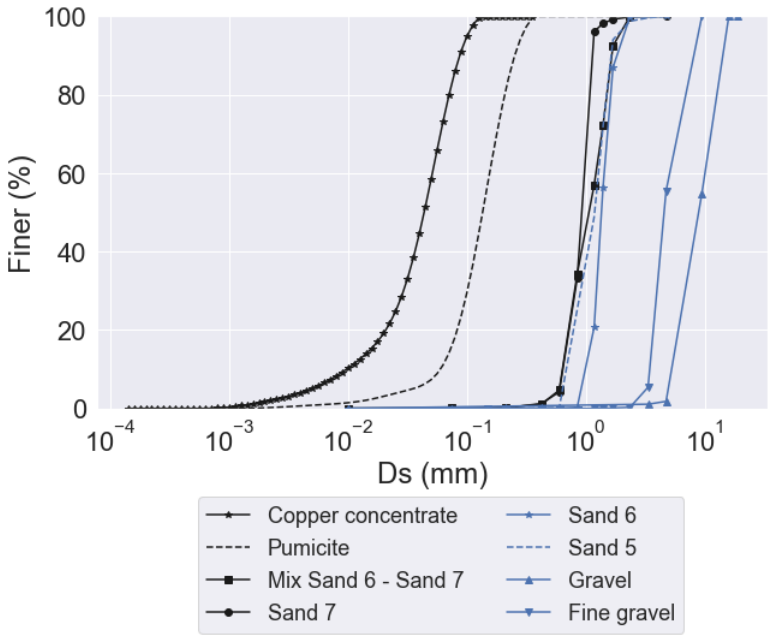

Figure 4.2: Grain size distribution of sediment and mineral particles.

the interstitial spaces of the gravel (i.e., through an internal particle suspension, so there would always be unimpeded static percolation), and to analyze the bridging infiltration, a sublayer of sand was considered. The thickness of the gravel layer represents the active layer in natural rivers (Parker, Klingeman, 1982).

The surface layer was gravel, with 20 mm thickness, and has a mean diameter of $D_g =$ 10 mm, both in the F1 and F2 flumes. In the F1 flume, the subsurface layer was of sand or fine gravel. It has 30 mm thickness and has a mean diameter, D_s, variable between 0.2 and 3.35 mm in different experiments. In the F2 flume, the subsurface layer was sand or fine gravel. It has 390 mm thickness and mean diameters between 0.7 and 5.7 mm, for different runs (Figure 4.2). The density of both materials, gravel, and sand, was 2.65 g/cm^{3}and the porosity of the substrate is 0.4 $\pm$0.02 in the experiments.

The fine sediments are copper concentrate, pumicite, and copper tailings. Only one experiment was made with actual copper tailings, but the pumicite recreates the clay-silt-sand content of tailings. The copper concentrate has a median diameter (D_{50}) of D_c=0.05 mm, a density of 4.2 g/cm^3 and it is poured with a concentration of 56% by volume in water; the pumicite has a median diameter (D_{50}) of D_c = 0.12 mm, a density of 1.7 g/cm^3 and it is poured with a concentration of 77% by volume in water. Copper tailings have a median diameter (D_{50}) of D_c= 0.34 mm, a density of 1.5 g/cm^3 and it is poured with a concentration of 56% by volume in water. Figure 4.2 reports the grain size distribution curves of gravel, fine gravel, three classes of sand (5, 6, or 7), copper concentrate, and pumicite. For each material, a different volumetric concentration was considered to avoid encapsulation, i.e., that it would only wet the particles.

The instrumentation used were a Venturi pipe for flow measurement, a Nikon D3200 camera for image analysis of fine sediment transport. The grain size distribution analysis of the fine particles is carried out in the Sedimentology Laboratory of the Universidad de Chile with Malvern Mastersizer 2000 equipment.

The experiments considered in this study are 34, 10 in F1, 24 in F2. Table 4.1 summarizes

the mean diameters, D_{50c}, D_{50s}, and grain standard deviations, σ_{gs}, σ_{gc}, of the fine sediment and sands, hydraulic flow parameters; Q_{sur}, Q_{sub}, U_{sur}, U_{sub}, surface and subsurface flows and section mean velocities and H flow depth, A, wetted area; R_h, hydraulic radius, S, slope of the channel, $u_{th*} = \sqrt{gSR_h}$, theoretical bulk shear velocity, R_c, dimensionless submerged density of fine sediment, $Fr_{\mathrm{d}}^2 = U_{sur}^2/(R_s\, g\, D_{50s})$, densimetric Froude number squared of the bed particle and $R\mathrm{e}_s = U_{sur}\, D_{50s}/\nu$, $R\mathrm{e}_g = U_{sur}\, D_{50g}/\nu$, bed particle Reynolds number and gavel Reynolds number, respectively, with ν the kinematic viscosity.
On the other hand, each experimental data has an error associated with instrumental precision. The flow rate in F1 was measured through mass measurement with an accuracy scale of 0.1 kg and an accuracy of the Venturi pipe of 0.2 l/s , while the flow rate in F2 was measured through volumetric measurement with a 500 ml test tube and the accuracy was of 1 ml. For the geometrical parameters, flow depth, wetted area, and the infiltration depth of the copper concentrate, the error was by the pixel size, in this case it was 0.3 mm, whereas the error for infiltration depth of pumicite and tailings was 1 mm.

Table 4.1: Sediment, mineral particles, and hydraulic parameters of flume, F1, and sediment column experiments, F2.

Exp	D_{50s}	D_{50c}	σ_{gs}	σ_{gc}	R_c	Q_{sur}	Q_{sub}	**H**	H/D_g	**A**	U_{sur}	U_{sub}	R_h	**S**	u_{*th}	Fr_{d}^2	$R\mathrm{e}_g$
#	m	m	-	-	-	l/s	l/s	m	-	m^2	m/s	m/s	m	-	m/s	-	-
1-F1	0.00100	0.000040	1.34	2.22	3.2	0.61	0.000	0.030	2.0	0.003	0.185	0.000	0.019	0.047	0.890	1.31	1848
2-F1	0.00100	0.000040	1.34	2.22	3.2	0.61	0.000	0.030	2.0	0.003	0.185	0.000	0.019	0.047	0.900	1.31	1848
3-F1	0.00100	0.000040	1.34	2.22	3.2	0.61	0.000	0.030	2.0	0.003	0.185	0.000	0.019	0.047	0.890	1.31	1848
4-F1	0.00004	0.001360	1.23	2.25	3.2	1.95	0.000	0.030	2.0	0.003	0.591	0.000	0.019	0.047	0.089	13.43	5909
5-F1	0.00004	0.002120	1.44	2.13	3.2	1.95	0.000	0.043	2.9	0.005	0.412	0.000	0.024	0.047	0.103	6.54	4123
6-F1	0.00006	0.000940	1.26	1.85	3.2	1.82	0.000	0.057	3.8	0.006	0.290	0.000	0.028	0.003	0.043	3.24	2903
7-F1	0.00004	0.001360	1.23	2.52	3.2	1.82	0.18	0.057	3.8	0.006	0.290	0.05	0.028	0.003	0.043	3.24	2903
8-F1	0.00006	0.000940	1.26	2.01	3.2	2.45	0.24	0.067	4.5	0.007	0.332	0.073	0.030	0.003	0.044	4.25	3324
9-F1	0.00006	0.000940	1.26	2.87	3.2	2.30	0.23	0.063	4.2	0.007	0.332	0.070	0.029	0.003	0.044	4.24	3319
10-F1	0.00006	0.001360	1.23	2.12	3.2	2.50	0.25	0.053	3.5	0.006	0.429	0.076	0.027	0.036	0.064	7.07	4288
1-F2	0.00003	0.001290	1.38	3.04	3.2	0.00	0.00	0.019	1.3	0.001	0.000	0.000	0.008	0.000	0.000	0.00	0
2-F2	0.00006	0.001970	1.22	2.22	3.2	0.06	0.004	0.010	0.7	0.000	0.203	0.000	0.006	0.029	0.041	1.59	2033
3-F2	0.00005	0.001910	1.25	2.67	3.2	0.03	0.013	0.028	1.9	0.001	0.036	0.001	0.010	0.002	0.013	0.05	357
4-F2	0.00004	0.001870	1.24	2.20	3.2	0.07	0.006	0.033	2.2	0.001	0.067	0.001	0.010	0.004	0.019	0.17	667
5-F2	0.00005	0.001910	1.23	2.46	3.2	0.05	0.006	0.033	2.2	0.001	0.054	0.001	0.010	0.007	0.027	0.11	535
6-F2	0.00005	0.004430	1.25	2.35	3.2	0.10	0.004	0.026	1.7	0.001	0.132	0.000	0.010	0.005	0.022	0.67	1321
7-F2	0.00005	0.001970	1.22	2.31	3.2	0.06	0.046	0.031	2.1	0.001	0.061	0.004	0.010	0.007	0.027	0.15	613
8-F2	0.00005	0.001980	1.22	1.97	3.2	0.11	0.026	0.026	1.7	0.001	0.138	0.002	0.010	0.015	0.038	0.74	1385
9-F2	0.00004	0.001230	1.38	2.31	3.2	0.08	0.034	0.067	4.5	0.002	0.039	0.003	0.012	0.007	0.029	0.06	388
10-F2	0.00460	0.000044	1.46	1.79	3.2	0.11	0.035	0.057	3.8	0.002	0.064	0.003	0.012	0.017	0.045	0.16	388
11-F2	0.00004	0.004490	1.45	2.41	3.2	0.02	0.04	0.031	2.1	0.001	0.022	0.003	0.010	0.002	0.013	0.02	215
12-F2	0.00004	0.001760	1.03	2.57	3.2	0.13	0.053	0.056	3.7	0.002	0.077	0.005	0.012	0.003	0.020	0.23	774
13-F2	0.00006	0.001910	1.23	2.86	3.2	0.15	0.038	0.056	3.7	0.002	0.089	0.003	0.012	0.005	0.025	0.31	893
14-F2	0.00017	0.005700	1.49	1.63	3.2	0.16	0.033	0.049	3.3	0.001	0.109	0.003	0.011	0.002	0.014	0.46	1088
15-F2	0.00019	0.004640	1.46	1.51	0.7	0.08	0.004	0.050	3.3	0.002	0.051	0.000	0.012	0.004	0.020	0.10	507
16-F2	0.00012	0.005150	1.51	1.74	0.7	0.15	0.003	0.061	4.1	0.002	0.081	0.000	0.012	0.005	0.025	0.26	814
17-F2	0.00014	0.004840	1.47	1.73	0.7	0.06	0.043	0.048	3.2	0.001	0.042	0.004	0.011	0.002	0.014	0.07	424
18-F2	0.00012	0.002940	1.33	2.09	0.7	0.09	0.039	0.059	3.9	0.002	0.052	0.003	0.012	0.010	0.035	0.104	520
19-F2	0.00023	0.002830	1.55	1.76	0.5	0.12	0.036	0.058	3.9	0.002	0.069	0.003	0.012	0.010	0.035	0.18	690
20-F2	0.00015	0.002420	1.38	1.79	0.7	0.20	0.055	0.071	4.7	0.002	0.094	0.005	0.012	0.022	0.052	0.34	939
21-F2	0.00012	0.001950	1.24	1.98	0.7	0.11	0.005	0.070	4.7	0.002	0.052	0.000	0.012	0.014	0.041	0.11	524
22-F2	-	0.002800	1.20	-	0.7	0.14	0.033	0.055	3.7	0.002	0.085	0.003	0.012	0.022	0.051	0.28	848
23-F2	-	0.002720	1.28	-	0.7	0.15	0.038	0.066	4.4	0.002	0.076	0.003	0.012	0.023	0.052	0.22	758
24-F2	-	0.002590	1.37	-	0.7	0.09	0.08	0.067	4.5	0.002	0.044	0.001	0.012	0.017	0.045	0.07	438

4.4 Results

4.4.1 Visualization of infiltration of fine mineral particles

The transport dynamic of fine mineral particles, when poured as a hyper-concentrate mixture, begins with transport in suspension because the mixture enters the flow through the free surface. When the fine sediment is mixed throughout the water column, infiltration of fine material begins, first at the gravel layer and, later, into the substrate layer (sand or fine gravel). Figure 4.3 shows four characteristic instants of the dynamic of the fine sediment (experiment 7-F1, Table 4.1) in the water column and bed. In experimental setup F1, Figure 4.3a shows the suspended transport of the hyper-concentrated mixture of fine sediment, after mixing it in the water column. In Figure 4.3b, the white arrows show the infiltration of copper concentrate as it begins to move into the gravel layer. After that, infiltration of copper concentrate into the sand (or fine gravel) substrate is generated. Figure 4.3c shows that the infiltration of copper concentrate patterns look like fingers. Therein, the white arrows show the beginning of infiltration of copper concentrate into the sand substrate. Finally, the final state of unimpeded static percolation within the sand substrate is shown in Figure 4.3d. Finger patterns have been fully developed. In addition, the green box shows the largest zone of fine sediment accumulation. The accumulation zone is generated due to the vertical variation of pore size because there is a change from gravel to sand, and the pore size of the gravel is larger than the pore size of the sand.

The infiltration of fine material analysis is also evaluated in experimental setup F2. In this case, the substrate height is 7.8 times larger than the substrate height size considered in F1. The maximum infiltration of fine material evaluated in F1 was for experiments with 30 mm sediment thickness and $d_s = 1.9$ mm. So it is also evaluated in F2. However, bridging layer was found at greater depth than 30 mm and with an inclination associated with the subsurface flow. Figure 4.4 shows images of the experiment 5-F2. Figure 4.4a shows, with red arrows, the fingers patterns of the copper concentrate deposits and their inclination due to subsurface flow. When copper concentrate deposits reach a maximum, there is no movement in the substrate (Figure 4.4a). Nevertheless, when the input flow is cut off, like an ephemeral stream, the decrease in the surface water level increases the infiltration depth of fine sediment (Figure 4.4b), because, vertical variation of subsurface flow can destabilize the bridging. The increase of the infiltration depth of the copper concentrate was analyzed by image processing. This analysis considers the image in which the infiltration depth of copper concentrate reaches the steady-state (Figure 4.4a) and the image when the water level is minimum. So, Figure 4.4c is the result of subtracting Figure 4.4b of Figure 4.4a. Note that the dark blue tones in Figure 4.4c show the increase in infiltration to the maximum infiltration state of copper concentrate.

Sediment size greater than $D_s = 1.9$ mm (fine gravel) was also considered in F2 to analyze the types of infiltration of fine materials. Both types of infiltration of fine materials, bridging, and unimpeded static percolation, were found. Figure 4.5 shows the bridging and unimpeded static percolation in F2. The color bar represents the concentration of copper concentrate in the sediment substrate sand (Figure 4.5a) and fine gravel (Figure 4.5b). The negative values in the color bar are because the intensities in an image are between 0-255. The zero intensity is associated with dark shades, while the 225 intensity is associated with light tones; i.e., when the infiltration of fine material increases its depth, the intensities decrease, so subtracting a final state from an initial state generates negative values when the analysis is performed

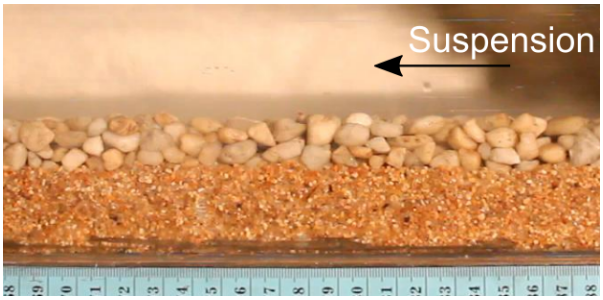

(a) t= 0 s

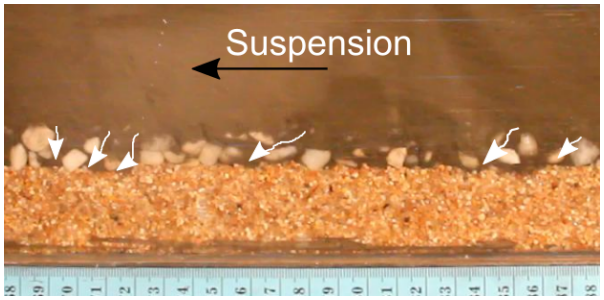

(b) t= 2 s

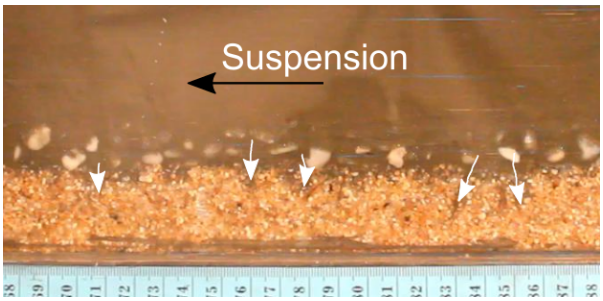

(c) t= 4 s

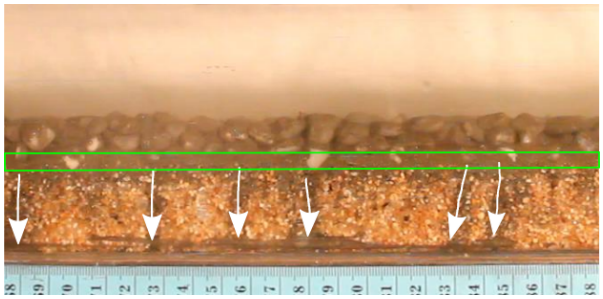

(d) Final state with unimpeded static percolation and bridging.

Figure 4.3: Copper concentrate transport dynamics in F1, experiment 7-F1; images were taken from the sidewall. **(a)** Suspension transport of copper concentrate; **(b)** White arrows show that copper concentrate begins to infiltrate the gravel layer; **(c)** White arrows show that the copper concentrate begins to infiltrate into the sand substrate; **(d)** The green box shows the maximum zone of copper concentrate deposition and white arrows represent unimpeded static percolation.

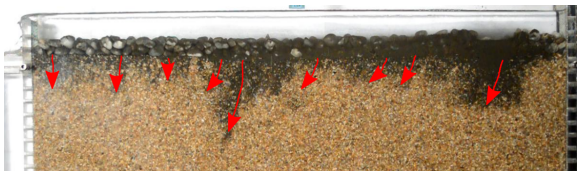

(a) Infiltration of copper concentrate into the sediment substrate.

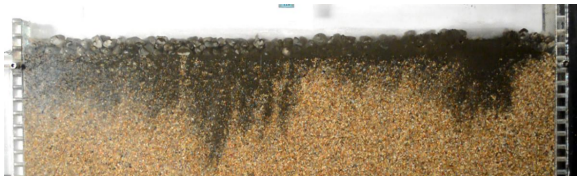

(b) Increase of infiltration depth due to decrease of subsurface level water.

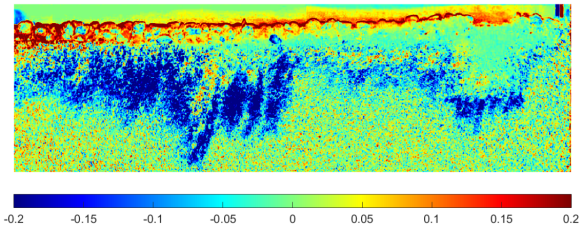

(c) Increase of infiltration depth considered the infiltration steady state with (Figure 4.4a) and without (Figure 4.4b) flows.

Figure 4.4: Effect of subsurface flow on increased infiltration of copper concentrate into sediment substrate. **(a)** Bridging steady state in the sand substrate, with d_s = 1.9 mm and Q_{sub} /Q_{sur} > 0; **(b)** Bridging steady state in the sand substrate with d_s = 1.9 mm and without surface and subsurface flows; **(c)** Increase in infiltration depth of copper concentrate due to decrease in surface water level because Q_{sur} decreases, Q_{sur} =0.

with double format images. The dark blue shades are the deposition of copper concentrate, while red shades are the changes associated with a small reflection of acrylic and water. The dashed black lines in Figure 4.5b show the zone of copper concentrate infiltration into the substrate of fine gravel substrate. When the substrate is fine gravel, the copper concentrate deposition concentration is lower than when the substrate is sand because the substrate with large particles, gravel or cobbles, generates a larger storage area of fine material. Therefore, the fine particles can be redistributed over a larger area, and for this reason, the concentration of fine particles within the substrate decreases.

4.4.2 Hydraulic Parameters

Infiltration depth of fine material was analyzed according to the dimensionless parameters presented in section 4.2. The H/D_{50g} parameter was omitted because macro-roughness flows were present in both experimental setups. H/D_{50g} was between 1.9 and 7.1, i.e., macro-roughness flows typical of mountains rivers, e.g., Aconcagua and Blanco rivers in Chile according to (Niño, 2002; CENMA, 2008).
On the other side, the infiltration dimensionless depth and type and the hydraulic parameters such as Frd^2 and Re_g were analyzed considering the parameters U_{sub}/U_{sur}, R_c, W^*_{spill}. Figure 4.6a-b allows analyzing the relationship between infiltration dimensionless depth and type and Frd^2 or Re_g, using R_c, and U_{sub}/U_{sur} as secondary parameters. Figure 4.6c-d allows analyzing the same relationship but using R_c, and W_{spill*} as secondary parameters. However, we did not find a relationship between the infiltration dimensionless depth and type and Frd^2 or Re_g, i.e., pollution into the bed is independent of hydraulic parameters, as (Beschta,

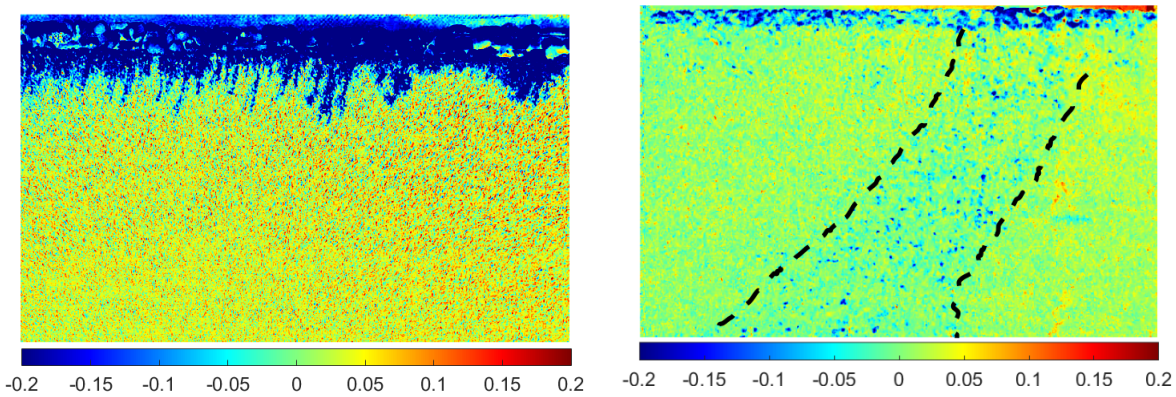

(a) Fingers pattern and bridging.

(b) Unimpeded static percolation.

Figure 4.5: Infiltration patterns of fine material and type of infiltration for two different substrates. **(a)** Substrate sediment is sand D_s= 1.9 mm, Q_{sur} = 0.053 l/s and Q_{sub} = 0.006 l/s; **(b)** Substrate sediment is fine gravel D_{50s}= 4.5 mm, Q_{sur} = 0.02 l/s and Q_{sub} = 0.04 l/s.

Jackson, 1979; Bustamante-Penagos, Niño, 2020b; Gibson et al., 2009; Huston, Fox, 2015) reported.

4.4.3 Infiltration depth of fine mineral particles

The infiltration depth for copper concentrate, pumicite, and tailings was analyzed considering hydraulic parameters do not effect infiltration depth, according to the analysis presented in section 4.4.2. The geometric relationships considered were D_{50s}/D_{50c}, D_{84s}/D_{16c} and D_{90s}/D_{50c}. These relationships were considered by Bustamante-Penagos, Niño (2020b) as good candidates to characterize the maximum infiltration type of copper concentrate in gravel beds. Figure 4.7 shows the thresholds corresponding to red lines proposed by Bustamante-Penagos, Niño (2020b) characterizing bridging or unimpeded static percolation. The colors represent each of the fine particles and the marker shows the infiltration type. Therefore, we can see that none of the thresholds, $D_{84s}/D_{16c} > 115$ and $D_{90s}/D_{50c} > 47$, adequately characterize the infiltration type. The infiltration reported as unimpeded static percolation in F1 was seen as a bridging layer in F2. For this reason, we propose that the concept of unimpeded static percolation is relative to the depth of the substrate, and this concept should be reevaluated to characterize the type of infiltration of fine materials. Unimpeded static percolation could become a bridging in a thicker substrate. We were able to find that the unimpeded static percolation reported by Bustamante-Penagos, Niño (2020b) became bridging in a thicker substrate. Under this argument, we postulate that the type of infiltration of fine material is relative to the depth of the substrate and the change in soil properties at depth. On the other hand, the dimensionless ratio of the maximum infiltration depth was analyzed by considering both U_{sub}/U_{sur}, and D_{50s}/D_{50c} (Figure 4.8a). R_c is represented by the color of the experimental points, and $W_{spill}*$ is represented by the size of the experimental points. Whereas Figure 4.8b considers the dimensionless ratio of the maximum infiltration depth as a function of R_c, and D_{50s}/D_{50c}. In this case, the color of the experimental points represents U_{sub}/U_{sur}, and the size of the experimental points represents $W_{spill}*$. Figure 4.8 shows that H_{perc}/D_{50c} increase with D_{50s}/D_{50c}, and is independent of $W_{spill}*$. The independence

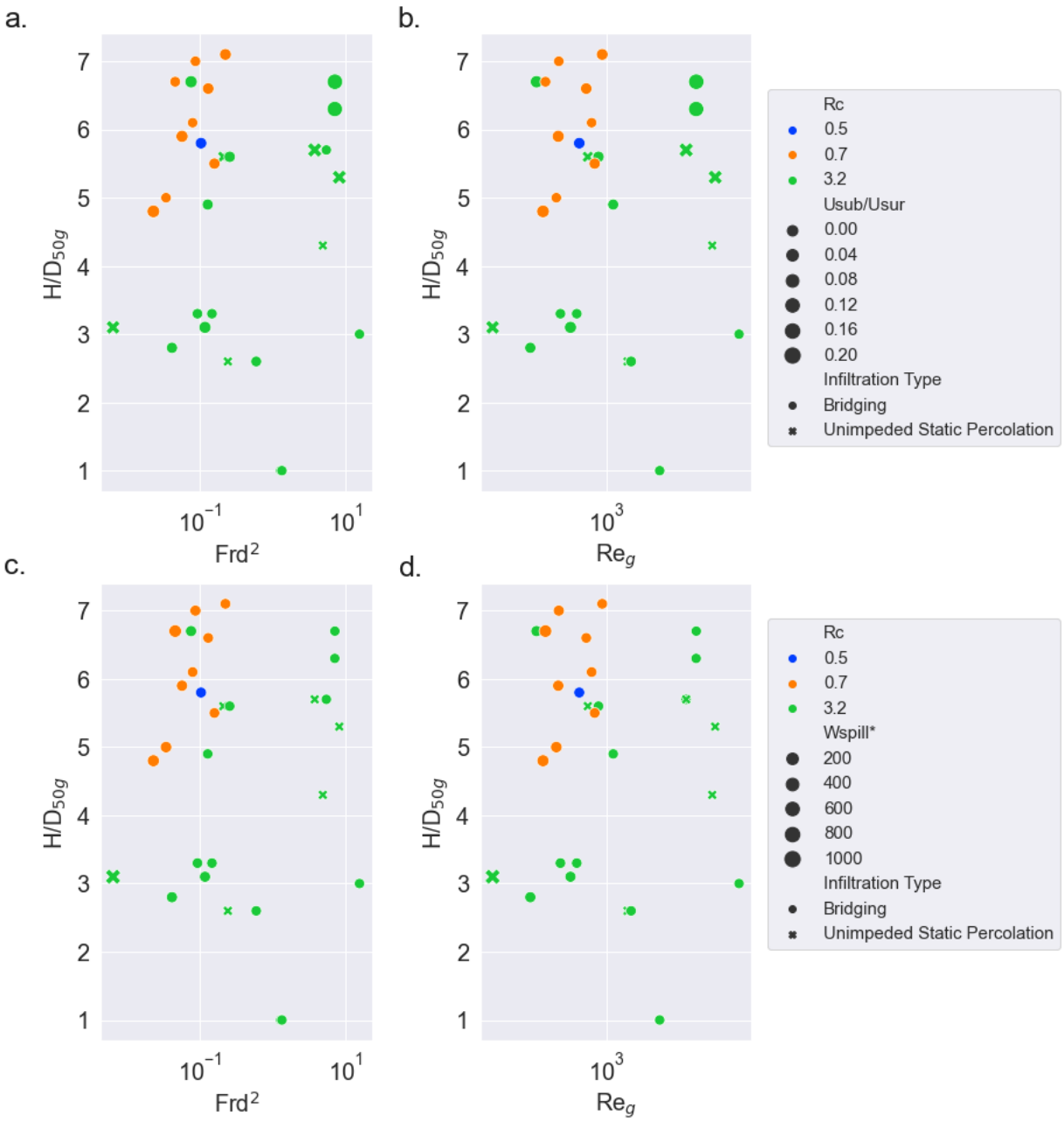

Figure 4.6: Infiltration dimensionless depth of fine material and type of fine particles into the substrate as a function of R_c, W_{spill*} and **a.- c**. densimetric Froude number squared of the particles, **b.-d.** Particle Reynolds number of the gravel.

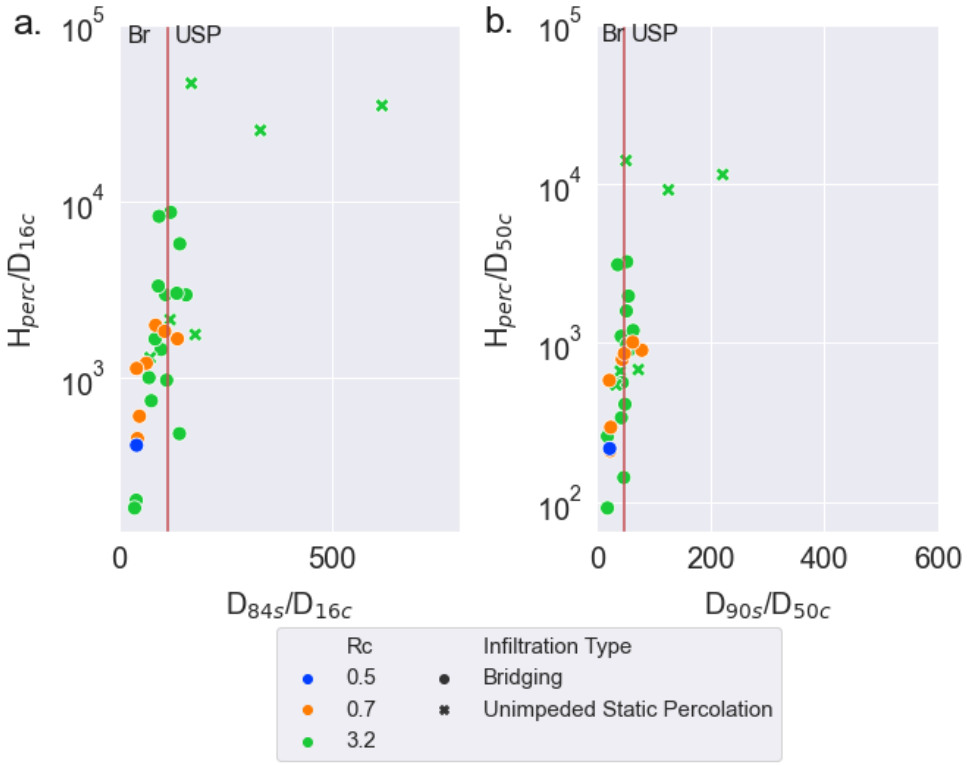

Figure 4.7: Maximum dimensionless infiltration of fine particles into the substrate: **a.** Hperc/D16c vs D84s/D16c and **b.** H_{perc}/D_{50c} vs D_{90s}/D_{50c}. The red lines are the thresholds proposed by Bustamante-Penagos, Niño (2020b). Br: Bridging, USP: Unimpeded static percolation

between H_{perc}/D_{50c} and $W_{spill}*$ implies that the depth of contaminated substrate after a mining accident is independent of the magnitude of the fine material dumped. The highest contamination will be in the first few centimeters of the substrate. Of course, the bigger is the accident, the more area of the river bed is affected.

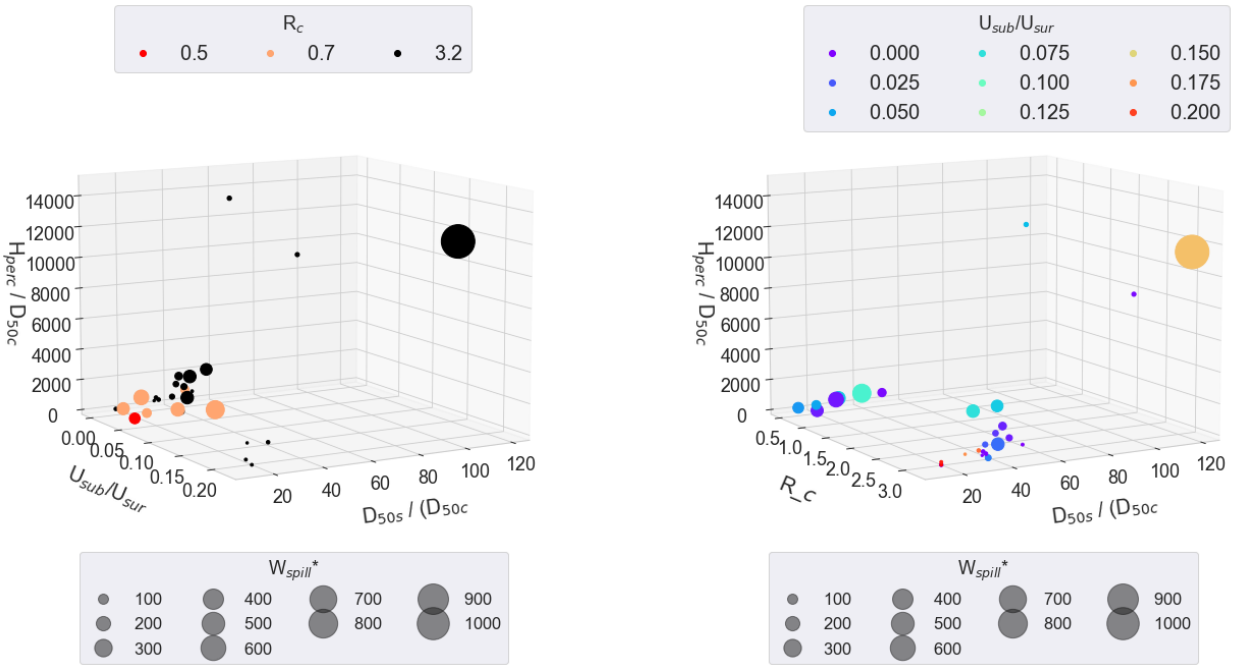

Figure 4.8: Maximum dimensionless infiltration of fine particles into the substrate as a function of: **(a)** Usub/Usur, D50s/D50c and Wspill*; **(b)** R_c, D_{50s}/D_{50c} and W_{spill*}.

Furthermore, Figure 4.8b shows that the dimensionless submerged density is the key parameter for analyzing the infiltration of fine material phenomenon. Note that, $R_c \sim 0.5$ - 0.7 has lower variability than that associated with $R_c \sim 3$ for different D_{50s}/D_{50c}. The dimensionless relationship of the maximum infiltration depth is analyzed as a function of only D_{50s}/D_{50c}, considering $R_c \sim 0.5$ - 0.7 separated from and $R_c \sim 3$. Figure 4.9 shows the experimental data and the trend lines of adjustment (red lines). Figure 4.9a corresponds to $R_c \sim 0.5$-0.7 and Figure 4.9b corresponds to $R_c \sim 3$. The logarithmic functions to characterize the dimensionless relationship of the maximum infiltration depth H_{perc}/D_{50c} as a function of D_{50s}/D_{50c} are reported in equation 4.3. In addition, the metrics of trend lines of the equation 4.3, such as the coefficient of determination r^2, and the root mean square error, RMSE, are for $R_c \sim 0.5$ - 0.7, $r^2 = 0.73$ and RMSE = 159.73. Whereas for $R_c \sim 3$, $r^2 = 0.49$, RMSE = 2758.31.

$$\frac{H_{perc}}{D_{50c}} = \begin{cases} 655.2\ ln\left(0.11\ \dfrac{D_{50s}}{D_{50c}}\right) & R_c \sim 0.5 - 0.7 \\ 5493.9\ ln\left(0.05\ \dfrac{D_{50s}}{D_{50c}}\right) & R_c \sim 3.2 \end{cases} \tag{4.3}$$

According to Figure 4.9, we can report an effect of the velocity ratio, U_{sub}/U_{sur}, and R_c in the maximum dimensionless infiltration depth. However, statistical metrics such as r^2 and

RMSE indicate that the relationship is weak, so we complement the analysis by considering two scales for the velocity ratio, $U_{sub}/U_{sur} < 0.025$ and $0.05 < U_{sub}/U_{sur} < 0.2$ (Figure 4.10). So, the maximum dimensionless infiltration depth as function of D_{50s}/D_{50c}, U_{sub}/U_{sur} and R_c are defined by equations 4.4, with their statistical metrics, r^2 and RMSE. Note that the statistical metrics shows a better correlation between the maximum dimensionless infiltration depth, the ratio of diameters of particles and velocity ratio. Therefore, we can consider an equation of the type $H_{perc}/D_{50c} = A\ ln(B\ D_{50s}/D_{50c})$ where A and B might be functions of U_{sub}/U_{sur}. However, more experiments are needed to determine the relationship between the coefficients A, B with U_{sub}/U_{sur}.

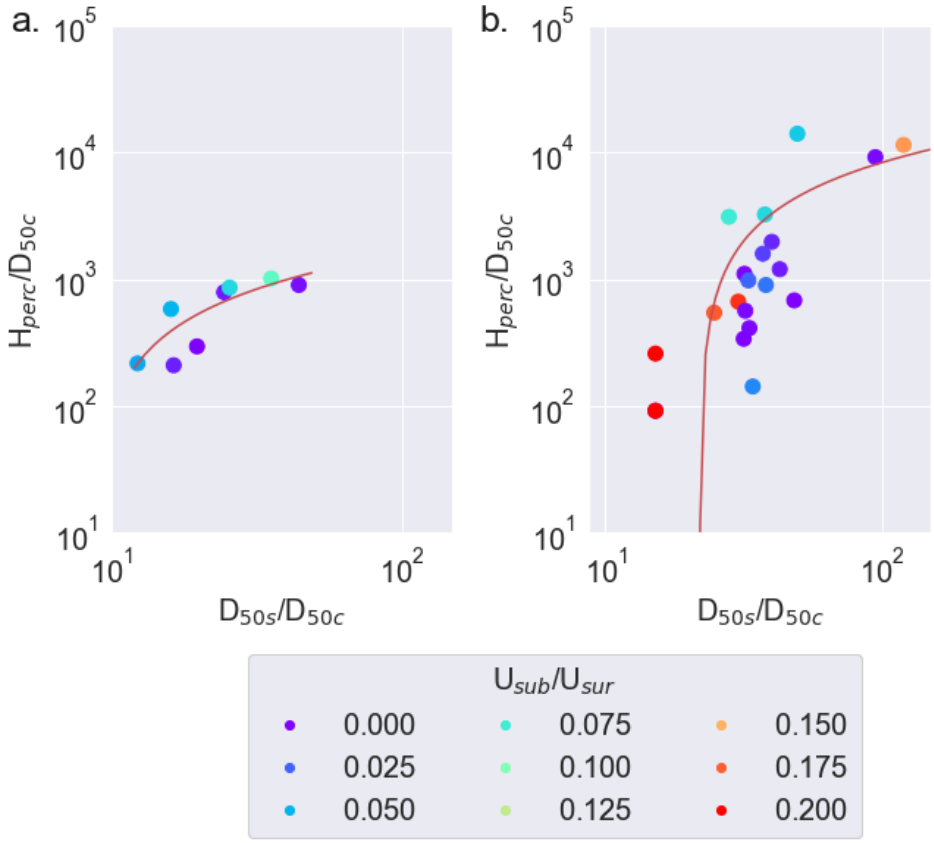

Figure 4.9: Maximum dimensionless infiltration of fine sediment into the substrate as function of the relative submerged density, R_c, and D_{50s}/D_{50c}. Red lines represent the logarithmic trend between H_{perc}/D_{50c} and D_{50s}/D_{50c}, for **a.** R_c ~0.5-0.7 and **b.** R_c ~3.

$$\frac{H_{perc}}{D_{50c}} = \begin{cases} 716.08\, ln\left(0.09\,\dfrac{D_{50s}}{D_{50c}}\right) & R_c \sim 0.5-0.7\ \&\ U_{sub}/U_{sur} < 0.025;\ r^2 = 0.79;\ RMSE = 138 \\ 544.09\, ln\left(0.18\,\dfrac{D_{50s}}{D_{50c}}\right) & R_c \sim 0.5-0.7\ \&\ 0.05 < U_{sub}/U_{sur} < 0.20;\ r^2 = 0.99;\ RMSE = 12 \\ 4752.53\, ln\left(0.04\,\dfrac{D_{50s}}{D_{50c}}\right) & R_c \sim 3.0\ \&\ \ U_{sub}/U_{sur} < 0.025;\ r^2 = 0.62;\ RMSE = 1409 \\ 6647.66\, ln\left(0.06\,\dfrac{D_{50s}}{D_{50c}}\right) & R_c \sim 3.0\ \&\ 0.05 < U_{sub}/U_{sur} < 0.20;\ r^2 = 0.67;\ RMSE = 2966 \end{cases} \tag{4.4}$$

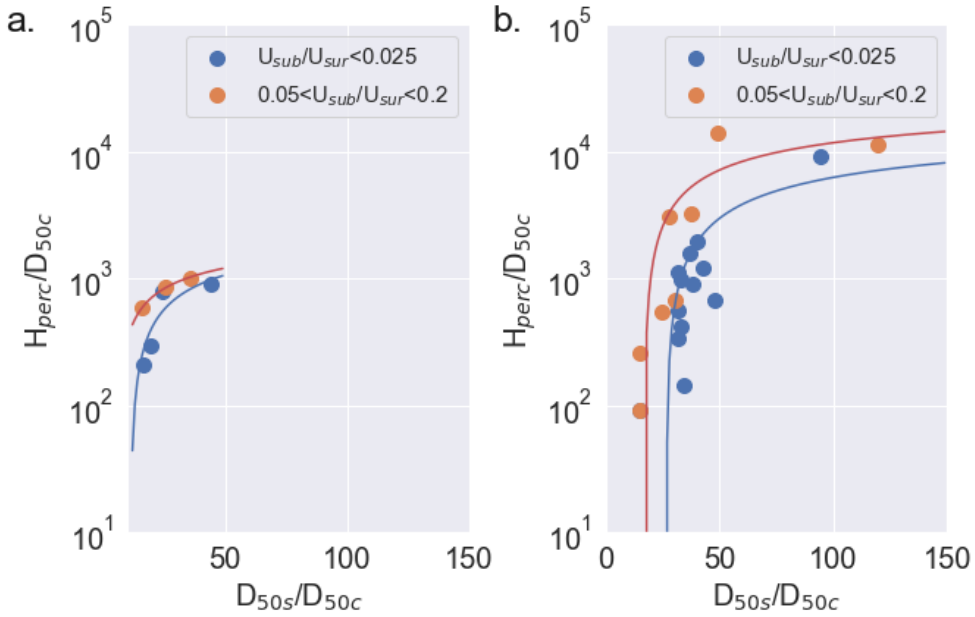

Figure 4.10: Maximum dimensionless infiltration of fine particles into the substrate as a function of R_c, U_{sub}/U_{sur} and **a.** $R_c \sim$ 0.5-0.7 and **b.** $R_c \sim 3$.

4.5 Discussion

4.5.1 Scale Effects

The fine materials used in this research are highly polluting and toxic, so small flumes were considered to avoid high contamination of wastewater. Moreover, the acquisition of granulometric data took approximately a week because it was necessary to sieve the bed, both for the sands and for the fine material, and remove the fine material from the experiments and put them in separate barrels for their disposal. All that made the experiments as small-scale as possible. In addition, researchers such as (Beschta, Jackson, 1979; Carling, 1984; Bustamante-Penagos, Niño, 2020b), reported that the infiltration phenomenon is independent of the hydraulic parameters, so narrow flumes could be considered.

In both facilities, F1 and F2, the ratio $B/H < 5$, so there is a wall effect and the dip phenomenon is present, i.e., the maximum velocities appear below the surface water (Dey, 2014), and the Vanoni correction is necessary to process the velocity field measurements and the bed shear stress (Vanoni, Brooks, 1957).

On the other hand, according to Beschta, Jackson (1979); Carling (1984); Bustamante-Penagos, Niño (2020b), as the infiltration phenomenon is independent of the surface hydraulic parameters, the F1 and F2 have a width of 0.11 m and 0.03 m, respectively, and substrates with a thickness of 30 mm 390 mm. The narrowest flume F2 made it possible to analyze the infiltration depth and subsurface flow simultaneously. Ten experiments were run in F1 and 24 in F2. The 30 mm thick substrate of F1 is sometimes too small to analyze bridging and unimpeded static percolation as infiltration types. F2 allows for an analysis of the infiltration type, considering a larger substrate size. For instance, in F1 unimpeded static percolation was found for very coarse sand. However, in F2, bridging infiltration was found with the same sand. The flows in the experiments in both facilities are with fully developed turbulence.

They have a relative depth, H/D_g, lower than 10, as observed in Table 4.1, i.e., they are macro-roughness flows, such as mountain rivers, and the flow resistance changes regarding the simple rough flow (Limerinos, 1970; Niño, 2002; García, 2008; Niño et al., 2018). In the experiments, the spilled mixture was in the center of the cross-section, and the length of the complete mixing, l, in the cross-section was reached at $l \sim 0.70$ m and $l \sim 0.17$ m for F1 and F2, respectively. The mixing length in F1 and F2 were estimated considering the experimental data reported by Bustamante-Penagos, Niño (2020a) and Bustamante-Penagos, Niño (2020b), respectively. The ratio l/B is 6.6 and 5.8, for F1 and F2, respectively, while in rivers highly polluted by mining accidents such as the Blanco River, in Chile, the complete mixing in the cross-section was reached at $l/B \sim 5.0$. Therefore, we can analyze the suspension dynamics of the spill of copper concentrate in the F1 and F2 experiments, because the experimental setup can represent the natural conditions of gravel-rivers. The experimental setup F2 can allow us to analyze the substrate dynamic of the phenomenon of infiltration of fine material in the substrate, more than the experiments with F1, because it has a thicker substrate.

4.5.2 Visualization of infiltration of fine mineral particles

Infiltration of fine sediments in gravel beds has shown different infiltration patterns, depending on the type of sediment considered as contaminant material. Researchers such as Beschta, Jackson (1979); Diplas, Parker (1985); Niño et al. (2018) reported depositions from the bottom of the bed to the top of the gravel layer. In these studies, fine sediment fed the system at a constant rate. However, the infiltration pattern changes when the fine sediment feed is a point discharge of a hyper-concentrated mixture of fine sediment and water, as in the present research. On the other hand, when a gravel bed is contaminated with sands, Niño et al. (2018) reported a transport of sands within the gravel bed. However, when the contaminating sediment is a cohesive sediment, such as copper concentrate, tailings, or pumicite, this dynamic was not observed. On the contrary, once the copper concentrate is deposited on the substrate, it is only transported vertically when there is a decrease in the phreatic level. Fingers could have an inclination that depends on the depth of the substrate. Substrates with small depth imply vertical fingers without inclination. Conversely, deep substrates imply that the fingers will have an inclination associated with the subsurface flows. Additionally, considering a substrate like the ones we have in this article, we also found that copper concentrate infiltration can be up to 10 times greater than tailings or pumicite.

4.5.3 Infiltration of fine sediment

River pollution associated with the infiltration of fine sediments into the substrate has a high environmental impact because fine sediments can modify the interaction between surface and subsurface flows (Beschta, Jackson, 1979; Diplas, Parker, 1985; Lisle, 1989; Findlay, 1995; Tonina, Buffington, 2009; Shrivastava, 2020). Furthermore, when the fine materials are heavy metals or mineral particles that come from mining activities, the contamination is more critical because these materials are toxic and could reside for a long time in the substrate (Byrne et al., 2018). For example, in Chile, mining companies process copper material as a sulfide ore. It has a characteristic diameter (D_{50}) D_c=40 μm, a density of 4.2 g/cm^3 and

approximately between 30 and 40% is copper and the rest are 24-26% iron, 24-27% sulfur, 2.5-3.0 % aluminum, 0.03% arsenic and other components.
The infiltration depth of fine material has not shown a relationship between flow parameters, and the amount of fine sediment spilled. This behavior has been reported both in this research and by researches such as Beschta, Jackson (1979); Gibson et al. (2009); Bustamante-Penagos, Niño (2020b). Conversely, the geometric relationship between diameters has allowed characterizing the type of infiltration of fine material. However, there is no single threshold to characterize the infiltration phenomenon of fine material. Beschta, Jackson (1979); Gibson et al. (2009); Huston, Fox (2015); Dudill et al. (2016); Bustamante-Penagos, Niño (2020b) reported unimpeded static percolation and bridging as types of infiltration of fine material, although we think that the unimpeded static percolation as a concept should be re-evaluated. The thickness of the substrate becomes key to define the type of infiltration of fine material. For example, we found bridging layers in F2, but in F1 we found unimpeded static percolation. Therefore, the unimpeded static percolation can become bridging in a deeper substrate. At least, with the results shown in this article, particles of tailings ($R_c \sim 0.5 - 0.7$) have no unimpeded static percolation and instead have a bounded bridging value.
The infiltration and deposition of fine mineral particles decrease in depth. That infiltration of fine material dynamics have also been reported in both experimental and field investigations according to Lisle (1989); Diplas, Parker (1985); Wooster et al. (2008); Gibson et al. (2009); Bustamante-Penagos, Niño (2020b), i.e., the decrease in depth deposition has also been validated with natural and non-natural sediments, such as copper concentrate and tailings. This behavior of fine sediment deposition shows that after a mining accident, most of the contaminated material is located in the first layer of riverbed sediments and this is independent of the magnitude of the mining accident.
Figure 4.9 shows that the logarithmic functions characterize the maximum dimensionless infiltration depth of fine material as a function of D_{50s}/D_{50c} and R_c; the coefficients of determination, r^2, are 0.73 for R_c ~0.5-0.7 and 0.49 for R_c ~3. Meanwhile, the coefficients of determination increase up to 28% when both D_{50s}/D_{50c} and U_{sub}/U_{sur} are considered in the analysis. So, this analysis shows that the parameters R_c, D_{50s}/D_{50c}, and U_{sub}/U_{sur} influence the infiltration phenomenon of fine material, but R_c was shown to be key to characterize the infiltration phenomenon of fine material. R_c can generate higher infiltrations of fine material, while the U_{sub}/U_{sur} parameter showed only a weak effect.
In Figure 4.10, for R_c ~0.5-0.7, it is seen that the maximum values for the maximum dimensionless infiltration of fine material reach more or less $1.5x10^3$, when extrapolating the trends indicated there for the values of $D_{50s}/D_{50c} \sim 100$. On the other hand, in Figure 4.10b, for R_c ~3, the maximum values for the maximum dimensionless infiltration of fine material reach values over 10^4, for the values of D_{50s}/D_{50c} ~100. That is, the copper concentrate reaches values of the maximum dimensionless infiltration that are of the order of 10 times that of the pumacite or the tailings.
As reported in the introduction, mining accidents are highly polluting and the residence time in the bed is prolonged. Nevertheless, this article shows that once the fine mining particles infiltrate the bed, there is no bedload transport of contaminant materials. However, fine material can be resuspended during periods of high flows or snowmelt. Therefore, the effect of a mining accident will have long-term effects. According to (CENMA, 2008), near the mines in the Aconcagua river basin, the Aconcagua River and its tributaries have a high sediment transport capacity, which decreases along the river. Namely, the reincorporation of fine material to suspension transport is high in the upper part of the basin and low in

the area near the mouth of the Aconcagua River to the Pacific Ocean. On the other hand, (Byrne et al., 2018) reported that copper may be transported due to seasonal oxidation of fine material or high flows associated with snowmelt and precipitation. So, in the lower part of the Aconcagua river basin, or any mountain river affected by mining activity, for that matter, the entrainment of heavy metals to the surface flow is also associated with the oxidation of heavy metals deposited in the substrate.
In addition, we found that the depth of infiltration of fine material could increase due to the decrease in surface and subsurface flows. This behavior will be typical of ephemeral streams that are being affected by climate change.

4.6 Conclusions

We have analyzed the infiltration of fine mineral particles in the bed of a gravel river, considering the hydraulic parameters of the flow, the mineral particles sizes, the amount of feed material, the density of the fine contaminant material, and the surface and subsurface flows. It was found that neither the amount of fine material dumped nor the hydraulic parameters of the surface flow affect the infiltration depth of fine material. On the other hand, an increase in the contamination of the substrate was found due to a decreasing phreatic level. This behavior could be found in ephemeral streams. It was also found that most of the fine contaminant material is retained in the first few centimeters of the substrate and decreases with depth. Therefore, it was found that the infiltration depth of fine material is independent of the magnitude of the mining accident and the surface layer or active layer of the riverbed is the one that retains most of the contaminating material. The maximum values obtained in this research for the maximum infiltration of tailings particles (R_c ∼0.5-0.7) seem to be close to 1000 D_{50c} and are expected to have no unimpeded static percolation and instead have a bounded bridging value. The copper concentrate reaches values of the maximum dimensionless infiltration that are of the order of 10 times that of the pumacite or the tailings. Furthermore, it was also found that the concept of unimpeded static percolation should be reevaluated since it was found that the type of infiltration of fine material is relative to the depth of the substrate.
Logarithmic functions characterize the maximum dimensionless infiltration depth as a function of D_{50s}/D_{50c} and R_c. The coefficients of determination increase up to 28% when both D_{50s}/D_{50c} and U_{sub}/U_{sur} are considered in the analysis. Therefore, this analysis shows that while the parameters R_c and U_{sub}/U_{sur} have an influence on the infiltration phenomenon, R_c was shown to be the key to characterizing the infiltration phenomenon. R_c can generate higher infiltrations of fine material, while the parameter U_{sub}/U_{sur} shows only a weak effect. Finally, we found that the coefficients of the logarithmic function are a function of the velocity ratio, U_{sub}/U_{sur}. As future work, more experiments that vary the velocity ratio are needed to determine with greater certainty how these coefficients are related to the coefficients with U_{sub}/U_{sur} parameters.

Chapter 5

Conclusion

In this research, the dynamics of a hyper-concentrated mixture of fine minerals particles in a flume with a gravel bed was analyzed. After discharge, the fine particles are transported in suspension, then infiltration into the gravel bed begins, and finally infiltration into the sand. Infiltration patterns appear finger-like, and these patterns may have a slope due to subsurface flows. Furthermore, the infiltration depth can increase in depth when there is a decrease in the water table and this behavior can be found in ephemeral streams.
Bustamante-Penagos, Niño (2020b) were able to characterize the sediment infiltration phenomenon as bridging and unimpeded static percolation. However, in Bustamante-Penagos, Niño (2021) were found that unimpeded static percolation is relative to substrate depth, because the experiments that achieved unimpeded static percolation reported by Bustamante-Penagos, Niño (2020b), where the substrate depth was approximately 0.05 m. Whereas, the infiltration was reported as bridging in Bustamante-Penagos, Niño (2021) , where the substrate depth was approximately 0.4 m.
On the other hand, sediment infiltration was analyzed considering, relative sediment density $R_c = (\rho_c - \rho)\rho$, dimensionless diameter relationships, relationship between subsurface and surface flow velocity, U_{sub}/U_{sur}. The research shows that while the parameters R_c and U_{sub}/U_{sur} have an influence on the infiltration phenomenon, R_c showed to be the key to characterizing the infiltration phenomenon. R_c can generate higher infiltration, while the ratio U_{sub}/U_{sur} shows only a weak effect.
On the other hand, that greater amount of the fine contaminant material is retained in the first few centimeters of the substrate and decreases with depth. However, the infiltration depth is independent of the magnitude of the spill, i.e., the magnitude of the mining accident, and the surface layer or active layer of the riverbed is the one that retains most of the contaminating material. Nevertheless, the maximum infiltration does depend on the type of fine material, the copper concentrate reaches values of the maximum dimensionless infiltration that are of the order of 10 times that of the pumacite or the tailings.
Sediment ejection is generated at a change in gravel bed permeability, constant inflow of surface and subsurface flows, a fine exposition ratio e/D_g ∼-0.1, a relative sediment density, R_c ∼0.5-0.7, and a low mean surface velocity. Subsurface flow upwelling is generated by clogging of internal channels in the gravel bed and the seal layer formed at gravel-sand interface. So, when the interstitial spaces of the sand and gravel are clogged with fine

material, flow infiltration to greater depths is limited. These flow ejections are generated by the downstream clogging of the internal gravel channels, which destabilize the fine sediment seals formed after the deposition of the fine sediment from the lower part of the gravel bed. Sediment ejection modifies the vertical velocity component such that Taylor's frozen turbulence hypothesis is no valid in the neighbourhood of the bed. Furthermore, this ejection also modifies the distribution of the power density spectrum. The spectral analysis shows structures of large scale and super large scale of motion, both vertical velocity fluctuation, w', and streamwise velocity fluctuations, u'. However, at the center and downstream of the ejection, the motion of large-scale turbulent structures has a higher concentration of the power spectrum density associated with vertical velocity fluctuation, w', dominate over streamwise velocity fluctuations, u'. Conversely, upstream of the ejection the vertical velocity fluctuation, w' has a higher concentration of the power spectrum density. In addition, the distribution of velocity fluctuations in the quadrant analysis changes after sediment ejection, with inward and outward interactions becoming more frequent than in a channel without sediment ejection. The sediment ejections reported by (Bustamante-Penagos, Niño, 2020a) were identified under special experimental conditions, a small flume and dimensionless number low. In rivers, these sediment ejections would be found in areas of water upwelling and in beds with an extended grain size curve, because sediment ejections are associated with the upwelling of subsurface flows.

Future Work

This research analyzed the dynamics of a hyper-concentrated mixture of particles in an open channel for three types of fine materials, pumicite, copper concentrate and tailings. It was found that independent of sediment density, there is initially suspended transport, deposition and finally infiltration. When analyzing the infiltration of sediments in gravel beds, it was found that the hydraulic parameters of surface and subsurface flow, geometric relationships and the relative density of the sediment have an influence on the infiltration depth. Although, the research reported a weak effect between dimensionless infiltration depth and velocity ratio, U_{sub}/U_{sur}, it is required to continue with this line of research to decrease the uncertainty in the estimation of infiltration depths. On the other hand, heavy metals in their solid phase tend to deposit on the bed and restart their downstream transport when there is scour or transport of coarse particles from the bed. When the heavy metals begin transporting, the particles are transported in suspension and not as bedload transport. According to our observation in a trip or Colorado in 2019 these dynamics were observed both for copper concentrate, at laboratory scale, and manganese in natural streams at Silverton, Colorado. In the case of natural stream the pH was about 3. Therefore, the characterization of the evolution of the heavy metal concentration in the neighborhood of the bed zone is a key line of work to estimate the time of highest concentration once the initial spill has passed. On the other hand, when the sediment-water mixture begins the infiltration into the substrate, the fine particles move by an "internal suspension" before settling on the substrate. Therefore, the neighborhood within the pores of the bed will allow us to know how the velocity varies in the first centimeters of the substrate and thus determine more accurately the interaction between surface and subsurface flow. These measurements can be performed by considering a ultrasonic velocity profile (UVP) into the bed.
Finally, the pumicite sediment ejection reported in Bustamante-Penagos, Niño (2020a) paper,

was also found from taillings and it is required to characterize the thresholds triggering sediment ejection and to characterize through stereo PIV this sediment ejection to analyze turbulence intensities in three components.

Bibliography

Aceituno Nicolas. Experimental study of the transport of mining tailings due to accidents in a flow with gravel. 2017.

Addison P. S., Watson J. N., Feng T. Low-oscillation complex wavelets // Journal of Sound and Vibration. 2002. 254, 4. 733–762.

Adrian Ronald J. Particle-Imaging Techniques for Experimental Fluid Mechanics // Annu. Rev. Fluid Mech. 1991. 23, 1. 261–304.

Adrian Ronald J. Hairpin vortex organization in wall turbulence // Physics of Fluids. 2007. 19, 4.

Amankwah R. K., Pickles C. A. Microwave roasting of a carbonaceous sulphidic gold concentrate // Minerals Engineering. 2009. 22, 13. 1095–1101.

Ambiente Seremi de Medio. Officials of the Ministry of the Enviroment of Valparaíso Participate in the last monitoring campaign of the Blanco River, In spanish. 2016.

Bagnold R. A. An Approach to the Sediment Transport Problem from General Physics. Washington, 1966. 42.

Bailly Christophe, Comte-Bellot Geneviève. Turbulence. 2015. 360. (Experiments Fluid Mechanics. Springer).

Balakumar B. J., Adrian R. J. Large- and very-large-scale motions in channel and boundary-layer flows // Philosophical Transactions of the Royal Society A: Mathematical, Physical and Engineering Sciences. 2007. 365, 1852. 665–681.

Bendat Julius S., Piersol Allan G. Random Data: Analysis and Measurement Procedures. 2010. 604.

Benito G., Benito-Calvo Alfonso, Gallart Francesc, Martín-Vide Juan Pedro, Regües David, Bladé Ernest. Hydrological and geomorphological criteria to evaluate the dispersion risk of waste sludge generated by the Aznalcollar mine spill (SW Spain) // Environmental Geology. 2001. 40, 4-5. 417–428.

Beschta Robert., Jackson William. The Intrusion of Fine Sediments into a Stable Gravel Bed // J. Fish. Res. Board Canada. 1979. 36. 204–210.

Bronshtein I.N., Semendyayev K.A., Musiol G, Muehlig H. Handbook of Mathematics. New York: Springer, 2007. 5th. 741–743.

Bustamante N, Tapia C, Niño Y. Experimental Study of Copper Concentrate Spill in Gravel Beds // XXIII Congreso Chileno de Ingeniería Hidráulica. In Spanish. Valparaiso, Chile, 2017. 14.

Bustamante-Penagos N., Niño Y. Flow–Sediment Turbulent Ejections: Interaction between Surface and Subsurface Flow in Gravel-Bed Contaminated by Fine Sediment // Water. 2020a. 12, 6. 1589.

Bustamante-Penagos N., Niño Y. Suspension and infiltration of copper concentrate in a gravel bed: a flume study to evaluate the fate of a potential spill in a Chilean river // Environmental Earth Sciences. 2020b. 79, 24. 1–12.

Bustamante-Penagos Natalia, Niño Yarko. Percolation of the copper concentrate in a porous medium // XXVIII Congreso Latinoamericano Hidráulica. In Spanish. Buenos Aires, Argentina: IAHR, 2018. 2076–2084.

Bustamante-Penagos Natalia, Niño Yarko. Copper concentrate and gravel beds // 38th IAHR World Congress. 1, 1. Panama: IAHR, 2019. 5080–5090.

Bustamante-Penagos Natalia, Niño Yarko. Infiltration depth of mineral particles in gravel-bed rivers // Minerals. 2021. 11, 1285. 1–20.

Byrne Patrick, Hudson-Edwards Karen A., Bird Graham, Macklin Mark G., Brewer Paul A., Williams Richard D., Jamieson Heather E. Water quality impacts and river system recovery following the 2014 Mount Polley mine tailings dam spill, British Columbia, Canada // Applied Geochemistry. 2018. 91, January. 64–74.

Byrne Patrick, Hudson-edwards Karen, Macklin Mark, Brewer Paul, Bird Graham. The long-term environmental impacts of the Mount Polley mine tailings spill, British Columbia, Canada // Geophysical Research Abstracts. 2015. 17, 1. 6241.

CENMA . Analysis of the physical-chemical composition of river sediments and their relationship with the availability of metals in water in the Aconcagua river basin. Santiago, 2008. S.I.T. N° 207 Volume IV of V.

Cameron S. M., Nikora V. I., Stewart M. T. Very-large-scale motions in rough-bed open-channel flow // Journal of Fluid Mechanics. 2017. 814. 416–429.

Carling Paul A. Deposition of Fine and Coarse Sand in an Open-Work Gravel Bed // Canadian Journal of Fisheries and Aquatic Sciences. 1984. 41, 2. 263–270.

Carmo Flávio Fonseca do, Kamino Luciana Hiromi Yoshino, Junior Rogério Tobias, Campos Iara Christina de, Carmo Felipe Fonseca do, Silvino Guilherme, Castro Kenedy Junio da Silva Xavier de, Mauro Mateus Leite, Rodrigues Nelson Uchoa Alonso, Souza Miranda Marcos Paulo de, Pinto Carlos Eduardo Ferreira. Fundão tailings dam failures: the environment tragedy of the largest technological disaster of Brazilian mining in global

context // Perspectives in Ecology and Conservation. 2017. 15, 3. 145–151.

Cenedese A., Romano G. P., Di Felice F. Experimental testing of Taylor's hypothesis by L.D.A. in highly turbulent flow // Experiments in Fluids. 1991. 11, 6. 351–358.

Chanson H., Treventhan M., Koch C. Discussions and clousers. Turbulence Measurements with Acoustic Doppler Velocimeters // Journal of Hydraulic Engineering. 2007. 131, 12. 1283–1295.

Chen Kebing, Zhang Yifan, Zhong Qiang. Wavelet coherency structure in open channel flow // Water (Switzerland). 2019. 11, 8.

Chow Ven Te. Hidraulica De Canales Abiertos. 1995. 647.

Cohen Ed A.K., Walden Andrew T. A statistical analysis of Morse wavelet coherence // IEEE Transactions on Signal Processing. 2010. 58, 3 PART 1. 980–989.

Cooper James R., Ockleford Annie, Rice Stephen P., Powell D. Mark. Does the permeability of gravel river beds affect near-bed hydrodynamics? // Earth Surface Processes and Landforms. 2018. 43, 5. 943–955.

Coulthard Tom J., Macklin Mark G. Modeling long-term contamination in river systems from historical metal mining // Geology. 2003. 31, 5. 451–454.

Cui Yantao, Parker Gary. The arrested gravel front: stable gravel-sand transitions in rivers Part 2: General numerical solution // Journal of Hydraulic Researc. 1998. 36, 2. 159 –182.

Cui Yantao, Wooster John K., Baker Peter F., Dusterhoff Scott R., Sklar Leonard S., Dietrich William E. Theory of fine sediment infiltration into immobile gravel bed // Journal of Hydraulic Engineering. 2008. 134, 10. 1421–1429.

Davis W. The Geographical Cycle // The Geographical Journal. 1899. 14, 5. 481–504.

Dermisis Dimitrios, Papanicolaou A. N.Thanos. The effects of protruding rock boulders in regulating sediment intrusion within the hyporheic zone of mountain streams // Journal of Mountain Science. 2014. 11, 6. 1466–1477.

Dey Subhasish. Fluvial Hydrodynamics. 2014. Springer. 706.

Dey Subhasish, Papanicolaou Athanasios. Sediment threshold under stream flow: A state-of-the-art review // KSCE Journal of Civil Engineering. 2008. 12, 1. 45–60.

Diplas P, Parker G. Pollution of Gravel Spawning Grounds due to Fine Sediment. 240, 240. 1985. 192.

Dudill Ashley, Frey Philippe, Church Michael. Infiltration of fine sediment into a coarse mobile bed : a phenomenological study // Earth Surf. Process. Landforms. 2016. 42, December 2016. 1171–1185.

Edroma B Y Eric L. Copper Pollution in Rwenzori National Park, Uganda // Journal of

Applied Ecology. 1974. 11, 3. 1043–1056.

El Ciudadano . Minera Los Pelambres, responsable de nuevo derrame tóxico en el río Choapa. 2009.

Findlay Stuart. Importance of surface-subsurface exchange in stream ecosystems: The hyporheic zone // Limnology and Oceanography. 1995. 40, 1. 159–164.

Fischer H. B., List E. J., Koh R. C.Y., Imberger J., Brooks N. H. Mixing in inland and coastal waters. San Diego, California: Harcourt Brace Jovanovich, 1979. 483.

Fox James F, Asce M. Prediction of the Clogging Profile Using the Apparent Porosity and Momentum Impulse // Journal of Hydraulic Engineering. 2016. 142, 11. 1–10.

Fuentes G., Viñals J., Herreros O. Hydrothermal purification and enrichment of Chilean copper concentrates. Part 2: The behavior of the bulk concentrates // Hydrometallurgy. 2009. 95, 1-2. 113–120.

Fuentes J. Estudio Experimental del Transporte de Sedimento Mediante Tomógrafo en el Marco de la Evaluación de la Contaminación de Ríos por Sedimento Fino. 2017. 108.

García Carlos M, Cantero Mariano I, Niño Yarko, García M H. Turbulence Measurements with Acoustic Doppler Velocimeters // Journal of Hydraulic Engineering. 2005. 131, 12. 1062–1073.

García Carlos M., García Marcelo H. Characterization of flow turbulence in large-scale bubble-plume experiments // Experiments in Fluids. 2006. 41, 1. 91–101.

García M., López F., Niño Y. Characterization of near-bed coherent structures in turbulent open channel flow using synchronized high-speed video and hot-film measurements // Experiments in Fluids. 1995. 19, 1. 16–28.

García Marcelo, Parker Gary. Entraiment of Bed Sediment into Suspension // J. Hydraul. Eng. 1991. 117, 4. 414–435.

García Marcelo H. Sediment transport and morphodynamics // Sedimentation Engineering processes, measurements, modeling, and practice. 10, 110. 2008. 2, 21–163.

Geremew Africa M., Yanful Ernest K. Role of fines on cohesive behavior of mine tailings inferred from critical shear stress // Canadian Geotechnical Journal. 2011. 48, 4. 568–582.

Gibson S., Abraham D., Heath R., Schoellhamer D. Bridging Process Threshold for Sediment Infiltrating into a Coarse Substrate // Journal of Geotechnical and Geoenvironmental Engineering, ASCE. 2010. 136, 2. 402–406.

Gibson S., Abraham David, Heath Ronald, Schoellhamer David. Vertical gradational variability of fines deposited in a gravel framework // Sedimentology. 2009. 56, 3. 661–676.

Govil P. K., Sorlie J. E., Sujatha D., Krishna A. K., Murthy N. N., Mohan K. Rama.

Assessment of heavy metal pollution in lake sediments of Katedan Industrial Development Area, Hyderabad, India // Environ. Earth Sci. 2012. 1. 121–128.

Grinsted A., Moore J. C., Jevrejeva S. Application of the cross wavelet transform and wavelet coherence to geophysical time series // Nonlinear Processes in Geophysics. 2004. 11, 5/6. 561–566.

Hofland B. Rock & Roll: Turbulence-induced damage to granular bed protections. 2005. 1–241.

Huston Davis L, Fox James F. Clogging of Fine Sediment within Gravel Substrates : Dimensional Analysis and Macroanalysis of Experiments in Hydraulic Flumes // J. Hydraul. Eng. 2015. 141, 8. 1–14.

Iseya Fujiko, Ikeda Hiroshi. Pulsations in bedload transport rates induced by a longitudinal sediment sorting: A flume study using sand and gravel mixtures // Geografiska Annaler. Series A. Physical Geography. 1987. 69, 1. 15–27.

Jackson Roscoe G. Sedimentological and fluid-dynamic implications of the turbulent bursting phenomenon in geophysical flows // Journal of Fluid Mechanics. 1976. 77, 3. 531–560.

Jaskuła Joanna, Sojka Mariusz, Fiedler Michał, Wróżyński Rafał. Analysis of spatial variability of river bottom sediment pollution with heavy metals and assessment of potential ecological hazard for the Warta river, Poland // Minerals. 2021. 11, 3. 1–21.

Julien P Y. Erosion and sedimentation. New York: Cambridge University Press, 2010. 371.

Advances in Water Resources Experimental observations on fine sand winnowing from immobile gravel substrate. // . 2020. 142.

Kuhnle R. A., Wren D. G., Langendoen E. J., Rigby J.R. Sand Transport over an Immobile Gravel Substrate R. // ASCE Journal of Hydraulic Engineering. 2013. 138, July. 642–652.

La Tercera . Codelco inició investigación interna por derrame de concentrado de cobre en el río Blanco. 2016.

Lichtner Derek T. Turbulent interactions between stream flow and near-subsurface flow: A laboratory approach using particle image velocimetry and refractive index matching - Thesis Master of Science in Geology. 2015. 279.

Limerinos J.T. Determination of the Manning coefficient from measured bed roughness in natural channels (Report No. 1898-B). 1970. 53.

Lisle E. Sediment Transport and Resulting Deposition in Spawning Gravels , North Coastal California " by Thomas E . Lisle // Water Resources Research. 1989. 25, 10. 1303–1319.

Liu Xiaoyang, Bai Zhongke, Shi Huading, Zhou Wei, Liu Xiaocai. Heavy metal pollution of soils from coal mines in China // Natural Hazards. 2019. 99, 2. 1163–1177.

Lloyd Denby S, Koenings Jeffrey P, LaPerriere Jacqueline D. Effects of Turbidity in Fresh Waters of Alaska // North Am. J. Fish. Manag. 1987. 7, 1. 18–33.

López Fabian, García Marcelo H. Risk of Sediment Erosion and Suspension in Turbulent Flows // J. Hydraul. Eng. 2001. 1, March. 231–235.

Macklin Mark G., Brewer Paul A., Hudson-edwards Karen A., Bird G., Coulthard T. J., Dennis I. A., Lechler P. J., Miller Jerry R., Turner J. N. A geomorphological approach to the management of rivers contaminated by metal mining // Geomorphology. 2006. 79, 3-4. 423–447.

Manes Costantino, Pokrajac Dubravka, McEwan Ian, Nikora Vladimir. Turbulence structure of open channel flows over permeable and impermeable beds: A comparative study // Physics of Fluids. 2009. 21, 12. 1–12.

Mcdowell-Boyer Laura M, Hunt James R, Sitar Nicholas. Particle Transport Through Porous Media // Water Resour. Res. 1986. 22, 13. 1901–1921.

Nakagawa H., Tsujimoto T., Shimizu Y. Turbulent flow with small relative submergence // Lect. Notes Earth Sci. Fluv. Hydraul. Mt. Reg. 1991. 33–44.

Nikora V., Nokes R., Veale W., Davidson M., Jirka G. H. Large-scale turbulent structure of uniform shallow free-surface flows // Environ. Fluid Mech. 2007. 7, 2. 159–172.

Nikora Vladimir. Flow turbulence over mobile gravel-bed: spectral scaling and coherent structures // Acta Geophysica Polonica. 2005. 53, 4. 539.

Nikora Vladimir, Goring Derek, McEwan Ian, Griffiths George. Spatially Averaged Open-Channel Flow Over Rough Bed // J. Hydraul. Eng. 2001. 127, February. 123–133.

Nikora Vladimir, Koll Katinka, McEwan Ian, McLean Stephen, Dittrich Andreas. Velocity distribution in the roughness layer of rough-bed flows // Journal of Hydraulic Engineering. 2004. 130, 10. 1036–1042.

Niño Y., García M. H. Experiments on particle - turbulence interactions in the near - wall region of an open channel flow: implications for sediment transport // Journal of Fluid Mechanics. 1996. 326. 285–319.

Niño Yarko. Simple Model for Downstream Variation of Median Sediment Size in Chilean Rivers // Journal of Hydraulic Engineering. 2002. 128, October. 934–941.

Niño Yarko, Licanqueo William, Janampa Ciro, Tamburrino Aldo. Front of unimpeded infiltrated sand moving as sediment transport through immobile coarse gravel // Journal of Hydraulic Research. 2018. 1686, 0022-1686. 18.

Niño Yarko, Lopez Fabian, Garcia Marcelo. Threshold for particle entrainment into suspension // Sedimentology. 2003. 50, 2. 247–263.

Niño Yarko, Musalem Rodrigo. Turbulent entrainment events of sediment grains over

bedforms // Proceedings of the Fourteenth Engineering Mechanics Conference. Austin, Texas: The University of Texas at Austin, 2000. 6.

Nuñez-González Francisco. Infiltration of fine sediment mixtures through poorly sorted immobile // Water Resources Research. 2016. 52, 12. 9306–9324.

Núñez-González Francisco, Martín-Vide Juan Pedro, Kleinhans Maarten G. Porosity and size gradation of saturated gravel with percolated fines // Sedimentology. 2016. 63, 5. 1209–1232.

Parker G., Cui Y., Imran J., Dietrich W. Flood- ing in the lower Ok Tedi, Papua New Guinea, due to the disposal of mine tailings and its amelioration. // Proceedings, Int. Semin. Recent trends floods their Prev. Meas. Hokkaido, Japan: Hokkaido Disaster Prevention Research Center, 1996. 29.

Parker Gary, Klingeman Peter C. On why gravel bed streams are paved // Water Resources Research. 1982. 18, 5. 1409–1423.

Perrier Valérie, Philipovitch Thierry, Basdevant Claude. Wavelet spectra compared to Fourier spectra // Journal of Mathematical Physics. 1995. 36, 3. 1506–1519.

Rijn Leo van. Sediment Transport, Parte II: Suspended Load Transport // J. Hydraul. Eng. 1984. 110, 11. 1613–1641.

Robinson S. Coherent Motions In The Turbulent Boundary Layer // Annual Review of Fluid Mechanics. 1991. 23, 1. 601–639.

Rosgen David L. A classification of natural rivers // CATENA. 1994. 22, 3. 169–199.

Roussinova V. Turbulent structures in smooth and rough open channel flows: effect of depth. 2009. 184.

Sambrook Smith Gregory H., Nicholas A. P., Ferguson R. I. Measuring and defining bimodal sediments : Problems and implications // Water Resources Research. 1997. 33, 5. 1179–1185.

Sambrook Smith Gregory H., Nicholas Andrew P. Effect on flow structure of sand deposition on a gravel bed: Results from a two-dimensional flume experiment // Water Resources Research. 2005. 41, W10450. 1–12.

Shamloo Hamid, Pirzadeh Bahareh. Analysis of roughness density and flow submergence effects on turbulence flow characteristics in open channels using a large eddy simulation // Applied Mathematical Modelling. 2015. 39, 3-4. 1074–1086.

Shields a. Application of Similarity Principles and Turbulence Research to Bed-Load Movement // Mitt. Preuss. Versuchsanst. Wasserbau Schiffbau. 1936. 26, 5-24. 47.

Shrivastava Shivansh. Influence of bioturbation and fine sediment clogging on hyporheic exchange in streams. 1, April. 2020. 0–2.

Soublette N., Heyer A., Cortes I. Preliminary and confirmatory investigation of soils with potential presence of contaminants (SPPC). Illapel city. (Spanish). 2011. 46.

Szlapczynski Rafal, Szlapczynska Joanna. An analysis of domain-based ship collision risk parameters // Ocean Engineering. 2016. 126. 47–56.

Tamburrino Aldo. Visualization of flow structures in low reynolds turbulent open-channel flows // Mechanics Research Communications. 1997. 24, 1. 33–40.

Tamburrino Aldo, Gulliver John S. Large flow structures in a turbulent open channel flow // Journal of Hydraulic Research. 1999. 37, 3. 363–380.

Thoms M. C. Channel sedimentation within the urbanized river Tame, U.K. // Regulated Rivers: Research & Management. 1987. 1, 3. 229–246.

Tonina Daniele, Buffington John M. Hyporheic Exchange in Mountain Rivers I : Mechanics and Environmental Effects // Geogr. Compass. 2009. 3, 3. 1063–1086.

Torrence Christopher, Compo Gilbert. A practical guide to wavelet analysis // Bulletin of the American Meteorological Society. 1998. 79, 1. 61–78.

Van Niekerk H. J., Viljoen M. J. Causes and consequences of the Merriespruit and other tailings-dam failures // Land Degradation and Development. 2005. 16, 2. 201–212.

Vanoni Vito a, Brooks Norman H. Laboratory Studies of the Roughness and Suspended Load of Alluvial Streams. 112, N° E-68. Pasadena, CA, 1957. 130.

Wallace James M. Quadrant Analysis in Turbulence Research: History and Evolution // Annual Review of Fluid Mechanics. 2016. 48, 1. 131–158.

Wood Pj, Armitage Pd. Biological Effects of Fine Sediment in the Lotic Environment // Environ. Manage. 1997. 21, 2. 203–217.

Wooster John K., Dusterhoff Scott R., Cui Yantao, Sklar Leonard S., Dietrich William E., Malko Mary. Sediment supply and relative size distribution effects on fine sediment infiltration into immobile gravels // Water Resources Research. 2008. 44, W03424. 1–18.

Wren D. G., Langendoen E. J., Kuhnle R. A. Effects of sand addition on turbulent flow over an immobile gravel bed // Journal of Geophysical Research: Earth Surface. 2011. 116, 1. 1–12.

Yolcubal Irfan, Demiray Ayda Doğrul, Çiftçi Emin, Sanğu Ercan. Environmental impact of mining activities on surface water and sediment qualities around Murgul copper mine, Northeastern Turkey // Environmental Earth Sciences. 2016. 75, 21.

Zhong Qiang, Chen Qigang, Wang Hao, Li Danxun, Wang Xingkui. Statistical analysis of turbulent super-streamwise vortices based on observations of streaky structures near the free surface in the smooth open channel flow // Journal of the American Water Resources

Association. 2016. 5, 3. 2–2.

Zhong Qiang, Li Danxun, Chen Qigang, Wang Xingkui. Coherent structures and their interactions in smooth open channel flows // Environmental Fluid Mechanics. 2015. 15, 3. 653–672.

Appendices

Annexed A

Copper concentrate and gravel beds

This chapter has been published in 38th IAHR World Congress. (2019) Bustamante-Penagos N. y Niño Yarko.

Abstract
Mining accidents can pollute gravel bed rivers with fine, metal materials, in particular with copper concentrate. This research shows the experimental advances on the spill of copper concentrate in gravel beds, with two approaches; first, in a flume with a bed and second, in a sediment column with surface flow and subsurface flow. Particle Image Velocimetry was applied for the measurement of the flow velocity before and after the spill, finding a maximum decrease of 9% in the bed shear stress. On the other hand, considering both facilities, the thresholds to characterize unimpeded static percolation and bridging, as types of percolation, were specified.

Keywords: Percolation; copper concentrate; suspension; unimpeded static percolation; bridging.

Introduction

The Chilean geomorphology in the regions north and center of the country are controlled by Los Andes Mountain range. This lithological control leads to high slopes and gravel bed rivers. Niño (2002) reported median sediment size between 0.3-250 mm and slopes between 0.04-8.61%. On the other hand, mining is the most common economic activity in those regions, that is, the extraction, refining, and exportation of copper concentrate. Mining is located far from the ports where the copper concentrate goes or the places where the tailings are placed, so the material is transported through pipelines or channels, which are nearby to rivers. Hence, mining accidents, for example, pipeline failure, have a high environmental impact on water resources, because mining materials contain toxic material and heavy metals. For example, naming a few accidents, failures in the dam of Harmoni Golden mine spilled 2.5 Mton of tailing that destroyed the mining village of Merriespruit, South Africa (Van

Niekerk, Viljoen, 2005); failures in a valve generated 45 m^3 spill of copper concentrate into the Choapa River, Chile (El Ciudadano, 2009); breakdown of an underground pipeline spilled 50 m^3 of copper concentrate into the Blanco River, Chile (La Tercera, 2016); the breakage of the tailings dam at Mount Polley spilled 25 Mm^3 into the Hazeltine Creek, Quesnel Lake and Polley Lake, Canada (Byrne et al., 2015); a failure of Fundão tailings dam spilled 43 Mm^3 into the Doce River to the Atlantic Ocean, Brazil (Carmo do et al., 2017).
On the other hand, the contamination of gravel-bed rivers with a fine material has high environmental impact. Due to the presence of fine sediment in the bed, it could change the roughness, velocity field and shear stress (Sambrook Smith, Nicholas, 2005; Niño et al., 2018). Additionally, there are changes in the hyporheic zone because the fine particles can change the permeability by filling the pores of the sediment (Mcdowell-Boyer et al., 1986). Several researchers have studied the pollution of gravel bed with sand or glass spheres as fine material. Einstein 1968 in (Beschta, Jackson, 1979), Diplas, Parker (1985); Cui, Parker (1998); Iseya, Ikeda (1987) researched experimentally the percolation dynamics of fine sediment into the gravel beds. They reported that the percolation depth depends on the size of the coarse material. They also identified two mechanisms of percolation such as unimpeded static percolation and bridging. Additionally they could not find a relationship between the hydraulic parameters and the percolation depth. On the other hand, (Cui, Parker, 1998) proposed that the gravel porosity is a reservoir for the interstitial deposition of fine sediment. Cui et al. (2008) could report a decrease in the accumulation of fine sediment deposited with depth into the substrate. Several studies show different thresholds to characterize the percolation type, such as the relationship of the sediment sizes, e.g., Beschta, Jackson (1979); Gibson et al. (2009); Huston, Fox (2015); Dudill et al. (2016). In fact, when sands are the pollutant material, typical mechanisms of sediment transport are observed, and its advance is a wavefront (Niño et al., 2018).
Nowadays, not too many papers have used mining materials as pollutants. Aceituno (2017) studied the pollution of gravel bed with tailings as fine material, finding that tailings are deposited in sort of dunes in the gravel bed and advance is not a wavefront but is in individual particles. Bustamante et al. (2017); Bustamante-Penagos, Niño (2018) used copper concentrate as fine material. They found that the movement of copper concentrate into the substrate has a dominant vertical movement like fingers. This paper has as aim showing the dynamic of pollution of gravel beds with copper concentrate, as fine material, through two experimental approaches.

Experimental setup

Experiment of dynamics of copper concentrate in flume

Experiments were conducted in a recirculation flume with 0.11 m wide, 3.0 m long, 0.15 m deep and variable slope between 0.007 and 0.047 (see Figure A.1). The sediment bed has two layers, superficial (gravel) and substrate (sand) (see Figure A.1). This was for the copper concentrate has such a small size that gravel has always unimpeded static percolation and only the sand can form bridges. In the spill zone there is a non-erodible impermeable plate that aims to avoid the scour due to the pouring copper concentrate. Bustamante et al. (2017) reported that the copper concentrate was fed through the free surface and transported in suspension; for this reason the experimental arrangement has a mobile chute that conducts

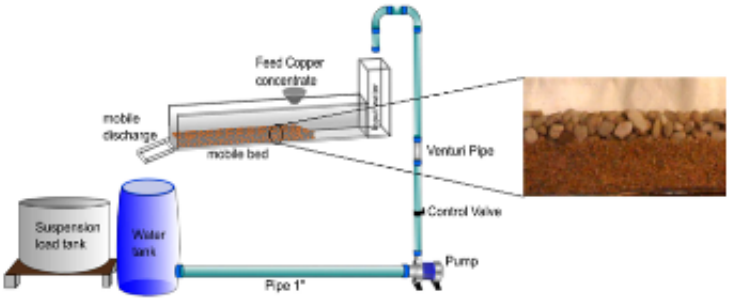

Figure A.1: Experimental setup used in the percolation of copper concentrate in open channel.

the suspended copper concentrate into a tank for collecting it and avoid recirculation of the concentrate in the system. There is a water reserve system, which becomes operational once the copper concentrate is poured into the channel and stops operating when the suspended material passed all downstream of the flume to the tank and the mobile discharge returns to its initial state.

Experiment of percolation of copper concentrate in a sediment column

Experiments were conducted in a sediment column with 0.03 m wide, 0.58 m long and variable slope (see Figure A.2). This sediment column has two layers of sediment, similar to the experiment 1, gravel and sand. With this experimental setup it was possible to independently measure the surface and subsurface flow and percolation depth until 480 mm.

Materials and instrumentation

The sediment setup in both experiments has two layers of sediment; the surface layer is of gravel, 20 mm thickness and mean diameter of $D_g = 10$ mm, and the subsurface layer for the experiments in the flume is of sand, of 30 mm thickness and mean diameter, D_s, is variable between 0.2 and 3.35 mm, in different runs (Figure A.3). The subsurface layer in the experiments in the sediment column is of sand or fine gravel, 390 mm thickness and mean diameter between 0.7 y 5.7 mm, for different runs (Figure A.3). The density of both materials, gravel and sand, is 2.65 gr/cm^3. On the other hand, the copper concentrate has a characteristic diameter (D_{50}) of $D_c = 40$ μ and a density of 4.2 gr/cm^3. The net weight of copper concentrate was 2.8 kg for the experiments in the flume and 0.07 kg and 0.2 kg for the experiments in the sediment column. Furthermore, the copper concentrate is poured with a concentration of 70% by weight, to avoid encapsulation and in analogy to pipeline failure, the copper concentrate was fed through an acrylic cone in the free surface, of 2.83 cm of diameter, during 7 s for the experiment in the flume, and 1.0 cm of diameter during 6s for the experiments in the sediment column.
The measurement of flow rate, Q, was through a Venturi pipe for the experiments in the flume and volumetric gauge for the surface and subsurface flow in the experiments in the sediment column. A Fastcam Mini UX50 camera was used for Particle Image Velocimetry. This camera takes up to 2500 fps. A Nikon D3200 camera was used for percolation analysis of copper concentrate. The Malvern Master Sizer 2000 equipment of the Laboratory of Sedimentology of Universidad de Chile was used for measurement the grain size distribution of copper concentrate. Table A.1 contains the hydraulic parameters of all the experiments,

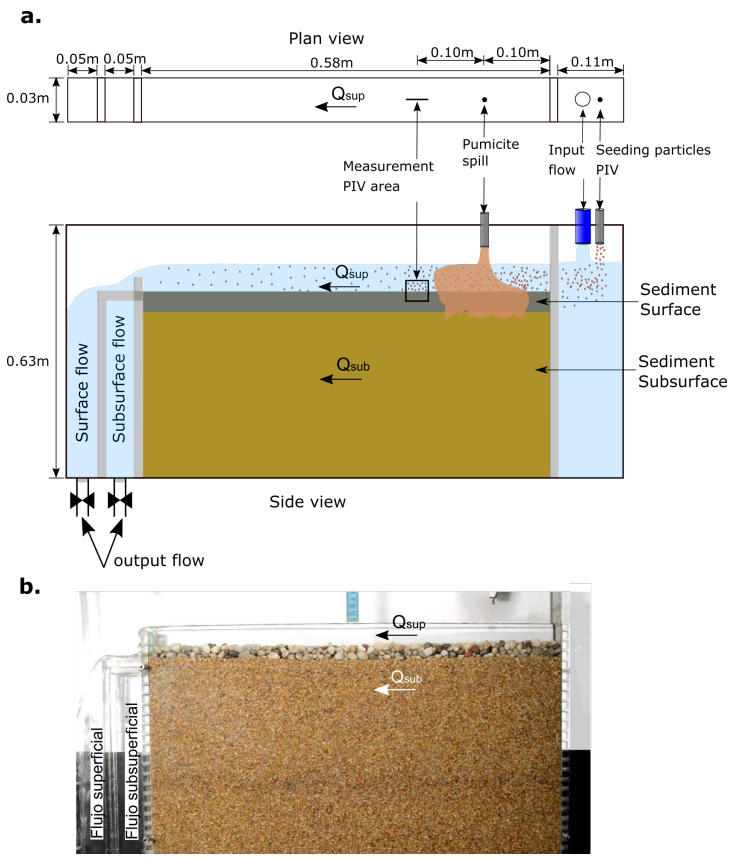

Figure A.2: Experimental setup used in the percolation of copper concentrate in porous media.

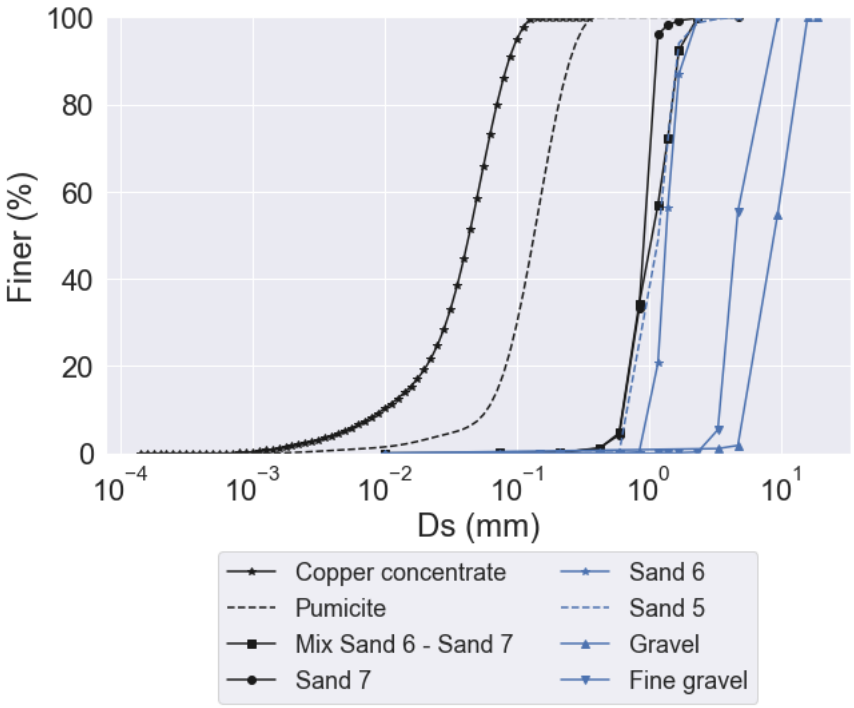

Figure A.3: Grain size distribution of gravel, sand and copper concentrate in the flume and porous media experiments.

Table A.1: Hydraulic parameters of flume and sediment column experiments

Exp	Q_{sur}	Q_{sub}	b	h	A	V	R_h	S	u_*	Re	Fr
#	l/s	l/s	m	m	m^2	m/s	m	–	m/s	–	–
1f	0.610	0	0.11	0.025	0.0028	0.222	0.017	0.047	0.089	5507	0.45
2f	0.610	0		0.026	0.0028	0.215	0.018	0.047	0.090	5507	0.43
3f	0.610	0		0.025	0.0028	0.222	0.017	0.047	0.089	5507	0.45
4f	1.950	0		0.025	0.0028	0.709	0.017	0.047	0.089	17604	1.43
5f	1.950	0		0.040	0.0044	0.443	0.023	0.047	0.103	17604	0.71
6f	1.820	0		0.052	0.0057	0.321	0.027	0.007	0.043	16458	0.45
7f	1.820	0		0.052	0.0057	0.321	0.027	0.007	0.043	16458	0.45
8f	2.450	0		0.062	0.0068	0.360	0.029	0.007	0.044	22158	0.46
9f	2.300	0		0.058	0,0064	0.361	0.028	0.007	0.044	20764	0.48
10f	2.500	0		0.048	0.0053	0.482	0.026	0.016	0.064	22973	0.70
1pm	0.000	0	0.03	0.019	0.00057	0.000	0.0084	0.000	0.000	0.000	0.000
2pm	0.060	0.004		0.010	0.00030	0.200	0.006	0.028	0.041	2000	0.639
3pm	0.033	0.013		0.028	0.00083	0.040	0.010	0.002	0.013	1091	0.076
4pm	0.070	0.006		0.033	0.00100	0.076	0.010	0.003	0.019	2514	0.133
5pm	0.053	0.006		0.033	0.00100	0.053	0.010	0.007	0.027	1767	0.093
6pm	0.103	0.004		0.026	0.00077	0.133	0.009	0.005	0.022	3423	0.264
7pm	0.057	0.046		0.031	0.00103	0.055	0.011	0.007	0.027	1718	0.100
8pm	0.108	0.026		0.026	0.00079	0.136	0.010	0.016	0.038	3590	0.266
9pm	0.078	0.034		0.067	0.00201	0.039	0.012	0.007	0.029	2600	0.048
10pm	0.110	0.035		0.057	0.00172	0.064	0.012	0.017	0.045	3667	0.085
11pm	0.020	0.040		0.031	0.00094	0.021	0.010	0.002	0.013	653	0.037

with "f" as sub-index are the flume experiments and "pm" are sediment column experiments, where Q_{sur} and Q_{sub}, are the surface and subsurface discharge; h, depth, A, wetted area; V, section mean flow velocity; R_h, hydraulic radius; S, slope of the channel; $u_* = \sqrt{g\ S\ R_h}$, theoretical bulk shear velocity; $Fr = V/\sqrt{gH}$, Froude number; g, gravitational acceleration, and $Re = V\ h/\nu$, Reynolds number with ν the kinematic viscosity.

Results

Spill and deposit of copper concentrate

After a spill of the copper concentrate in the fume, there are suspension transport, percolation into the substrate and low entrainment. For measuring the copper concentrate deposited in the bed, the total length of the flume was divided into seven sections. Figure A.4, shows the weight of copper concentrate deposited in each section per unit bed area, W_{bed}, made dimensionless with the total weight the copper concentrate poured per unit bed area of the flume, $Wtot$, as a function of the longitudinal coordinate made dimensionless with the diameter of the copper concentrate feeding acrylic cone, X_*. The blue box represents the zone of the spill. Note that, upstream from the area of spill a percolation of copper concentration was also observed, i.e., after a mining accident it is possible to affect a region upstream of the river. In fact, the maximum deposit of copper concentrate is located near the place where the

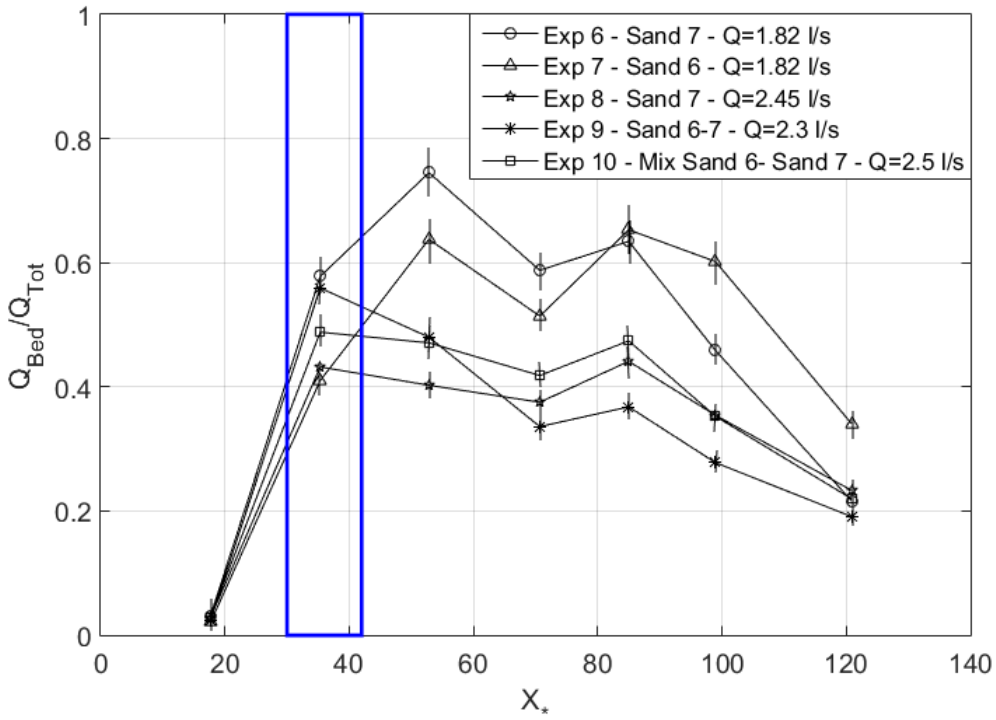

Figure A.4: Distribution of copper concentrate dimensionless weight per unit area of copper concentrate along the channel after the spill.

spill occurs, however, the non-erodible impermeable plate placed in the spill zone prevented more of the copper concentrate from being deposited in this zone.

On the other hand, Figure A.5 shows the effect of the relationship between surface flow, Q, and the flow rate of copper concentrate, Q_{spill}, in the longitudinal distribution of copper concentrate deposited in the bed. Additionally, the experiments with red line correspond to the experiments where the maximum percolation was 30 mm. It is observed that the lower the Q/Q_{spill} ratio, the greater the deposition of copper concentrate along the channel. This relationship is directly related to the ratio w_s/u_*, where w_s is the settling velocity of copper concentrate, i.e., lower Q/Q_{spill}, higher w_s/u_*, lower turbulence and therefore the particles tend to deposit more quickly than for a higher Q/Q_{spill} ratio. Implicitly, it is related to the shear velocity (u_*) as observed in Table A.2, where the shear velocities measured experimentally in the channel are reported, also validating that at a lower shear velocity greater deposition of copper concentrate in the bed .

Shear stress

In the experiment in the flume the velocities fields were measured, and these were analyzed considering the methodology proposed by Nikora et al. (2001), i.e., the total shear was defined as: $\tau_{tot} = \tau_\nu + \tau_t + \tau_f$, with τ_ν is the viscous component ($\tau_\nu = \mu\, \partial\overline{u}/\partial z$), τ_t is the turbulent component ($\tau_t = -\rho(\overline{u'\, w'})$) and the τ_f is the form-induced component ($\tau_f = -\rho\langle\tilde{u}\tilde{w}\rangle$), where μ is the dynamic viscosity, $\overline{u}$ is the mean velocity, u' and w' are the velocity fluctuations in longitudinal coordinate (x) and vertical coordinate (z), respectively. $\tilde{u}$ an $\tilde{w}$ are the form

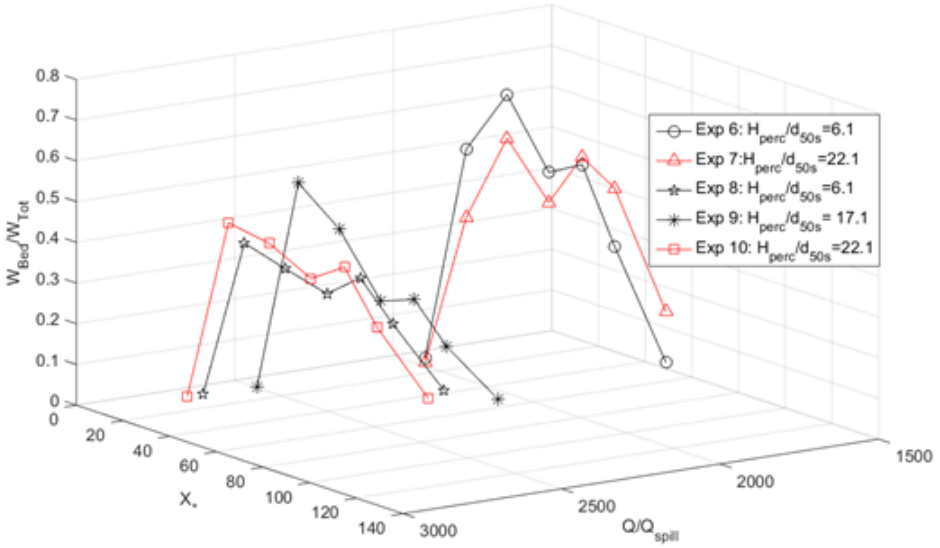

Figure A.5: Effect of the relation Q/Q_{spill} in the longitudinal distribution of the copper concentrate deposited in the bed.

Table A.2: Experimental mean shear velocities before (bcc) and after (acc) the spill.

Exp	u_* [m/s]	
#	bcc	acc
7f	0.028	0.029
8f	0.036	0.035
9f	0.034	0.034
10f	0.044	0.040

induced disturbance in longitudinal coordinate (x) and vertical coordinate (z), respectively. On the other hand, three planes were considered in the cross section for measuring the velocity fields in each experiment, before and after the spill of copper concentrate. Those points were located at y/B =1/2 (P1), y/B=1/4 (P2) and y/B=1/8 (P3). However, when the ratio $h/b < 3$, as it can be deduced in Table 1, the experiments are conducted in a narrow channel and according to Chow (1995) it will have strong secondary currents and we could observe the dip phenomenon in the velocity profiles and hence in the shear stress profiles. Figure 6 shows the shear stress made dimensionless with the bed shear stress of each plane, τ_0.
On the other hand, to estimate the shear velocity in the section an effective area per each plane was considered and a weighted average can be estimated for each experiment, before and after of the spill of copper concentrate. Table A.2 contains the mean shear velocity for the complete section and it is possible to deduce that the copper concentrate into the bed have shown a maximum decrease close to 9% in the shear velocity. Figure A.7 shows the relation between mean shear velocity before and after the spill of copper concentrate in the flume.

Percolation

The percolation phenomenon was analyzed with two approaches, in a flume and a sediment column. In the first case, the maximum percolation that could be evaluated was 30 mm.

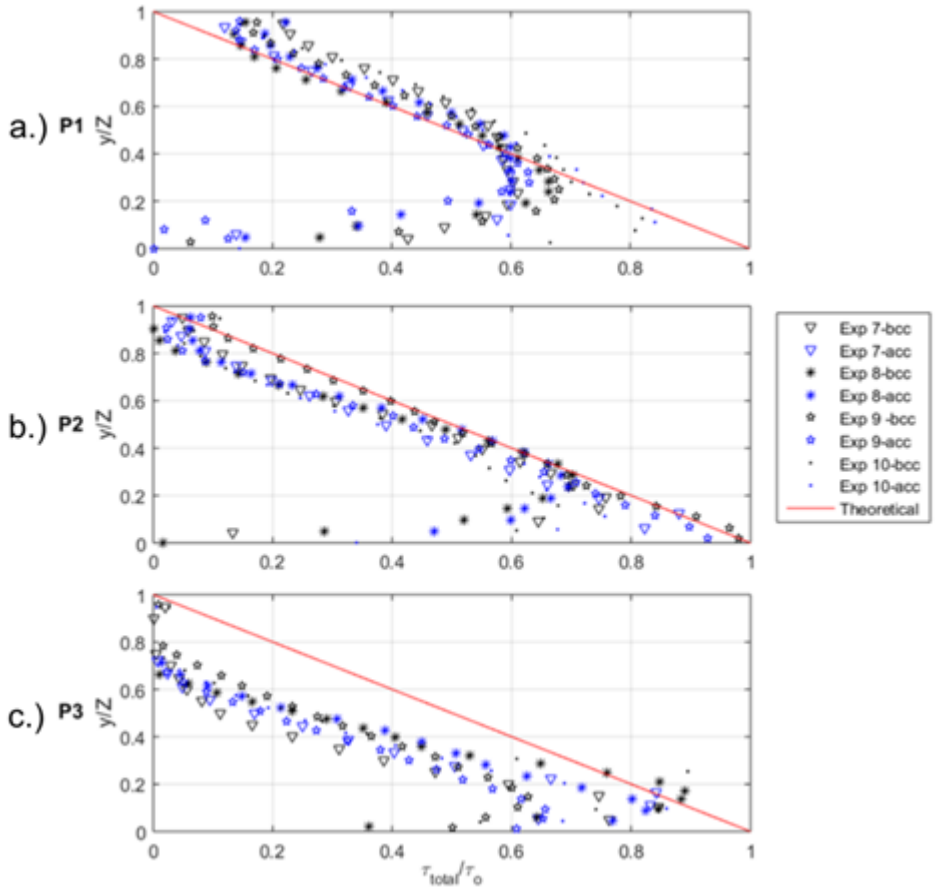

Figure A.6: Velocity and shear stress in the experiment 1. Profiles **a.)** P1; **b.)** P2; **c.)** P3.

In the second case, the maximum percolation depth was 480 mm. In both cases, bridging or unimpeded static percolation was found. For the percolation in the sediment column, an inclination of the fingers was found in the direction of the subsurface flow. Bustamante et al. (2017) showed an independence between the percolation depth and the surface flow parameters for the experiments in the flume. However, for the second case, it is necessary to analyze the percolation depth with the relationship between surface flows and subsurface, Q_{sur}/Q_{sub} and the weight of copper concentrate poured in the spill, W_{spill}. In Figure A.8 results of the images analysis for two final states of percolation are shown, where the dark tone implies the presence of copper concentrate. In Figure A.8a Q_{sur}/Q_{sub} >0 is considered and it can be seen fingers inclined. This inclination depends on the sediment diameter of the sublayer of sediment, i.e. fine sediment implies a small size of pores and short and vertical percolations. When the percolation achieves a steady state we start the second part of the experiment, that is considering Q_{sup}/Q_{sur} =0 and final state is shown in Figure A.8b. As a result, there is an increase of the percolation depth of the copper concentrate with inclination. Note that the tones in the Figure 8b is lighter than in Figure 8a because it shows the increase in percolation, i.e. Figure A.8b is the result of the evolution of copper concentrate in the final state Figure A.8a until to the maximum percolation state. Table A.3 reports the weight of copper concentrate poured in the spill, W_{spill}, the weight and mean size of copper concentrate deposited into the bed, W_{perc} and d_{50c}, the maximum percolation depth, H_{perc}, and the characteristic size of sand, d_{50} and d_{90}, for each run of the experiments

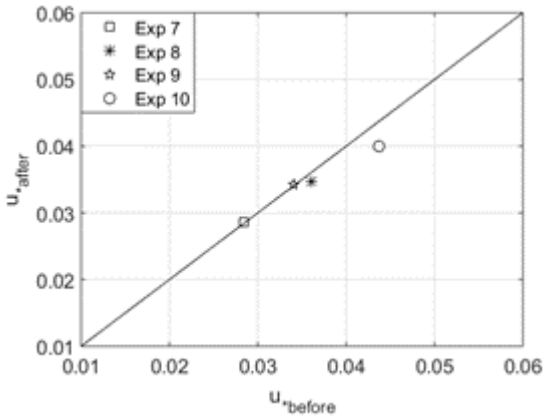

Figure A.7: Relationship between shear velocity before and after the spill of copper concentrate.

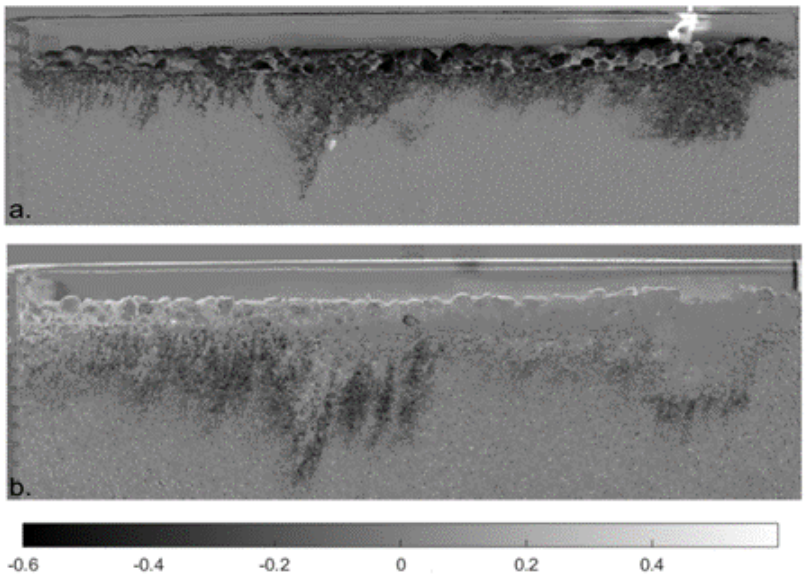

Figure A.8: Percolation of copper concentrate into the bed in the sediment column.

in the flume and in the sediment column.

According to Bustamante et al. (2017), the percolation depth does not have a dependence with Reynolds number, Froude number or Shields number, and they proposed dimensionless relationships to characterize the type of percolation depending on grain size of sediment and the copper concentrate. Considering the experiments in the flume and in the sediment column, those relationships are the ones observed in Figure 9. The geometric relationships presented in Figure 9a and Figure 9c, are good dimensionless relationships to characterize the percolation types. In the experiments in the flume, the sediment sublayer is of 30 mm, so for this experimental setup unimpeded static percolation was considered if the depth percolation was 30 mm (red star in Figure A.9). But, considering the results in the sediment column, it is possible to think that if the thickness sublayer is greater, we could see bridging or unimpeded static percolation. Conversely, the relationship presented in Figure 9b is not a good dimensionless relationship to characterize the type of percolation, for there was a

Table A.3: Spill data: Weight poured of copper concentrate, maximum percolation depth, grain size of copper concentrate and sand.

W_{spill} gr	d_{50c} μm	W_{perc} gr	H_{perc} mm	d_{50} mm	d_{90} mm
2800	42.6	739.1	14.6	1.36	1.85
	43.8	810.91	30.0*	2.12	3.20
	61.8	1748.1	5.7	0.94	1.15
	45.4	1611.0	30.0*	1.36	1.85
	62.3	1174.7	5.7	0.94	1.15
	61.6	667.1	16.1	0.94	1.15
	55.2	501.6	30.0*	1.36	1.85
	70.4	739.1	8.1	1.08	1.66
	57.2	810.91	30.0*	1.19	1.69
70	28.4	36.2	43.9	1.29	1.68
	28.4	12.6	142.9	1.59	2.18
	37.1	36.7	41.0	1.18	1.58
	61.5	34.5	34.7	1.97	2.75
	57.0	2.6	23.52	1.89	2.81
	50.2	47.7	45.3	1.91	2.82
	53.4	36.5	85.0	1.98	2.77
80	50.4	28	77.4	4.6	8.43
100	43.8	59.4	52.6	1.87	2.79
200	47.8	136.5	94.4	1.91	2.65
	46.8	110	430.0	4.43	5.88
	52.2	119.4	169.4	1.97	2.74
	44.0	118.9	136.8	1.23	1.61
	37.5	147.2	430.0	4.49	8.3

* Unimpeded static percolation reported in the flume experiment.

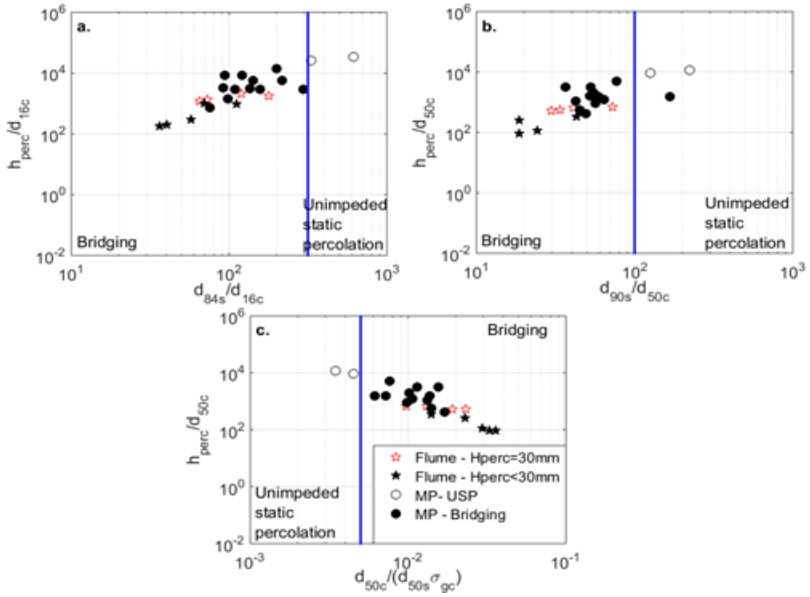

Figure A.9: Geometric relationships of maximum percolation of copper concentrate into the substrate **a.** h_{perc}/D_{16c} vs d_{84s}/d_{16c}, b. h_{perc}/d_{50c} vs d_{90s}/d_{50c}, c. h_{perc}/d_{50c} vs $d_{50c}/(d_{50s}\sigma_{gc})$. USP is Unimpeded Static Percolation.

particular experiment in the sediment column that do not obey the blue line that separates bridging from unimpeded static percolation. It is necessary to analyze the dimensionless relationships for the percolation depth as function of the weight of the copper concentrate poured and relation of flows Q_{sub}/Q_{sur}. In Figure A.10 it is shown the first approximation of the relationship between type of percolation, d_{90s}/d_{50c}, Q_{sub}/Q_{sur}, and dimensionless relationship of spill weight, $W_{spill}/(\rho\ R_c\ d_{50c}^3)$, finding that:

$$\frac{d_{90s}}{d_{50c}} + \frac{1}{3\times 10^6}\frac{w_{spil}}{\rho\ R_c d_{50c}^3} > 300, \quad \forall \quad Q_{sub}/Q_{sur}\ \ Unimpeded\ Static\ Percolation\ zone \tag{A.1}$$

$$\frac{d_{90s}}{d_{50c}} + \frac{1}{3\times 10^6}\frac{w_{spill}}{\rho R_c d_{50c}^3} < 300, \quad \forall Q_{sub}/Q_{sur}\ \ Bridging \tag{A.2}$$

Note that the gray plane in Figure A.10 shows an independence between the types of percolation and the dimensionless relationship of surface and subsurface flows, in this case $\alpha = 0$. However, it is necessary to make more experiments to analyze whether $\alpha = 0$ or $\alpha \neq 0$ (red plane in Figure A.10), i.e., we will characterize the percolation phenomenon as a function of diameters of the materials, surface and subsurface flows and the dimensionless weight of copper concentrate poured in the spill.

Conclusions

This research allowed to characterize the dynamics of copper concentrate after a spill in gravel beds through two experimental approaches, finding that the copper concentrate poured into the flume is transported in suspension and then percolated in the sediment column.

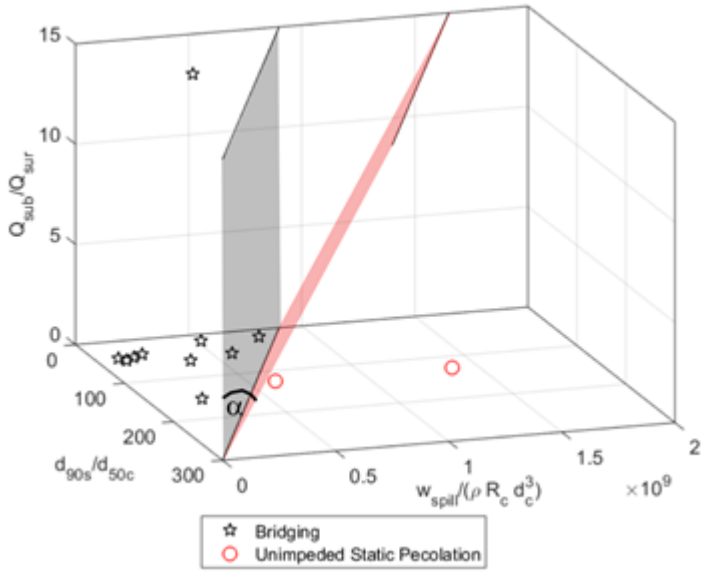

Figure A.10: Type of percolation as a function of d_{90s}/d_{50c},d_{90s}/d_{50c} and $W_{spill}/(\rho_c d_{50c^3})$.

There is no relationship between the surface flow parameters and the percolation depth. However, increasing the relationship Q_{sub}/Q_{sur} has the effect of increasing the depth and inclination of the percolation.

Although the hydraulic parameters of the flow are not related to the percolation depth of the copper concentrate, the transport in suspension of the metal depends on the ratio Q/Q_{spill}. That is, the lower the Q/Q_{spill} is, the greater the copper concentrate deposition along of the bed. The percolation phenomenon of copper concentrate is characterized, considering both experimental setups, as unimpeded static percolation or bridging. But the depth percolation of fine material in coarse sediment reported by Beschta, Jackson (1979); Diplas, Parker (1985); Gibson et al. (2010); Huston, Fox (2015); Dudill et al. (2016), are not valid when the fine material is copper concentrate because they found that maximum percolation depth is of the order of $2 - 5\ d_{90g}$, where d_{90g} is the d_{90} of the coarse sediment. For copper concentrate the percolation depth is much higher than this value.

On the other hand, we analyze the copper concentrate percolation in the sediment column as a function of dimensionless parameters $W_{spill}/(\rho\ R_c\ d_{50c}^3)$, Q_{sub}/Q_{sur} and d_{90s}/d_{50c}. This research is in progress and we must carry out more experiments in the unimpeded static percolation zone and thus complement the characterization of percolation of copper concentrate in the sediment column.

Annexed B

Fine sediment and turbulent interactions of permeable beds

This chapter has been published in XXV Chilean congress of hydraulic engineering. (2021). Bustamante-Penagos N, Fuentes J. y Niño Y. (In Spanish)

Abstract

This paper presents an analysis of the variation of the values and spectral density of the vertical velocities of an alluvial stream in the neighbourhood of a gravel bed, contaminated with fine sediments. The objective of this work is to determine how turbulent interactions are modified in the neighbourhood of a gravel bed, in which fine sediment has infiltrated. Particle Image Velocimetry (PIV) velocimetry data from three experimental facilities of the Francisco Javier Dominguez laboratory of the University of Chile are considered. The analysis considers a space between two particles (a pore in this paper) in a gravel bed and takes into account three points in the bed, upstream of the pore, in the pore and downstream of the pore. We reported that the pore can generate modifications in the vertical flow velocity around the pore by infiltration of fine sediment. When there is a low-density fine sediment ejection, the Taylor frozen turbulence hypothesis is no longer valid. Finally, we concluded that, when there is no sediment ejection in a gravel bed contaminated with fine sediment, there is also no change in either the vertical component of the velocity or the spectral density distribution.

Introduction

Natural disasters such as debris flows, volcanic eruptions, floods or human activity can introduce large amounts of fine sediments into gravel beds, generating a high environmental impact, since the presence of fine sediments in the substrate can modify the flow dynamics in the hyporheic zone. Fine particles can modify permeability and when deposited within the pores change the hydraulic conductivity of the substrate (Dermisis, Papanicolaou, 2014; Khademishamami, Nardin, 2020; Mcdowell-Boyer et al., 1986). Additionally, fine material that is deposited within the interstitial spaces in gravel beds can reduce grain roughness

(Iseya, Ikeda, 1987; Niño et al., 2018).
After a particle is deposited on the bed, it can be entreiment into the suspended transport. Researchers such as Bagnold (1966); López, García (2001); Niño et al. (2003), and others, have determined thresholds to characterize sediment entraiment and suspended transport. Robinson (1991); García et al. (1995); Niño, García (1996), and others, have proposed that fine particles can entraiment into suspended transport under the action of coherent structures that can contribute to vertical momentum transport. Researchers such as Tamburrino (1997); Adrian (2007); Zhong et al. (2015, 2016), and others, reported small-scale, $l \sim H$, large-scale, $l \sim 3H$, and longitudinal superscale, $l > 10H$ structures, where l is the longitudinal scale of the vortex or coherent structure, and H is the depth of the water sheet. Additionally, turbulent structures have been analyzed by means of a quadrant analysis, in a Cartesian plane, of the axial and vertical velocities of the flow, where in Quadrant 1 are the outward interactions, in Quadrant 2 are the ejections, in Quadrant 3 are the inward interactions and in Quadrant 4 are the sweeps. Through this analysis it has been reported that the most frequent turbulent interactions are those in Quadrant 2 and 4, while the turbulent interactions in quadrant 1 and 3 are less frequent. In addition, sweep-type interactions are more efficient for the reincorporation of fine particles from the bed (Niño, Musalem, 2000). However, Bustamante-Penagos, Niño (2020a) reported experimental results of fine sediment, pumicite, infiltrating a gravel bed with subsurface flow, where there are fine sediment ejections into the surface flow. These ejections are an upwelling of the subsurface flow to the surface flow that transports sediment vertically in a quasi-steady state. These ejections modify the presence of turbulent interactions. That is, ejections and sweeps type interactions do not predominate. The dynamics of these ejections allowed us to question, under what conditions the contamination of a gravel bed with fine particles can modify the vertical velocity patterns, the Taylor's frozen turbulence hypothesis and the spectral density distribution. These ejection motivated the analysis of both vortex motion scales and a spectral analysis, by means of the Wavelet transform, for the velocity in the neighbourhood of the fine particle contaminated velocity gravel bed. Velocimetry data from Fuentes (2017); Bustamante-Penagos, Niño (2020a,b), were considered for this analysis.

Experimental setup

The experiments were conducted in three different experimental installations, but all facilities had a gravel bed and a fine contaminating sediment. The first facility was that of Fuentes (2017). The experimental setup consisted of a closed pipe system, 0.1 m in diameter and 10 m in length, 8 m of PVC pipe and 2 m of clear acrylic. Inside the 8 m pipe there is a gravel bed fixed on an acrylic surface along the pipe, in order to avoid sediment deposition in this sector. Downstream there is a transparent pipe, 2 m long. The gravel bed in this sector is immobile, and the thickness of the gravel layer is 0.05 m. The characteristic diameter of the gravels (D_{g50}) was 10 mm. The fine particles were glass particles and their mean diameter (D_{f50}) was 0.12 mm (Figure B.1a). The second setup was the setup of (Bustamante-Penagos, Niño, 2020b). The experimental setup consisted of a variable slope channel, with a width of 0.11 m and length of 3.0 m. The bed configuration had two sediment layers; the subsurface layer, 0.03 m thick, was sand whose characteristic diameter (D_{s50}) varied between 0.2 and 3.35 mm; the surface layer was 0.02 m thick, was gravel and its characteristic diameter (D_{g50}) was 10 mm. The fine particles were copper concentrate with a mean diameter (D_{f50}) of 40 μm

(Figure B.1b). Finally, the experimental setup of (Bustamante-Penagos, Niño, 2020a) was a 0.03 m wide, 0.58 m long channel and the bed configuration had two sediment layers. The subsurface layer, 0.39 m thick, was sands whose characteristic diameter (D_{s50}) was 2.45 mm; the surface layer, 0.02 m thick, was gravels whose characteristic diameter (D_{g50}) was 10 mm and the fine particles were pumicite with a mean diameter (D_{f50}) of 0.12 mm (Figure B.1cc). Fuentes (2017); Bustamante-Penagos, Niño (2020a,b) implemented the Particle Image Velocimetry (PIV) technique for velocity field measurement. Fuentes (2017); Bustamante-Penagos, Niño (2020b) considered particles of 75 μm mean diameter, with rhodamine, a laser light of wavelength 532 nm. Bustamante-Penagos, Niño (2020a) used pumicite particles as tracers for PIV implementation. A Photron FASTCAM Mini UX50 camera, whose maximum sampling rate is 2500 fps was used for image acquisition and data processing was performed with PIVLab software.

Table B.1 presents the hydraulic parameters of the experiments, where d_{f50} the mean fine particle diameter, Q is the flow rate, U is the mean flow velocity, u_* is the frictional velocity, which was estimated as $u_* = \sqrt{\tau_0/\rho}$, where τ_0 is the shear stress at the bottom, obtained experimentally from the results with PIV, and ρ is the fluid density.

Table B.1: Hydraulic parameters.

Research	Particles	d_{f50} mm	Q l/s	U m/s	u_* m/s	H m
Fuentes (2017)	Particle glasses	0.12	1.4	0.38	0.044	0.050
Bustamante-Penagos, Niño (2020a)	Pumicite	0.12	0.09	0.052	0.0023	0.067
Bustamante-Penagos, Niño (2020b)	Copper concentrate	0.04	1.8	0.29	0.043	0.056

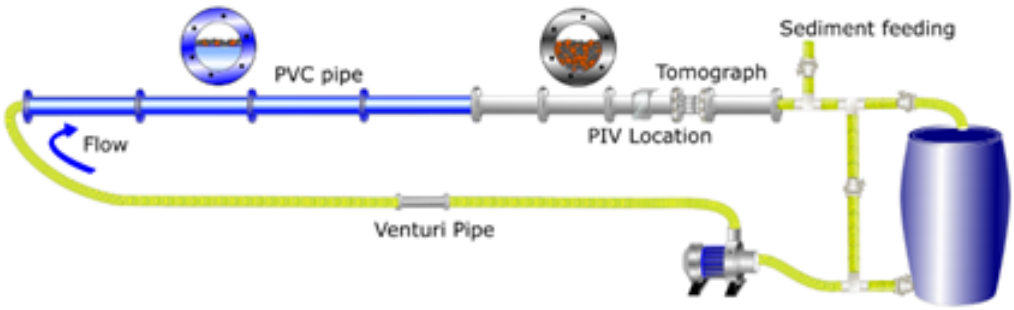

(a) Closed system, with fixed gravel bed in the blue section of the pipeline and immobile gravel bed in the gray section of the pipeline. Experimental scheme considered to investigate contamination of gravel beds with glass particles.

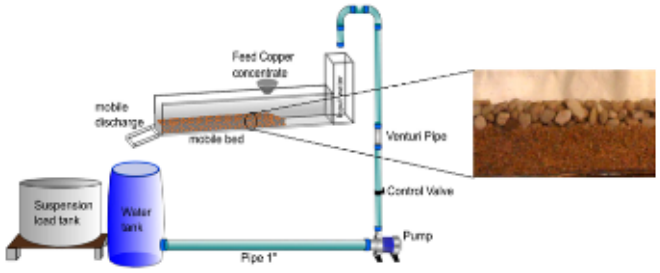

(b) Open channel with recirculating water system and movable gate to divert surface flow with suspended sediment. Experimental scheme implemented to investigate contamination of gravel beds with copper concentrate.

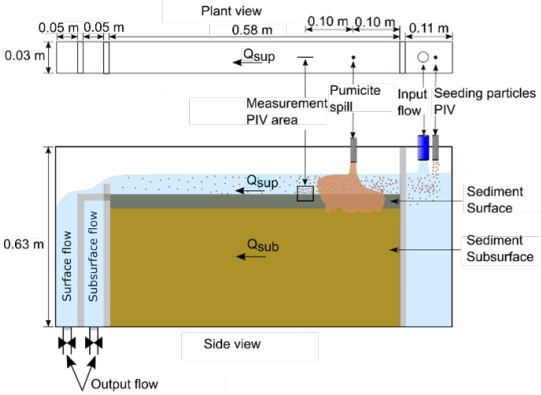

(c) Open channel with independent measurement system for surface and subsurface flow. Experimental scheme implemented to investigate contamination of gravel beds with pumicite and copper concentrate.

Figure B.1: Facilities implemented by: **a.)** Fuentes (2017), **b.)** Bustamante-Penagos, Niño (2020b), **c.)** Bustamante-Penagos, Niño (2020a).

For the analysis of the velocity time series in the neighbourhood of the gravel bed, the methodology presented by Bustamante-Penagos, Niño (2020a) was implemented, in which a space between two particles (a pore) was considered and three measurement points were taken, upstream of the pore (P1), in the pore (P2) and downstream of the pore (P3) (Figure B.2). Vertical velocities, and Wavelet frequency spectra of the vertical and streamwise velocities were analyzed.

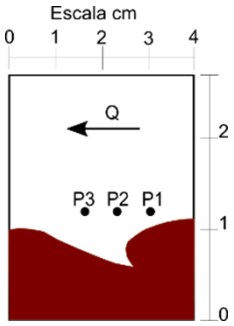

Figure B.2: Location of the points where the time series velocity were analyzed. P1 is upstream of the pore, P2 is in the pore and P3 is downstream of the pore. The gravel bed is shown in brown. The mean diameter of the gravels were 10 mm.

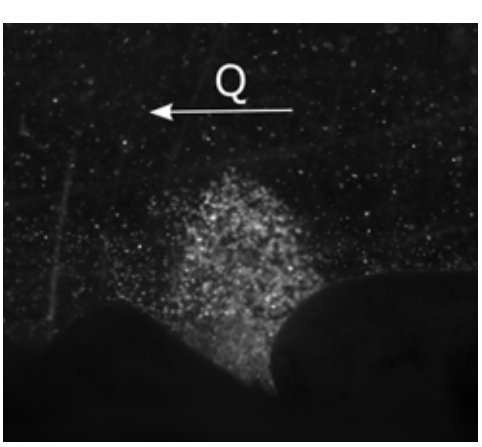

(a) Sediment ejection.

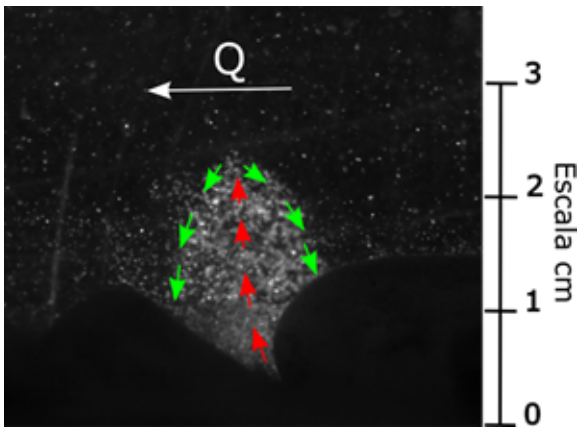

(b) Trajectory of fine particles ejected from the bed.

Figure B.3: Fine sediment ejection in a gravel bed reported by Bustamante-Penagos, Niño (2020a).

Figure B.3 shows the subsurface flow upwelling and fine particle transport associated with sediment ejection reported by Bustamante-Penagos, Niño (2020a). The red arrows represent the flow ejected through the pore and also the vertical movement of fine particles ejected from the bed into the water column. Whereas, the green arrows represent the outer edge of the sediment ejection and also the zones of vertical downward movement of fine particles ejected from the bed.

Wavelet Frequency Spectra

Wavelet frequency spectra were considered over Fourier frequency spectra, since the Wavelet transform does not require stationary series and also has the property of localization (Perrier et al., 1995; Bronshtein et al., 2007). In addition, the Wavelet transform is more robust and generates error propagation associated with some perturbations. For the continuous Wavelet transform of a signal $u(t)$ is defined as:

$$W_a(a, t_0) = \int_{\infty}^{\infty} u(t')\mathrm{d}t' \frac{1}{\sqrt{a}} \psi * (\frac{t_0 - t'}{a})\ \mathrm{d}t' \tag{B.1}$$

Where ψ is the wavelet function, $*$ denotes the complex conjugate, a and t_0 are the scale and position, respectively. The wavelet function considered in this work was the Morlet, which is defined as:

$$\psi(t) = \pi^{-1/4} \mathrm{e}^{\mathrm{i}\omega_0 t} \mathrm{e}^{-t^2/2} \tag{B.2}$$

Performing a procedure analogous to Fourier analysis for cross-correlations we obtain:

$$W_u v(a,t) = W_u(a,t) W_v^*(a,t). \tag{B.3}$$

It can be shown that, the frequency spectrum is given by:

$$E_{uu}(f) = \frac{1}{v} \int_{\infty}^{\infty} |W_{uu}(f,t)|^2 \mathrm{d}t \tag{B.4}$$

Where $|W_{uu}(f,t)|^2$ is the local Wavelet spectrum. In this article the mathematical analysis of the Wavelet transform is not presented, since it is outside the scope of the paper. However, authors such as Torrence, Compo (1998); Bronshtein et al. (2007); Chen et al. (2019), present a detailed mathematical analysis of the Wavelet transform.

Results

Vertical velocity

The dimensionless vertical velocity with the mean flow velocity at the measurement points P1, P2 and P3 are presented in Figure 4a-c for each experimental setup. The analysis is presented as a function of dimensionless time $t*$, where $t* = tU/H$, t is the time, U is the mean flow velocity and H is the sheet of water. Figure B.4a and Figure B.4b show that the variation of the flow velocity in the dimensionless time is the same at the three points, with a small time shift. That is, the Taylor frozen theory hypothesis is valid. Whereas, Figure B.4c shows a variation of vertical velocity between measurement points P1, P2 and P3, i.e., sediment ejection makes the frozen turbulence hypothesis invalid. Additionally, Figure B.4c shows that the pore has the highest vertical velocity upstream, due to sediment ejection. While, downstream of the pore, the highest vertical downward velocity occurs, because in this zone a sink is generated for the deposition of particles ejected through the pore. It is important to highlight that Bustamante-Penagos, Niño (2020b) used cohesive and high density fine particles, copper concentrate, and the exposure ratio of fines in the gravel bed, e/D_g, was approximately 1, where e is the difference between the deposition height of the fine sediment, H_s, and the height of the gravel layer, H_g, and D_g is the gravel diameter. Fuentes (2017) used glass particles and $\mathrm{e}/D_g \sim 0.5$. In both cases, no sediment ejections and no vertical velocity variation between sampling points (upstream, pore, and downstream) were found. While Bustamante-Penagos, Niño (2020a) considered pumicite particles. The relationship $\mathrm{e}/D_g \sim -0.1$, in this case, sediment ejections were reported and also an effect of sediment ejection on the velocity field was evidenced. On the other hand, there was a reduction in bed permeability. However, there was a constant inflow of subsurface flow. That is to say, the size of the gravel interior conduits through which the subsurface flow was initially transported was reduced, this causes it to outcrop to the surface flow and as it passes

it ejects sediment deposited within the bed.
Pumicite is a non-monodisperse, low-density material, so particle segregation can occur and the finer particles may form seals within the substrate. Therefore, subsurface flow can destabilize the particles in the seals and eject them from the gravel bed. That is, sediment ejections may represent the points where there were internal breaks in the streamwise subsurface flow (Bustamante-Penagos, Niño, 2020b).

Wavelet spectrum

Considering that the sediment ejection in the Bustamante-Penagos, Niño (2020a) paper has a quasi-permanent condition, we considered the implementation of Wavelet frequency analysis for the time series, u' and w', for each of the experiments. Figure B.5 and Figure B.6 and present the wavelet power spectra, $|W_u|^2$ and $|W_v|^2$ dimensioned by Hu_*, of the velocity fluctuations u' and w', respectively. Where the abscissa correspond to the dimensional time, tU/H, and the ordinates correspond to λ/H, with $\lambda = U/f$ as the wavelength and f the frequency, H the water depth and t is the time.
The wavelet spectra show a higher concentration of the power spectrum in the streamwise component where there is no sediment ejection (Figure B.5 and Figure B.6). This is expected since the vertical component of velocity is much smaller than the streamwise component. On the other hand, the streamwise component of the velocity fluctuations, u', allowed the identification of large-scale structures for the three experiments analyzed. For Fuentes (2017), large-scale structures, i.e., $\lambda > 10H$, were identified and no effect of the pore on the spectral density was found. The $\lambda \sim 15H$ structures are present between $54 < t* < 400$. Whereas, $\lambda \sim 13H$ structures concentrate their spectral density at $t* \sim 110$. On the other hand, the data of Bustamante-Penagos, Niño (2020b) also show large-scale $\lambda \geq 10H$ structures concentrating their spectral density during the whole measurement time and no pore effect on the spectral density concentration is evident neither downstream, nor upstream of the pore. On the contrary, in the case of sediment ejection, Bustamante-Penagos, Niño (2020a) report that the highest spectral density concentration occurs upstream of the pore and there is a decrease in large longitudinal scale structures downstream of the pore.
It is important to highlight that for the cases where sediment ejection is not present, there are no major variations in the spectral density distribution for both the streamwise and vertical velocity components. In addition, the streamwise component of the velocity is where the highest spectral density occurs (Figure B.5 and Figure B.6).

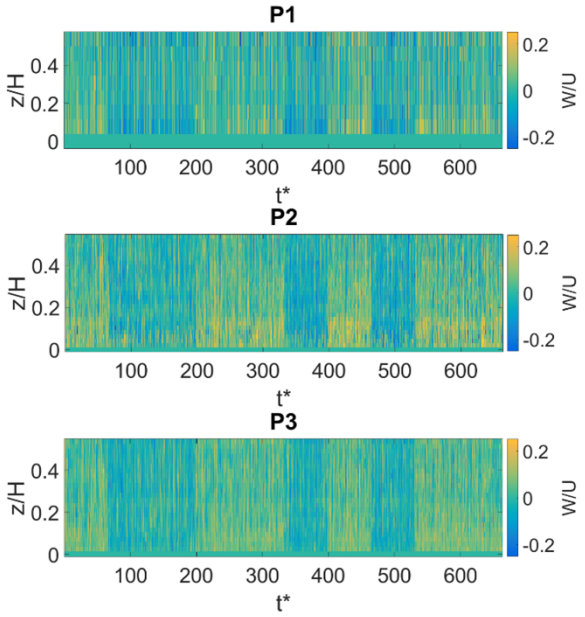

(a) Vertical velocity dimensionless with mean flow velocity for Taylor frozen hypothesis analysis for experimental data Fuentes (2017).

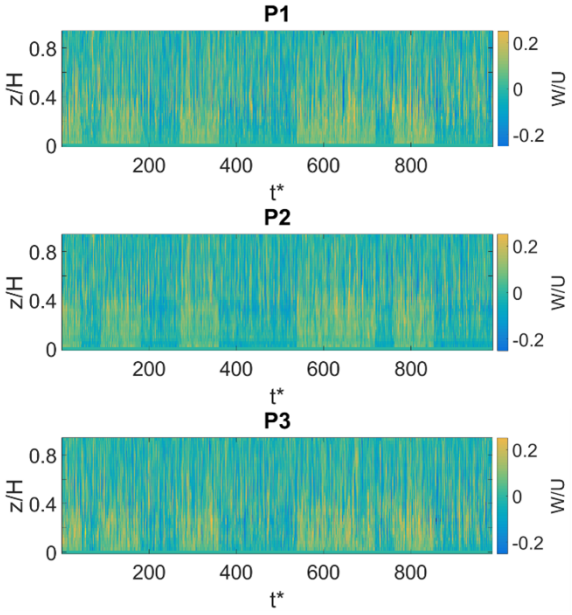

(b) Vertical velocity dimensionless with mean flow velocity for Taylor frozen hypothesis analysis for experimental data Bustamante-Penagos, Niño (2020b).

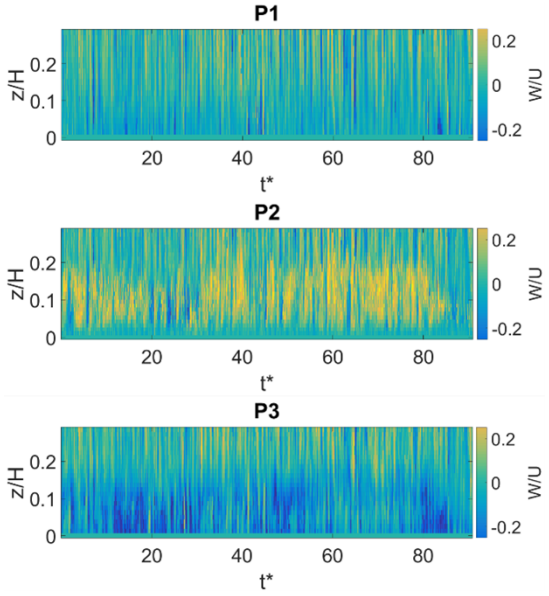

(c) Vertical velocity dimensionless with mean flow velocity for Taylor frozen hypothesis analysis for experimental data Bustamante-Penagos, Niño (2020a).

Figure B.4: Vertical velocity dimensionless with U, w/U, for: **(a)** upstream of the pore (P1), **(b)** in the center of the pore (P2) and **(c)** downstream of the pore (P3).

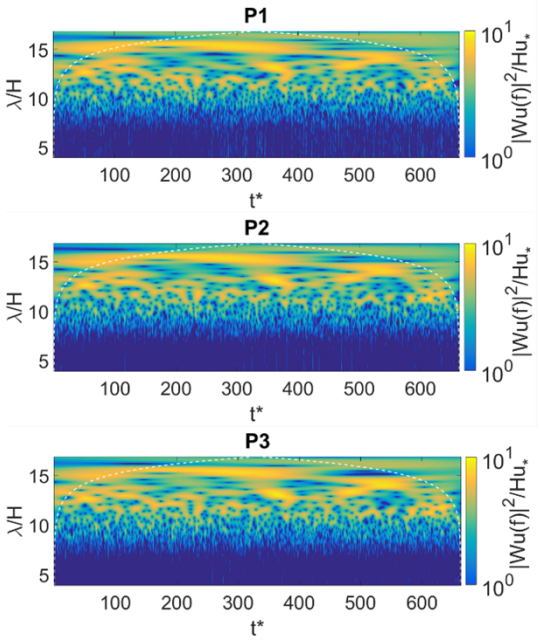

(a) Spectral density for velocity fluctuation in the streamwise component for experimental data Fuentes (2017).

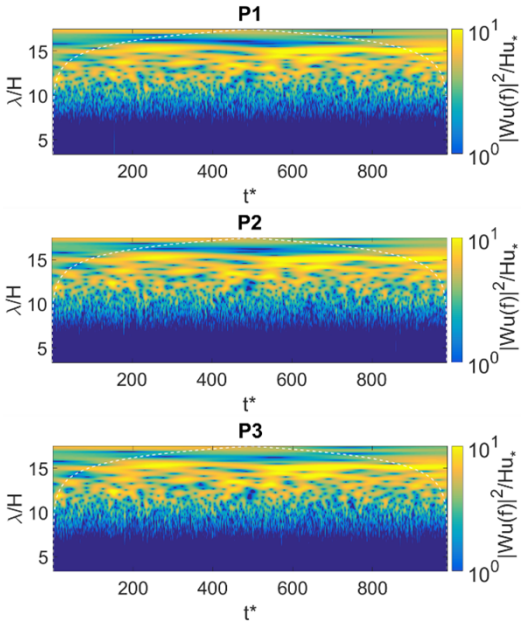

(b) Spectral density for velocity fluctuation in the streamwise component for experimental data Bustamante-Penagos, Niño (2020b).

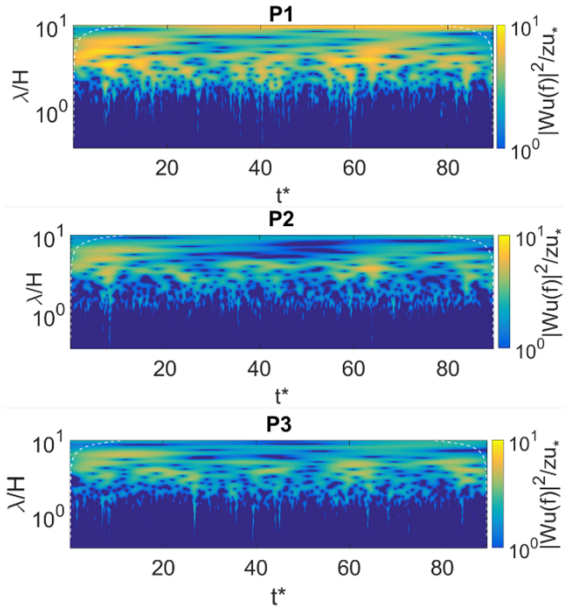

(c) Spectral density for velocity fluctuation in the streamwise component for experimental data Bustamante-Penagos, Niño (2020a).

Figure B.5: Wavelet spectrum for velocity fluctuations in the streamwise component u', (**a**) upstream of the pore (P1), (**b**) in the center of the pore (P1) and (**c**) downstream of the pore (P3).

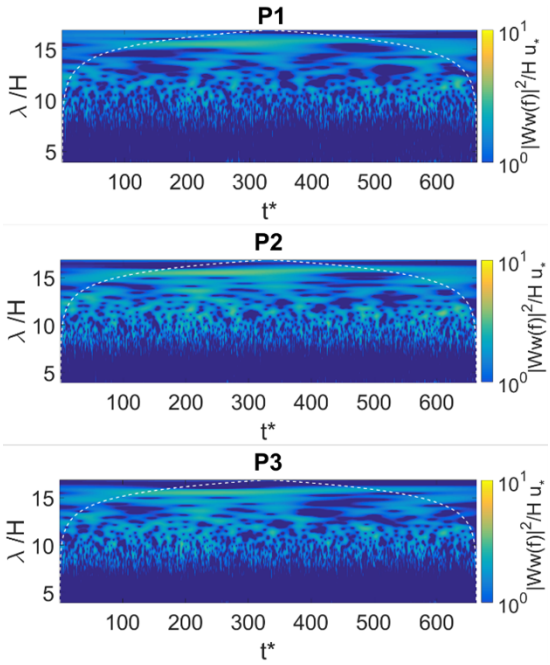

(a) Spectral density for velocity fluctuation on the vertical component for experimental data Fuentes (2017).

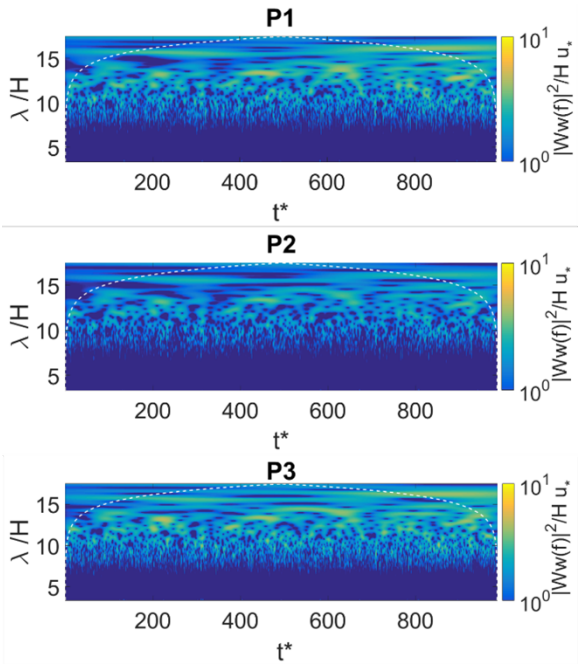

(b) Spectral density for velocity fluctuation on the vertical component for experimental data of Bustamante-Penagos, Niño (2020b).

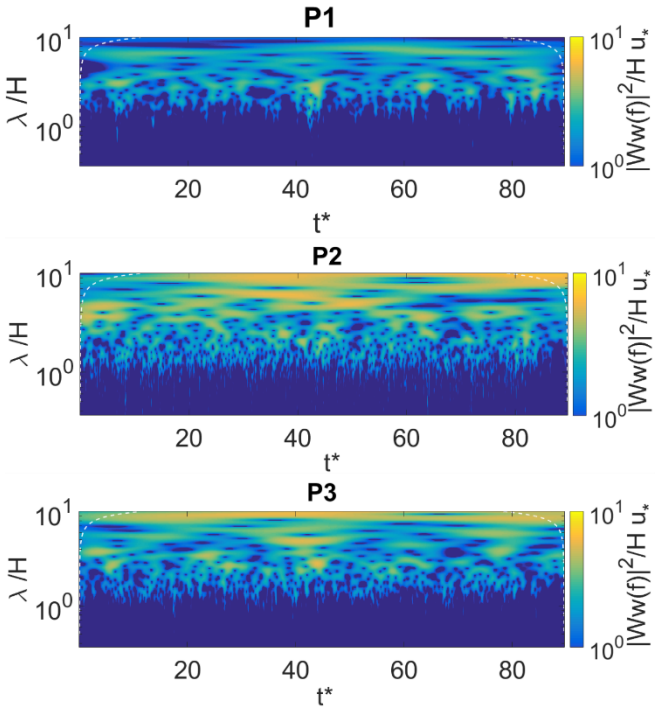

(c) Spectral density for velocity fluctuation of the vertical component for experimental data of Bustamante-Penagos, Niño (2020a).

Figure B.6: Wavelet spectrum for velocity fluctuations in the streamwise component w', (**a**) upstream of the pore (P1), (**b**) in the center of the pore (P1) and (**c**) downstream of the pore (P3).

Conclusions

This research presents an analysis of the effect of the pore on vertical velocities and spectral density distribution in the neighborhood of the gravel bed. Three experimental setups with gravel beds and with three types of fine sediments were considered: glass particles, copper concentrate and pumicite. In the experiments made by Fuentes (2017); Bustamante-Penagos, Niño (2020b), no fine sediment ejections were evidenced, nor was an effect on the vertical component of the velocity and spectral density spectra associated with the gravel pore identified. In contrast, in the Bustamante-Penagos, Niño (2020a) experiment, sediment ejection was formed, which generated a change in the vertical component of the velocity. Taylor's frozen turbulence hypothesis was no longer valid under these conditions and also generated modifications in the spectral density spectra upstream of the pore, in the pore and downstream of the pore.

The formation of sediment ejection is due to a change in the permeability of the gravel bed, constant subsurface flow inflow, an $e/D_g \sim -0.1$ ratio, low-density fine sediment, and a low mean surface velocity. Subsurface flow upwelling is generated by the clogging of internal conduits in the gravel bed. That is, when the pores of the sand and gravel are clogged with pumicite, flow infiltration to lower strata is limited. These flow ejections are generated by the downstream clogging of the internal gravel ducts, which destabilize the pumicite seals formed after the deposition of the fine sediment from the lower part of the gravel bed.